Probing modes of vesicle docking in neurosecretory cells with evanescent wave microscopy

PhD Thesis

in partial fulfilment of the requirements
for the degree “Doctor of Philosophy (PhD)”
in the Neuroscience Program
at the Georg-August University Göttingen,
Faculty of Biology

submitted by
Olexiy Kochubey
born in Dniepropetrovsk, Ukraine

2005

Herein I declare

that my PhD thesis “Probing modes of vesicle docking in neurosecretory cells with evanescent wave microscopy” has been written independently and with no other sources and aids than quoted

Göttingen, 15.12.2005

Signature …….

List of Contents

Chapter 1

Introduction

1.1 Exocytosis in neuronal signaling and neurosecretion

Exocytosis is a fundamental process by which intracellular membranous compartments (trafficking vesicles) can deliver their membrane material or content to the plasma membrane or to the extracellular space. The process involves fusion of intracellular vesicles with the plasma membrane, for review see (Jahn et al., 2003; Jahn, 2004). Exocytosis is a ubiquitous process resulting in addition of the material to the plasma membrane. It is utilized by all eukaryotic cells in the process of cell growth, development, division, membrane remodeling and delivery of membrane-associated molecules. Another important purpose of exocytosis is to transmit the chemical signals into the cell's surrounding. The signals are the molecules, produced and packaged into the vesicles inside the cell, that escape through the vesicle opening ('fusion pore') or after the vesicle collapses into the plasma membrane, and then reach the target receptors by diffusion. When the release of signaling substances can be controlled or synchronized by any trigger, exocytosis becomes a powerful mechanism of cell-to-cell communication. This principle is employed for signaling in neuron-neuron chemical synapses and neuromuscular junctions, i.e. in neurotransmission. The signaling substances, named neurotransmitters, were found to be released from the presynaptic terminals in small multi-molecular packages or quanta, producing miniature endplate (or postsynaptic) potentials (Del Castillo and Katz, 1954). These quanta were postulated to correspond to the content of single synaptic vesicles whose fusion with the plasma membrane was later proved ultrastructurally (Heuser and Reese, 1973; Heuser et al., 1979). The trigger for release of a single neurotransmitter-filled vesicle, when powerful enough, can synchronize exocytosis of many vesicles thus resulting in a massive release of neurotransmitter into the synaptic cleft which produces evoked response at the postsynaptic specialization. The trigger for synaptic vesicle fusion, as recognized quite early, is the depolarization-induced Ca^{2+} influx into the presynaptic terminal (Katz and Miledi, 1965).

The regulated exocytosis at neuronal synapses was studied extensively over the past three decades. Namely fusion of synaptic vesicles with the plasma membrane is only a part of complex cycle of synaptic vesicles (Betz and Angleson, 1998; Sudhof, 2004). The synaptic vesicle cycle is necessary to maintain the membrane area after fusing intracellular vesicles and refilling the pool of functional neurotransmitter-filled vesicles, available for the next round of exocytosis (Heuser and Reese, 1973). A simplified schematic of the cycle is shown in Fig. 1.1.

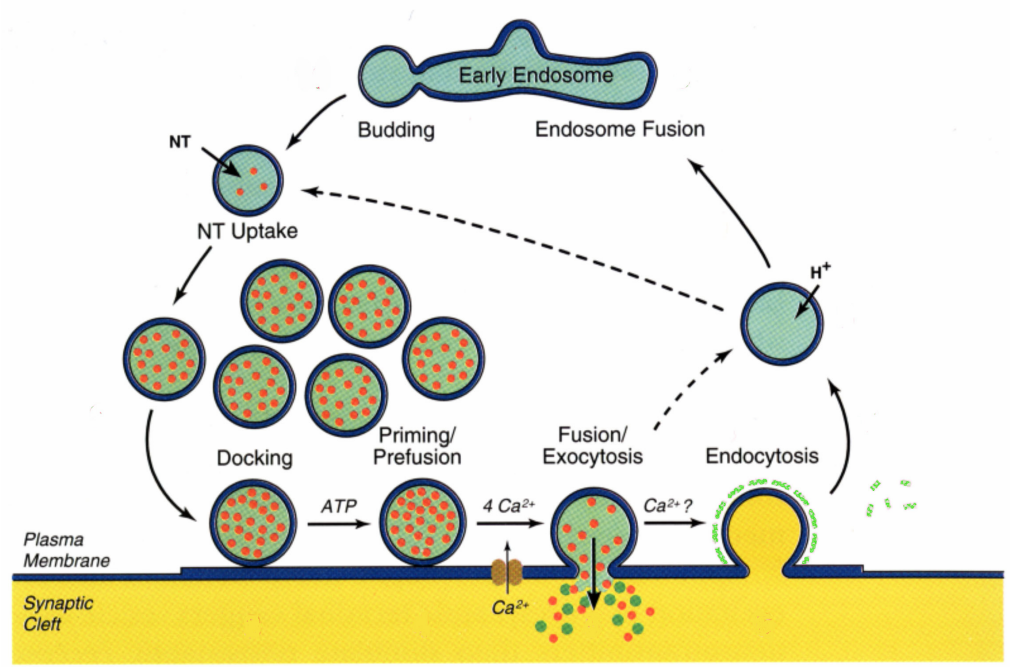

Fig. 1.1. A schematic of the synaptic vesicle cycle showing the exocytotic (docking, priming, fusion), endocytotic and recycling/refilling steps. Adopted from (Südhof and Scheller, 2001).

Most synaptic vesicles at rest reside inside the synaptic terminal and comprise the so-called reserve pool (Kuromi and Kidokoro, 1998; Richards et al., 2000; Satzler et al., 2002; Rizzoli and Betz, 2004). Before undergoing exocytosis by fusing with the plasma membrane, vesicles first establish morphological contact with the membrane near the release site (‘active zone’ in synapses), the process called docking (Steyer et al., 1997; Harlow et al., 1998). After the contact, the vesicle should pass through ATP-dependent maturation steps (‘priming’) (Eliasson et al., 1997; Kawasaki et al., 1998; Ashery et al., 2000; Chen et al., 2001). The final fusion step occurs upon depolarization-evoked Ca^{2+} influx through voltage-activated calcium channels. Calcium ions entering the presynaptic terminal are able to trigger rapid (~0.1 ms) fusion by formation of a fusion pore and merging of the vesicular and plasma membranes (Borst et al., 1995; Sabatini and Regehr, 1998; Moser and Beutner, 2000). Vesicle fusion can be also a spontaneous event (in the absence of stimulation), with probability to occur depending on the resting calcium concentration (Lou et al., 2005). The problem of the mechanism of fusion pore formation (a structure connecting vesicle lumen and extracellular space) is still open. Some works suggest that the fusion pore is formed by the merging phospholipid bilayers (Zenisek et al., 2002; Jahn et al., 2003; Taraska and Almers, 2004), while others propose formation of a proteinacious fusion pore (Han et al., 2004; Hiesinger et al., 2005; Richards et al., 2005).

To complete the cycle, synaptic vesicles and associated molecular constituents must be retrieved from the plasma membrane by endocytosis. There are evidences for different modes of endocytosis and pathways of vesicle recycling, which are debated in the literature (Royle and Lagnado, 2003). Most likely several modes of vesicle retrieval exist

and their occurrence depends on the synapse and regime of synaptic activity: a) kiss-and-run – combination of fast incomplete fusion and rapid retrieval by closure of the fusion pore (Ceccarelli et al., 1972; Klingauf et al., 1998; Sun et al., 2002; Aravanis et al., 2003; Gandhi and Stevens, 2003); b) two modes of compensatory endocytosis, fast and slow, independent and dependent on clathrin (Koenig and Ikeda, 1996; Beutner et al., 2001; Jockusch et al., 2005); c) bulk membrane retrieval (Koenig and Ikeda, 1989; Lenzi et al., 2002; Paillart et al., 2003). There are at least two described vesicle recycling pathways of retrieved vesicles (Fig. 1.1, smooth and dotted lines), necessary to refill the different populations of vesicles ('vesicle pools') for maintaining following rounds of exocytosis: rapid recycling into the readily-releasable pool and slow recycling through reserve pool and/or endosomal intermediates (Koenig and Ikeda, 1996; Klingauf et al., 1998; Pyle et al., 2000; Richards et al., 2000; Sara et al., 2002). Existence of distinct morphological vesicle pools and division of the readily-releasable pool into smaller functional exocytotic pools based on molecular steps and Ca^{2+}-regulation of exocytosis (see next sub-section), have important consequences in short-term synaptic plasticity, reviewed in (Schneggenburger et al., 2002; Zucker and Regehr, 2002).

Neurosecretory cells, like chromaffin cells of the adrenal medulla, are derived from the neural crest during development (Unsicker et al., 2005) and posses similarities with neurons. Chromaffin cells receive sympathetic input through acetylcholinergic stimulation by the splanchnic nerve, are able to fire action potentials, and are responsible for release of catecholamines (Brandt et al., 1976), adrenalin or noradrenalin (Kobayashi and Coupland, 1993), into the blood stream. Adrenal medulla and chromaffin cells are thus the part of the neuroendocrine system involved in regulation of cardiovascular tone. Catecholamine is stored in the large dense core vesicles (LDCV), secretory granules (Gorgas and Bock, 1976; Grabner et al., 2005) conserved among neurosecretory cells. Chromaffin cells contain also certain fraction of electron-lucent small synaptic-like vesicles (Kobayashi, 1977; Koval et al., 2001) containing acetylcholine, similar to neuronal synaptic terminals which, apart from the main pools of synaptic vesicles, also have large secretory peptidergic vesicles. The LDCVs in chromaffin cells fuse with the plasma membrane upon Ca^{2+} influx through the L-, P/Q- and R-type of voltage-gated calcium channels (Chan et al., 2005). The LDCVs which undergo secretion can be functionally divided into several exocytic pools (Sorensen, 2004), in analogy to the exocytic vesicle pools in neurons, possesing very similar properties of molecular regulation. Relative ease of preparation, genetic manipulations, robustness, and, most important, similarity of the molecular machinery of secretion to the synaptic, makes chromaffin cells a suitable model for studying molecular mechanisms of regulated exocytosis (Kobayashi, 1977; Bader et al., 2002). In this work, chromaffin cells and exocytic steps of LDCVs will be used as a model to study molecular aspects of synaptic vesicles docking.

1.2 Molecular machinery of regulated secretion, exocytotic vesicle pools

Synaptic vesicle exocytosis as well as LDCV secretion is tightly regulated. The mechanism underlying preparation for fusion, secretion and its regulation is determined by the complex molecular interactions between the proteins and lipids of synaptic vesicles and target membranes. The set of vesicular proteins with implicated roles in exocytosis is illustrated in Fig. 1.2a (Li and Chin, 2003; Sudhof, 2004). Among the multitude of important vesicular proteins, two play a crucial role in the last steps of exocytotic part of vesicle cycle: Synaptobrevin and Synaptotagmin.

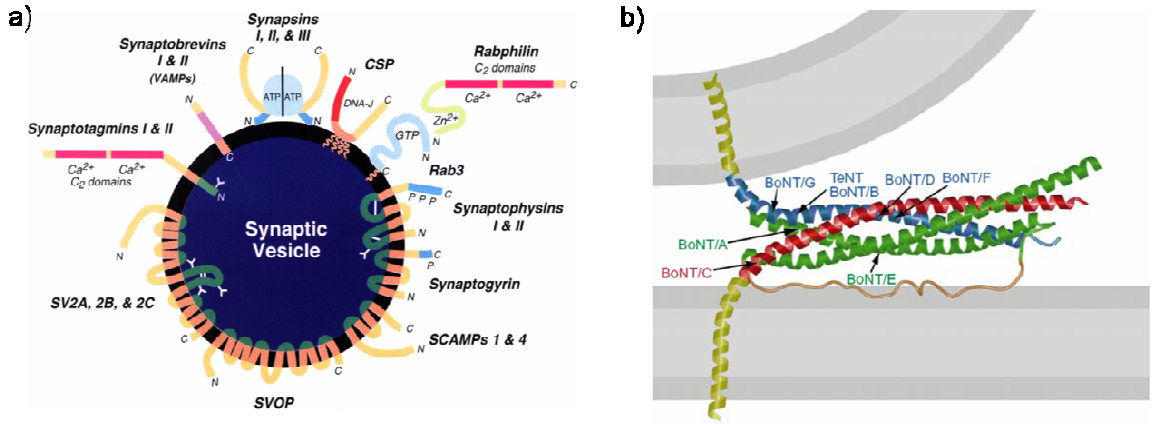

Fig. 1.2. (**a**) A set of synaptic vesicle proteins which take part in regulation of vesicle exocytosis and vesicle cycle. From (Südhof and Scheller, 2001). (**b**) Assembled neuronal SNARE complex (Synaptobrevin-2, blue, Syntaxin-1a, red, SNAP-25B, green), necessary for vesicle fusion to occur. From (Sutton et al., 1998).

Synaptobrevin is one of the soluble NSF (*N*-ethylmaleimide sensitive fusion protein) attachment protein receptors (SNAREs), a protein family highly conserved in evolution which determines specificity and regulation of vesicle trafficking and fusion (Fasshauer et al., 1998). The other two partner SNARE proteins in neurons and neurosecretory cells (SNAP-25 and Syntaxin-1a) reside on the target plasma membrane and can form a stable complex with Synaptobrevin (Fig. 1.2b) which then is able to drive a membrane fusion reaction *in vitro* and *in vivo* (Sollner et al., 1993; Sutton et al., 1998; Weber et al., 1998; Fix et al., 2004; Liu et al., 2005). Neuronal SNARE proteins are targets for cleavage with neurotoxins (Fig 1.2b) which, together with the genetic deletion experiments, prove their essential role in the last steps of Ca^{2+}-triggered exocytosis, between vesicle docking and final fusion (Broadie et al., 1995; Foran et al., 1996; Chen et al., 2001; Schoch et al., 2001; Washbourne et al., 2002; Sorensen et al., 2003; Borisovska et al., 2005).

Synaptotagmins-1,2 are vesicular proteins with C_2 domains (A and B) that have ability to bind phospholipids in Ca^{2+}-dependent manner (Rizo and Sudhof, 1998). Synaptotagmin-1 can bind to the Syntaxin-SNAP-25 SNARE dimer (Rickman et al., 2004), and thus is one of the main candidates for the calcium sensor in fast synchronous

Ca^{2+}-triggered fusion of synaptic vesicles upon calcium influx (Geppert et al., 1994; Fernandez-Chacon et al., 2001; Voets et al., 2001; Sorensen et al., 2003; Tucker et al., 2004; Maximov and Sudhof, 2005), while the SNARE core complex itself might also contribute to the calcium triggering of fusion (Chen et al., 2005). The molecular identity and the question whether more than one sensor can account for the high Ca^{2+}-sensitivity and cooperativity and accommodate different modes of short-term synaptic plasticity and synchronicity of release (Schneggenburger and Neher, 2005), is now debated. As already was stressed before, and shown in some of the cited studies, molecular events of Ca^{2+}-triggered release of LDCVs in neurosecretory cells is very closely related to the synaptic release machinery, with the differences restricted down to different isoforms of proteins involved in fusion machinery and organization of the active zones (in neurosecretory cells, release sites).

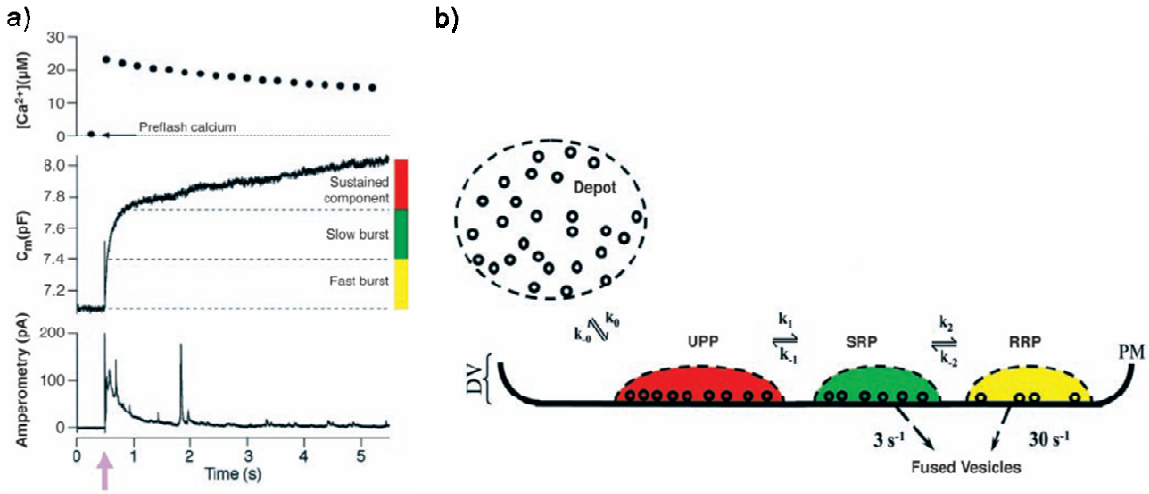

Fig. 1.3. (**a**) Three phases of LDCV release (fast burst, slow burst and sustained component) measured in chromaffin cells with capacitance monitoring cell membrane area and amperometry recordings upon step-like increase in intracellular Ca^{2+} concentration. (**b**) A kinetic model explaining different modes of LDCV exocytosis: slow and rapidly releasable pools (SRP, RRP) account for the slow and fast exocytic burst while their refilling by priming of vesicles from unprimed pool (UPP) can explain sustained component. *From (Rettig and Neher, 2002)*.

Calcium influx into presynaptic terminals of different types of synapses revealed several kinetic components of exocytosis, as could be measured with capacitance recordings or using release rate deconvolution techniques (Goda and Stevens, 1994; Neves and Lagnado, 1999; Moser and Beutner, 2000; Sakaba and Neher, 2001; Lou et al., 2005). In neurosecretory chromaffin cells of adrenal medulla, step-like $[Ca^{2+}]_i$ elevation by Ca^{2+}-uncaging leads to the three-component exocytic response (Fig. 1.3a) when monitored with capacitance recordings.

The three components can be associated with three distinct states, or pools of vesicles: unprimed pool (UPP), slow and rapidly releasable pools (SRP, RRP) (Voets et

al., 1999). These three pools are downstream of vesicle docking, and there is evidence that the readily releasable pool (SRP+RRP) consists of all or a fraction of the morphologically docked vesicles in either synapses or neurosecretory cells (Vitale et al., 1995; Schikorski and Stevens, 2001). Distinct kinetic components can originate from two different mechanisms: molecular heterogeneity (i.e. Ca^{2+}-sensitivity) of vesicles or their release sites, or differences in positions of vesicle release sites relative to the sites of Ca^{2+} entry (Klingauf and Neher, 1997; Neher, 1998), or both. The Ca^{2+}-uncaging approach allows studying exclusively the contribution of vesicular heterogeneity into kinetically different release components (Voets et al., 1999). This technique, in which Ca^{2+} can be step-wise homogenously elevated throughout the cell cytoplasm, allowed to dissect molecular players in LDCV exocytosis by analyzing filling degree and transitions between different pools.

The major changes in the vesicle's state, which is accompanied with certain molecular events, are thus docking to the plasma membrane (Depot pool→UPP), priming (acquisition of release-competence: UPP→SRP+RRP) and final fusion. The molecules involved at these last steps of priming and fusion, are mostly SNAREs and SNARE-interacting molecules (Sorensen, 2004). It was described in the literature that vesicle supply into the readily releasable pool can be increased by PKC activation with phorbol ester or elevated Ca^{2+} concentration (Gillis et al., 1996; Smith et al., 1998; Nagy et al., 2002), as well as in hippocampal neurons (Stevens and Sullivan, 1998). Munc13-1, a molecule implicated in facilitation and stabilization of the open state of Syntaxin-1a, was found to be one of the priming factors in chromaffin cells (Ashery et al., 2000), as in central synapses (Rosenmund et al., 2002). Priming, in general, requires SNAREs, thus this step can be modulated by treatments modifying SNARE partners or interacting proteins (Xu et al., 1999; Nagy et al., 2002; Nagy et al., 2004). The LDCV fusion itself requires SNAREs (Xu et al., 1998; Sorensen et al., 2003; Borisovska et al., 2005), and Ca^{2+} sensitivity of fusion is determined mostly by the proteins of Synaptotagmin family (Voets et al., 2001; Sorensen et al., 2003). Amperometry recordings of catecholamine release can provide direct insight on the very late phase of fusion – dynamics of the fusion pore and its modulation (Burgoyne et al., 2001).

In contrast to the intensively studied priming and fusion steps, not much is known about the molecular mechanisms of LDCV or synaptic vesicle docking.

1.3 Molecular mechanism and technical approaches for studying vesicle docking

Vesicle translocation to the target membrane and docking are the most upstream processes in a sequence of events in preparation for Ca^{2+}-triggered exocytosis. Zippering-up of four SNARE-domains of the SNARE proteins is thought to be the central molecular mechanism to drive fusion of vesicles with their target membrane (Jahn et al., 2003). As mentioned above, genetic deletion or enzymatic cleavage of SNARE genes/proteins

invariably blocks fusion of transport and secretory vesicles, and evidence is accumulating that SNAREs participate in several sequential processes in the exocytosis pathway leading up to and including the formation of a fusion pore between the vesicle interior and the outside of the cell. It was initially suggested that SNAREs and core complex formation might serve as a docking platform for vesicle docking (Bennett et al., 1992; Sollner et al., 1993). However, SNARE-complex assembly is not likely to be the first event occurring when the vesicles reach their target. Deletion and toxin-mediated cleavage experiments suggest that SNAREs are not necessary to morphologically dock synaptic or large dense core vesicles at the target membranes of presynaptic terminal or chromaffin cell (Hunt et al., 1994; Broadie et al., 1995; O'Connor et al., 1997; Schoch et al., 2001; Washbourne et al., 2002; Sorensen et al., 2003; Borisovska et al., 2005). Hence, unknown processes distinct from and upstream of SNARE-complex assembly must be involved in the reception of arriving vesicles.

It was suggested that Synaptotagmin might be responsible for vesicle docking to the presynaptic membrane (Petrenko et al., 1991), supported by later findings of morphological vesicle docking impairment in neuromuscular junction and squid giant synapse by interference with Synaptotagmin-1 function (Reist et al., 1998; Fukuda et al., 2000). The possible role of Synaptotagmin-1 in vesicle docking is also supported by biochemical studies showing Synaptotagmin-1 binding to the t-SNARE SNAP-25 or a Syntaxin-1a/SNAP-25 dimer (Schiavo et al., 1997; Chieregatti et al., 2002; Rickman et al., 2004), however this hypothesis contradicts the intact vesicle docking after genetic deletion of SNARE proteins.

Another study recently proposed a role for the exocyst complex Sec6/8 in docking of insulin containing secretory granules in the cells of pancreatic lineage (Tsuboi et al., 2005). The exocyst complex was originally described in yeast and implicated for secretory vesicle docking/tethering in polarized secretion upstream of Sec1p/Syntaxin interaction (Novick and Guo, 2002; Jahn, 2004), however the mechanism involving mammalian exocyst in synaptic vesicle or neurosecretory granule docking has to be further investigated (Hsu et al., 1999).

One strong candidate for a key molecule in the vesicle docking machinery upstream of fusion was obtained in studies of LDCVs docking in neuroendocrine cells. Deletion of *munc18-1* expression (Verhage et al., 2000) produced a marked defect in LDCV docking to the plasma membrane in adrenal chromaffin cells (Voets et al., 2001) and somatotrophs of the anterior pituitary (Korteweg et al., 2005). Moreover, studies performed with *Munc18-1* null mutant mouse (M18 KO) showed completly abolished transmission in neurons (Verhage et al., 2000), as well as a severe impairment of LDCV secretion (Voets et al., 2001; Korteweg et al., 2005). Synaptic development and axonal wiring of the brain were, in contrast, intact in M18 KO mice. A very similar phenotype was also described in *C. elegance* mutants of *unc-18* gene, including severe defects in synaptic vesicle docking and exocytosis at the neuromuscular junction (Weimer et al., 2003). The current

knowledge about Munc18-1 and its role in secretory cascade is described in the next sub-section.

Although some molecular players in the process of vesicle docking are proposed in the literature, the precise mechanism is not known. A more systematic analysis of the gene cascade that orchestrates the reception of vesicles at their target membrane is hampered by the currently poor definition of the docking process itself. Docking is typically assessed on the basis of electronmicrographs. Electron microscopy provides very high spatial resolution, however this method does not allow the study of vesicle dynamics in living cells and thus precludes the identification of different states of docking, if there are. In contrast, electrophysiological approaches, capacitance measurements of changes in the cell membrane area (Neher and Marty, 1982) and amperometric detection of catecholamine release (Chow et al., 1992), posses very high sub-millisecond temporal resolution sufficient for high quality detection of single vesicle fusion events. One disadvantage is that the whole-cell configuration of the patch-clamp technique in which capacitance recordings are usually performed does not reveal spatial information on exocytic activity. Spatial resolution of amperometry is limited by the size of the carbon electrode used, and can be increased using a special recording configuration (Hafez et al., 2005). However, both capacitance and amperometry techniques are designed for monitoring secretion, i.e. only final fusion events contribute to the resulting signal. It means, in turn, that the kinetic transitions between vesicle pools upstream of fusion can only be estimated from fitting the cumulative response after depletion of most of the readily releasable pool of vesicles during ongoing stimulation (Fig. 1.3a), with several exponential functions. In this case, the sustained component is determined by the rate of priming of UPP vesicles and of docking of Depot vesicles. Docking is usually much slower than priming (Voets et al., 1999), and isolation of the docking rate requires strong repeated stimuli to deplete the readily releasable pool as well as UPP.

In order to study docking at the level of single vesicles, imaging techniques with high spatial and temporal resolution must be applied. Imaging techniques using fluorescent microscopy approaches with currently available fluorescent probes, can provide sufficient spatial and temporal resolution and sensitivity to study vesicle cycle at single vesicle or even single molecule level (Ryan, 2001). Among them, evanescent wave, or total internal reflection microscopy (TIRFM) is particularly suitable for monitoring dynamics of single fluorescently labeled vesicles within the optical section of ~100 nm thickness beneath the plasma membrane (Oheim et al., 1999; Oheim, 2001; Toomre and Manstein, 2001). The only requirement for the cellular preparation is that the cells attach to the cover glass with their membrane, forming a ‘footprint’ – the membrane area illuminated with the evanescent waves. This requirement is usually fulfilled with neurosecretory cells which tend to form a tight contact to the supporting glass. Detailed physical principles of the TIRFM technique are described in the section 2.1 of this work.

The method was widely applied in a number of biological applications including studies of exo/endocytosis. It was, for example, used in studying single vesicle release

from the bipolar cell synaptic terminal (Zenisek et al., 2002), release and recapture of large dense core vesicles in neurosecretory cells (Lang et al., 1997; Steyer et al., 1997; Tsuboi and Rutter, 2003; Allersma et al., 2004; Perrais et al., 2004; Taraska and Almers, 2004), dynamics of endocytic proteins and coated vesicles during endocytosis (Merrifield et al., 2002; Loerke et al., 2005; Merrifield et al., 2005) and many others. High axial resolution of the method makes it especially suitable for studying vesicle approach to the target membrane and establishing the morphological contact with the docking sites. Several studies addressed the question of vesicle docking to the plasma membrane using fluorescent dyes or genetically encoded fluorescent vesicle proteins (Steyer et al., 1997; Steyer and Almers, 1999; Oheim and Stuhmer, 2000; Johns et al., 2001; Loerke et al., 2002; Manneville et al., 2003). In these works single vesicle mobility was studied in ~100 nm proximity to the footprint plasma membrane and the role of submembrane cytoskeleton was thoroughly examined. However, only few addressed the question of the molecular machinery of docking by interfering with the known molecular players of exocytic cascade (Johns et al., 2001; Tsuboi et al., 2005). In the current work, the TIRFM imaging was combined with the single particle tracking, correlation and residency time analysis, and assisted by stochastic modeling, to better characterize molecular events in vesicle docking/tethering to the plasma membrane. Imaging was performed in combination with genetic manipulations, using M18 KO chromaffin cells as a starting point due to the pronounced impairment of LDCV docking in these cells (Voets et al., 2001). Electrophysiological and EM morphological analysis was performed by collaborating groups (headed by Drs. Jakob Sorensen and Matthijs Verhage, respectively), thus the set of complementary techniques allowed approaching the molecular mechanism of LDCV docking in neurosecretory cells.

1.4 Munc18-1 protein and its functions in secretion

Munc18-1 (or *n-Sec1*) belongs to the family of Sec1 genes responsible for the mechanisms regulating trafficking of intracellular vesicles between different cellular compartments, highly conserved in eukaryotic cells (Halachmi and Lev, 1996; Toonen and Verhage, 2003). Among this family, the yeast Sec1p, *C. elegance* Unc-18 and *D. melanogaster* Rop homologues of Munc18-1 are involved at early stages of secretion and regulated exocytosis in neuromuscular junction, central synapses, and neurosecretory cells (Novick and Schekman, 1979; Gengyo-Ando et al., 1993; Harrison et al., 1994). Munc18-1 was discovered at the same time by different groups (Hata et al., 1993; Garcia et al., 1994; Pevsner et al., 1994). This protein, as well as other members of Sec1 family (Ogawa et al., 1996), is a soluble monomer with high binding affinity to the t-SNARE protein Syntaxin-1a,2,3 (Pevsner et al., 1994). The yeast homologue Sec1p is an exception since it binds to the assembled SNARE core complex (Carr et al., 1999). The crystal structure of Munc18-1 in complex with Syntaxin-1a is solved (Misura et al., 2000) and reveals a three-domain, arc-shaped globular protein (Fig. 1.4a) with a positively

charged cavity in domain 1, capable of binding to N-terminus of Syntaxin1A Habc domain in closed conformation (Fig. 1.4b, schematic).

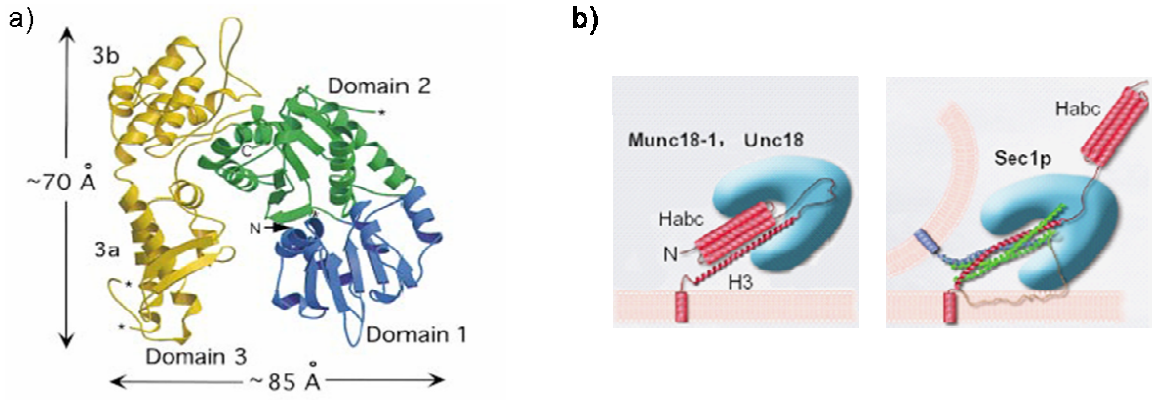

Fig. 1.4. (**a**) Ribbon representation of Munc18-1 (n-Sec1) crystal structure. Three domains in arc-shaped configuration determine the protein as a hydrophilic monomer. *From (Misura et al., 2000)*. (**b**) Schematic drawing shows binding of Munc18-1 or Unc-18 to the Syntaxin-1a in closed conformation, in contrast to the yeast Sec1p binding to the SNARE complex. *From (Toonen and Verhage, 2003)*.

Requirement of the open Syntaxin-1a conformation for the formation of SNARE complexes (Richmond et al., 2001) leads to the hypothesis that Munc18-1 is a negative regulator of downstream exocytic reactions by keeping Syntaxin in the closed conformation (Sassa et al., 1999; Perez-Branguli et al., 2002). This point of view was supported by the data on the Rop homologue in *D. Melanogaster* (Schulze et al., 1994; Wu et al., 2001) where Rop overexpression resulted in inhibition of transmitter release from. On the other hand, Munc18-1 was suggested to be a positive regulator of release by promoting an essential intermediate conformation of Syntaxin before opening (Dulubova et al., 1999). The positive role of Munc18-1 in modulating exocytosis is further supported by the impaired secretion in *munc18-1/sec1* mutants (Novick and Schekman, 1979; Voets et al., 2001; Weimer et al., 2003) and functional rescue or up-regulation of fusion by introduction of excess of this protein in the chromaffin cells (Gulyás-Kovács, 2005), and also yeast (Scott et al., 2004). Another strong argument is that the open conformation of Syntaxin-1a (Unc-64) fails to rescue transmitter release in the *C. elegans* Unc18 mutant (Weimer et al., 2003), supporting an essential role for Munc18/Unc18 in promoting vesicle fusion at the step upstream from priming. The discrepancy between the positive and negative roles of Sec1 proteins in secretion may be probably resolved by assuming an activating or chaperone-like function of Munc18-1 in setting up the SNARE complex for secretion (Gallwitz and Jahn, 2003).

An indirect positive role of Munc18-1 for exocytosis may also be its effect on the Ca^{2+} channels inactivation, which is promoted by the open Syntaxin-1a, but this Syntaxin-1a mediated inhibition of Ca^{2+} influx can be relieved by Munc18-1 co-expression (Gladycheva et al., 2004; Mitchell and Ryan, 2005). Other evidence of possible effects of

Munc18-1 on the exocytotic pathway come from the following studies. Munc18-1 was shown to control Syntaxin trafficking to the plasma membrane (Rowe et al., 2001). Activation of cyclin-dependent kinase Cdk5 by Munc18 can influence the polymerization status of the cytoskeleton (Shetty et al., 1995; Veeranna et al., 1997; Bhaskar et al., 2004) which in chromaffin cells, with their pronounced sub-membrane actin cortex, can lead to up-regulation of secretion (Vitale et al., 1995; Trifaro et al., 2000). Direct interactions of Munc18-1 with its other binding partners Doc2 and Mints (Verhage et al., 1997; Hill et al., 2003) may also have a function in secretion, independent from interaction with Syntaxin (Biederer and Sudhof, 2000; Ciufo et al., 2004; Schutz et al., 2005). Several studies also suggested a role of Munc18 in the last steps of vesicle fusion, i.e. in the modulation of the fusion pore dynamics (Fisher et al., 2001; Barclay et al., 2003; Ciufo et al., 2004). The variety of possible functions of Munc18-1/Sec1 in secretion, described in the literature, is summarized in the Supplementary Table S.1.

1.5 Aims and scope of this work

The aims of this work were:

1) to apply total internal reflection microscopy (TIRFM) imaging to investigate the molecular mechanisms and different states of large dense core vesicle (LDCV) docking in neurosecretory cells;

2) to further our understanding of the role of Munc18-1 in early stages of secretory cascade, namely vesicle docking in neurosecretory cells.

All live imaging studies, investigating stages of vesicle docking in neurosecretory cells, so far described mostly morphological aspects of docking such as establishment of the contact with the plasma membrane and changes in vesicle mobility in vicinity to the target plasma membrane. On the other hand, ultrastructural, electrophysiological and molecular biological techniques often do not have sufficient temporal or spatial resolution, or provide indirect evidence on the docking mechanism in live cells. The function of the docking machinery and the molecular mechanisms underlying successful transition from the simple morphological contact between vesicle and membrane to the primed state remain poorly understood. Here, TIRFM imaging technique was used to study different states of LDCVs docking in chromaffin cells. To understand the docking steps and approach the molecular mechanisms underlying vesicle docking, chromaffin cells from the *munc18-1* null mutant mice were taken as a starting point because of the pronounced vesicle docking defect described in these cells, and the essential role of this molecule in the secretion cascade (Verhage et al., 2000; Voets et al., 2001). Two collaborating groups participated in the project: 1) Ruud F. Toonen, Heidi de Wit, Bas Konijnenburg, and Matthijs Verhage, Department of Functional Genomics, Center for Neurogenomics and Cognitive Research (CNCR), Vrije Universiteit Amsterdam and Medical Center, Amsterdam, The Netherlands; 2) Attila Gulyas-Kovacs, Jakob B.

Sørensen, Department of Membrane Biophysics, Max Planck Institute for Biophysical Chemistry, Göttingen, Germany. These two groups conducted ultrastructural electron microscopy and electrophysiology (capacitance measurements and amperometry) analysis, respectively. The data obtained in these groups were referenced in the Results and Discussion chapters of this thesis and used for interpretation of the final results.

The movement of fluorescently labeled LDCV beneath the membrane of the chromaffin cells was characterized by single vesicle tracking approach in TIRFM mode. An improved correlation analysis of axial movement (Johns et al., 2001) and an automated analysis of vesicle residency time at the membrane were developed and applied to dissect the different docking/tethering states of vesicles close to or in morphological contact with the plasma membrane. Computer simulations of different docking models assisted in interpreting the single vesicle tracking and correlation data. With pharmacological and genetic manipulations three distinct docking states were identified, and a high-affinity, Munc18-1/Syntaxin dependent tethering mechanism was suggested as an essential step preceding secretory vesicle exocytosis. Live TIRFM imaging, supported by the complementary ultrastructural morphometry and secretion assays, proved to be a very useful technique to monitor the different functional states of a secretory vesicle from the first arrival at the membrane to final fusion.

Chapter 2

Theoretical Methods and Data Analysis

2.1 Evanescent wave microscopy principles

2.1.1 The physics of evanescent waves

An evanescent wave is a special case of an electromagnetic field. Evanescent waves are generated as a consequence of the total internal reflection of the light at the interface of two different dielectrics i.e. two optical media. When an incident light beam from the first optical medium with refractive index n_1 reaches the interface to the second medium with a different refractive index n_2, the light continues into the second medium as a refracted beam at a refraction angle β different from the incidence angle α (Fig. 2.1), according to the Snell's law (2.1).

$$n_1 \cdot \sin\alpha = n_2 \cdot \sin\beta \tag{2.1}$$

In the condition when $n_1 > n_2$, a range of the incidence angles ($\alpha_{crit} \le \alpha < \pi/2$) exceeding the 'critical' angle $\alpha_{crit} = \arcsin(n_2/n_1)$ exists, at which the geometrical optics formalism breaks down and the light beam undergoes total internal reflection back into the medium of incidence (Fig. 2.1).

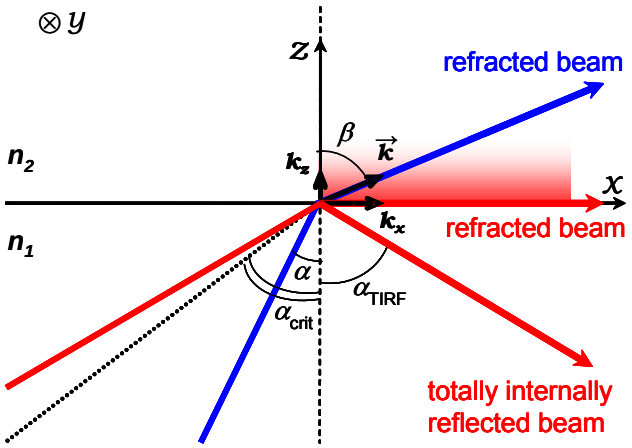

Fig. 2.1. Total internal reflection of the light beam leads to creation of the evanescent field behind the optical interface (red). In contrast, normal refraction (blue) allows propagation into the second optical medium.

However, electromagnetic wave still penetrates the interface for the limited distance, comparable to the wavelength of incident light. An analogy of 'infinitely high potential barrier' can be used to illustrate this phenomenon: photons bearing a finite positive momentum along z direction can not be instantaneously reflected from the optical interface (potential barrier) and thus the energy of the photon will leak into the second medium, rapidly decaying with the distance. Due to this effect, the evanescent field is being formed during the total internal reflection. The simplified derivation of the evanescent field equation can be performed using the wave representation of the light in conjunction with the Snell's law (Lauterborn and Kurz, 2003). The refracted plane wave

(electric component) in the second medium can be described as the sum of wave vector components along axes x and z (Fig 2.1):

$$E(\vec{r},t) = E_0 e^{i(\vec{k}\cdot\vec{r}-\omega t)} = E_0 e^{-i\omega t} e^{i(k_x x + k_z z)} = E_0 e^{-i\omega t} e^{i|\vec{k}|(x\sin\beta + z\cos\beta)} \quad (2.2)$$

where E_0 - wave amplitude, $\vec{k}$ - wave vector in the second optical medium, ω - cyclic frequency of the incident light. Using the Snell's law (2.1), $\sin\beta$ and $\cos\beta$ can be expressed as $\frac{n_1}{n_2}\sin\alpha$ and $\sqrt{1-\frac{n_1^2}{n_2^2}\sin^2\alpha}$, respectively. In the case of the total internal reflection, $\alpha_{crit} \le \alpha_{TIRF} < \pi/2$, and thus $\cos\beta$ becomes imaginary: $\cos\beta = i\sqrt{\frac{n_1^2}{n_2^2}\sin^2\alpha - 1}$ (here and below α_{TIRF} is denoted simply as α). Substitution of these expressions into (2.2) and taking into account that $|\vec{k}| = 2\pi n_2/\lambda_0$ (λ_0 - wavelength of the light in vacuum), yields (2.3):

$$E(\vec{r},t) = E_0 e^{i(\frac{2\pi n_1 \sin\alpha}{\lambda_0}x - \omega t)} \cdot e^{-z\cdot\frac{2\pi}{\lambda_0}\sqrt{n_1^2\sin^2\alpha - n_2^2}} = E_0'(z)\cdot e^{i(\frac{2\pi n_1 \sin\alpha}{\lambda_0}x - \omega t)} \quad (2.3)$$

It can be recognized from equation (2.3) that the refracted beam is a wave that propagates along the interface between the optical media (along axis x) and decays in amplitude along the z axis. The intensity of the electromagnetic field I is proportional to the squared amplitude of its electric component ($I \propto E^2$):

$$I(z) \propto E_0'^2(z) = I_0 e^{-\frac{z}{d}}, \quad d = \frac{\lambda_0}{4\pi\sqrt{n_1^2\sin^2\alpha - n_2^2}} \quad (2.4)$$

Thus, the intensity of the evanescent wave decays exponentially in the second medium with the $1/e$ constant called the penetration depth d (2.4). The penetration depth is a function of the incidence light wavelength and the refractive indexes of the two media forming the dielectric interface.

A more general description of partial reflection as well as the transition into total internal reflection is given by Fresnel's equations where a wave optics approach was used (Hecht, 2002). These equations are especially important because they describe the dependence of the interface reflectance coefficients on the polarization of the incident light and thus allow estimation of the evanescent field intensity I_0 (see 2.4) at the interface ($z = 0$):

$$\begin{aligned} I_0^{(s)} &= I_0^{(y)} = 4\cos^2\alpha\cdot\left[1-(n_2/n_1)^2\right]^{-1} \\ I_0^{(p)} &= I_0^{(x)} + I_0^{(z)} = 8\cos^2\alpha\sin^2\alpha\cdot\left[(1-(n_2/n_1)^2)\left(\sin^2\alpha - (n_2/n_1)^2\cos^2\alpha\right)\right]^{-1} \end{aligned} \quad (2.5)$$

with p- or s-polarized laser light (electric vector is in the plane xz, or parallel to the axis y, respectively). Usually, either of p- or s- configurations is used for generation of evanescent field with the laser light source in practice. In the setups described in Chapter 3, p-polarization was used.

2.1.2 Application of evanescent waves in fluorescent microscopy

As it was shown above, the total internal reflection of light produces an evanescent wave with the rapidly decaying intensity along the axis perpendicular to the optical interface. This intensity can be utilized, for example, for excitation and thus imaging fluorophores located close enough to the interface. The excitation volume is limited to a thin layer determined by d (2.4) beneath the interface. This restriction allows the elimination of background fluorescence from the distant fluorescent objects and thus enhances contrast. Due to the small magnitude of d, the axial resolution of such an approach can be uniquely high. This is the basic principle of evanescent wave microscopy, or TIRFM (total internal reflection microscopy). There are several possible practical implementations of the principle. The most commonly used are prism-based and objective-based approaches, reviewed e.g. by (Toomre and Manstein, 2001).

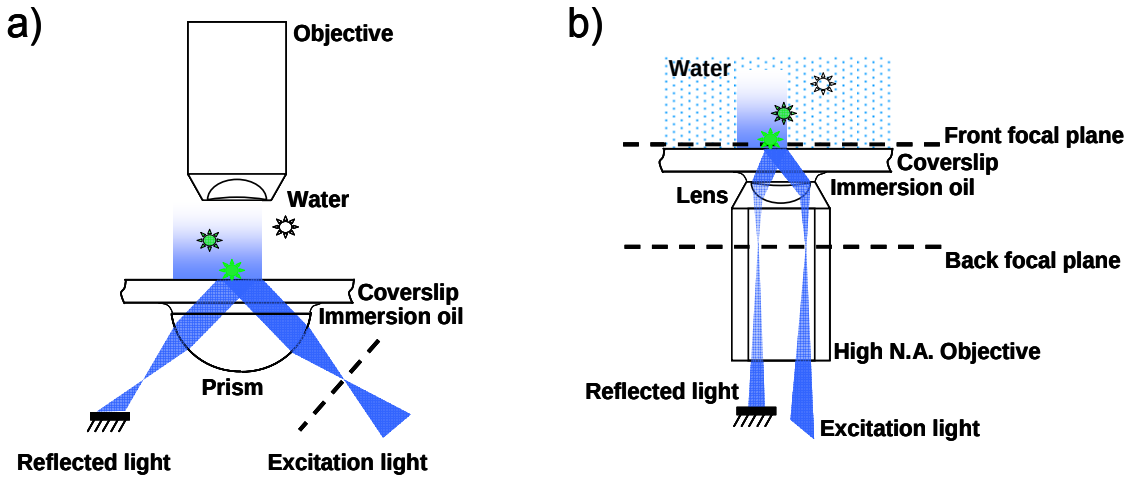

Fig. 2.2. Most commonly used configurations of TIRF microscopes: prism-based (**a**) and objective-based (**b**).

In the prism-based configuration (Fig 2.2a), the incident light beam is coupled to the interface of a glass coverslip with water-based buffer with the help of the glass prism (Axelrod et al., 1983). Detection of fluorescence can be performed from the opposite side e.g. with a water-immersion objective. The advantage of such a system based on using a hemi-cylindrical prism is that the incidence angle can be easily changed such that the penetration depth of the evanescent field d can be adjusted (so-called VA-TIRF) allowing alternative resolution in axial z-direction (Loerke et al., 2000; Oheim, 2001).

In the objective-based configuration (Fig 2.2b), the laser beam is focused to the marginal area of the back focal plane of a high-numerical aperture objective. It results in a parallel light beam leaving the objective lens at a large angle deflected from the optical axis. The immersion oil and glass coverslip serve as the optical medium guiding the beam towards the interface with the buffer of lower refractive index, as in the prism-based approach (Fig. 2.2a). The fluorescence excited by the evanescent wave at the interface is

captured by the same objective. The high numerical aperture objective lens (>1.4) is of critical importance in this configuration, because it allows large exit angles above the critical angle α_{crit} at the glass-buffer interface. The high NA is also important for fluorescence detection since the amount of fluorescent light generated using evanescent wave excitation is naturally low, and fluorescence detection efficiency is further affected by the near-field absorption, interference and reflection from the proximate dielectric interface (Burghardt and Thompson, 1984).

2.1.3 Calibration of evanescent field *in vitro*

For quantitative measurements with TIRFM it is important to know actual penetration depth constant d of the evanescent field. In the case of the objective-based TIRF microscopy, the penetration depth can be estimated by measurements of fluorescent beads at different heights from the interface (Oheim et al., 1999; Steyer and Almers, 1999), or by direct measurements of the light beam exit angle when a hemi-cylindrical prism is placed on top of the objective lens, which is equal in this case to the incidence angle α (Zenisek et al., 2002).

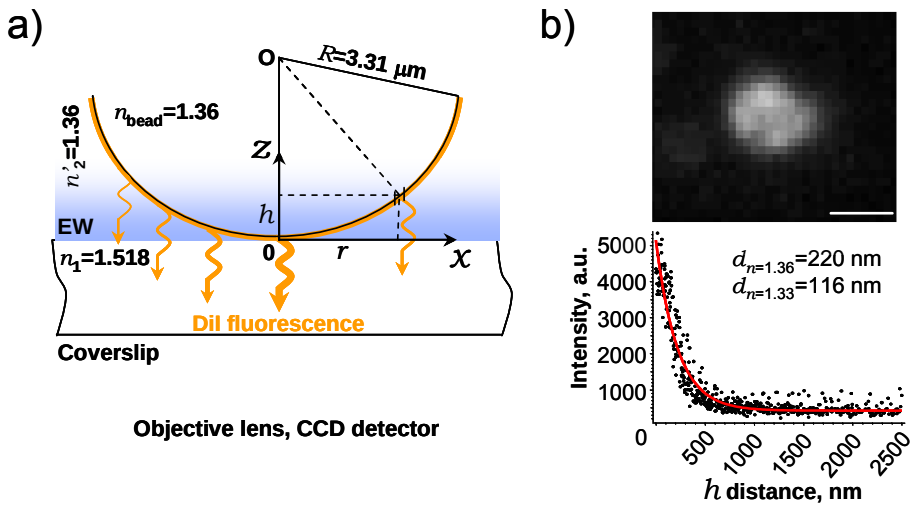

Fig. 2.3. Illustration of evanescent field penetration depth calibration principle used: (**a**) imaging large surface-coated fluorescent bead of known geometry and matching refractive index. (**b**) Exemple TIRF image of calibration bead (scale bar 2 μm) and results from fitting an exponential decay (red solid line) to the fluorescence intensity for determination of the evanescent field penetration depth.

Here, another way for penetration depth estimation was used, described first by (Mattheyses and Axelrod, 2002). The principle of this calibration method is explained in Fig. 2.3. The method is based on measuring the large silica beads of known geometry that are surface-coated with fluorescent dye (Fig. 2.3a). The beads used in calibration were 'Uniform Silica Microspheres' with average diameter of 6.62 μm (cat. SS06N, Bangs Laboratories Inc., Fishers, IN, USA). The beads were surface-coated with the fluorescent

lipophilic dye DiI (DiIC18(3), cat. D-282, Molecular Probes, Eugene, Oregon, USA). The dye was reconstituted from powder in ethanol, 1 µl of beads was mixed with 5 µl DiI solution (0.2 mg/ml) for coating, and 1 ml of 3M KCl solution was added as calibration medium. In this assay, it is important to match the refractive indexes of beads and surrounding medium in order to avoid distortions of the evanescent field at the bead surface. Thus, both beads and 3M KCl solution have same refractive indexes $n_2' = n_{bead} = 1.36$.

For calibration, the beads are allowed to settle on the cover glass and then being imaged with a CCD camera in TIRF mode while focusing at the glass-water interface. Due to the large bead radius compared to the penetration depth d of the field, only the bottom part of stained bead surface is illuminated, resulting in fluorescence images as shown exemplarily in Fig. 2.3b. Lateral coordinates of the bead center O are determined by fitting 2D-Gaussian function to the image which is subsequently used to calculate the distance r for every pixel in the image. Assuming that every pixel collects fluorescence from an equal-sized area of the bead surface exposed to an excitation intensity $I_{exc}(h)$ of the evanescent wave,

$$I(r) = A\sigma I_{exc}(h); \quad h(r) = R - \sqrt{R^2 - r^2} \tag{2.6}$$

where A-pixel area, σ- surface density of dye coating, $I(r)$-measured pixel intensity. Every pixel of the image thus can be represented by a pair of numbers: its intensity and distance h from the interface of fluorescent voxel. These pairs are plotted in a scatter plot (Fig. 2.3b) showing an expected mono-exponential intensity decay with increasing h (2.4). The penetration depth d of evanescent field can be estimated by fitting these points to a mono-exponential function with two additional free parameters: constant scaling factor (estimating the unknown constant $A\sigma I_0$) and offset (background intensity). In the calibration shown on Fig. 2.3b, d was measured to be 220±6 nm in $n_2' = 1.36$ medium. The expression for the penetration depth (2.4) can be used to re-calculate d in typical buffers as used in recordings ($n_2 = 1.33$) for a given wavelength λ_0 since the incidence angle is fixed and the same during calibration and experiment. For the case shown in Fig. 2.3b, d was 116±3 nm in $n_2 = 1.33$ and 488 nm excitation wavelength, corresponding to an incidence angle 64°36'.

2.2 Vesicle movement analysis and imaging data processing

2.2.1 Single large dense core vesicle tracking with an evanescent wave

Large dense core vesicles (LDCV) were marked using virus-mediated expression of neuropeptide Y (NPY) fused to Venus YFP fluorescent protein (Nagai et al., 2002). NPY is known to localize to and be natively secreted from chromaffin granules of the adrenal medulla in different species (Hexum et al., 1987; Bastiaensen et al., 1988), while a specific signal sequence within the protein allows targeted fluorophore expression (El

Meskini et al., 2001), which provides a tool to study single LDCVs dynamics with fluorescent microscopy (Lang et al., 1997; Perrais et al., 2004; Tsuboi et al., 2005).

The stacks of acquired images were analyzed off-line using custom-developed routines in analysis software IgorPro 4.09 (WaveMetrics Inc, Lake Oswego, OR, USA). LDCV tracking was preceded by band-pass spatial filtering in Fourier space using a Hanning window to eliminate background fluorescence and enhance the images of fluorescent vesicles. The filter window profile and an example of raw versus filtered images are shown in Fig. 2.4.

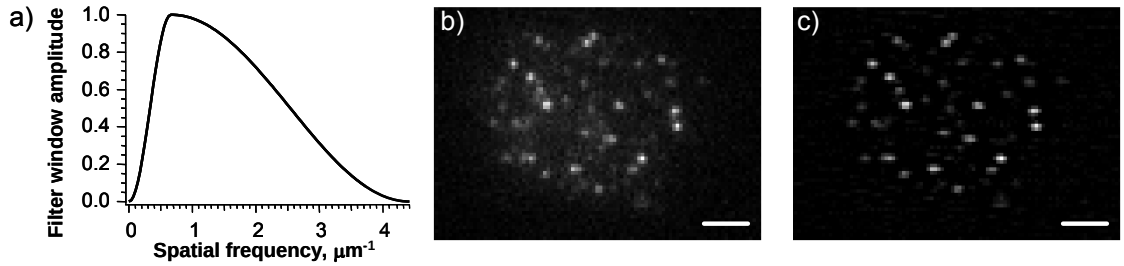

Fig. 2.4. Fourier filtering of image stacks with a Hanning window prior to single vesicle tracking. The filter profile used (**a**) allowed selective enhancement of the fluorescent signal from single-LDCV sized objects: raw image of NPY-Venus labeled vesicles (**b**) compared to the filtered image (**c**). Scale bar 2 μm.

Lateral (xy) granule position at each particular time point was determined by fitting a 2D Gaussian (2.7) to the intensity distribution in a rectangular fragment of the filtered footprint image containing only that particular granule. The 2D Gaussian fitting approach is often used and found to be reliable in many single particle tracking applications including those based on TIRFM (Steyer and Almers, 1999; Manneville et al., 2003), even though the optical point spread function in TIRF microscopy is best approximated with a 2D Lorentzian (Sund et al., 1999).

$$I(x,y) = A \cdot e^{-\frac{(x-x_0)^2+(y-y_0)^2-2\rho(x-x_0)(y-y_0)}{2(1-\rho^2)\sigma^2}} + C \qquad (2.7)$$

In fitting function (2.7), $e^{-1/2}$ width values of the 2D Gaussian along x and y axis were assumed equal ($\sigma_x = \sigma_y = \sigma$), while the correlation coefficient ρ was a free fitting parameter to account for random ellipticity of the intensity distribution due to noise. Amplitude A of the peak, local background intensity offset C and peak coordinates $(x_0; y_0)$ were the other free parameters of the fit. The Gaussian width σ was used to check the quality of tracking: results were accepted when it was on average between 100 and 200 nm (approximating the point spread function width). Additionally, xy trajectories were visually inspected for fit errors, and occasional large fluctuations for only one time point in xy trajectories were corrected by averaging two neighboring points. The same time points in z were corrected like-wise.

The intensity of LDCVs was measured from unfiltered images after background subtraction as the average of pixel intensity within a circular ROI. The ROI was drawn around every granule in the first frame and followed the vesicle center according to the measured *xy* trajectory. A background value used for background correction was measured as a time average from a large ROI outside the cell footprint. Sometimes intensity traces revealed mono-exponential decay due to fluorophore bleaching, which was determined by exponential fitting (τ >5s). This was corrected for when necessary by reverse scaling of the time course of granule fluorescence intensity with the fitted exponential curve. Due to the known evanescent field decay constant d, it was possible to extract vesicle axial coordinates from intensity traces. Assuming that a vesicle is a small sphere of radius R, homogenously filled with fluorophore at concentration C_0, positioned in evanescent field with its center at height z_0, and the incoming evanescent field is equal to the field inside the vesicle, it is possible to approximate the measured intensity of the vesicle with the integral over fluorescent volume *V* of the sphere (2.8)

$$I(z_0) = \int_{(V)} \gamma C_0 dV = \int_{-R}^{R} \gamma C_0 \cdot \pi (R^2 - z^2) \cdot I_0 e^{-\frac{z+z_0}{d}} dz = \gamma C_0 \pi I_0 e^{-\frac{z_0}{d}} \int_{-R}^{R} (R^2 - z^2) e^{-\frac{z}{d}} dz \quad (2.8)$$

where z - axial coordinate, I_0 - evanescent field maximum intensity (2.4), γ - unknown constant describing excitation and detection efficiency of the optical system. The integral in (2.8) does not depend on z_0 and can be solved analytically which results in (2.9), where $A_0 = I_{\max} = I(0)$:

$$I(z_0) = 4\pi\gamma C_0 I_0 d^2 \left[R\cosh(R/d) - d\sinh(R/d)\right] \cdot e^{-\frac{z_0}{d}} = A_0 e^{-\frac{z_0}{d}} \quad (2.9)$$

Although being an approximation, (2.9) is usually used in practice for tracking the axial coordinate of particles within the evanescent field (Steyer and Almers, 1999). The problem of axial tracking is discussed in detail, for example, in (Rohrbach, 2000). Bleaching-corrected intensity traces were used for relative z_0 position estimation at time points t_i according to equation (2.10)

$$\ln I(t_i) = \ln A_0 - \frac{z_0(t_i)}{d} \quad \Rightarrow \quad z_0(t_i) = -d \ln \frac{I(t_i)}{I_{\max}} \quad (2.10)$$

where $I_{\max}$ was the maximal measured intensity value of the vesicle. It is not known, however, to which minimal distance from the interface $I_{\max}$ corresponds for every particular vesicle, thus $z_0(t_i)$ in (2.10) gives only relative axial coordinate with unknown constant offset $z_0^{\min}$. Use of axial movement characteristics which involve differentiation of $z_0(t_i)$ (like velocity and its autocorrelation function, mean square displacement) solve the problem of $z_0^{\min}$ offset. Fig. 2.5 shows an exemplar trajectory obtained with the tracking procedure described above.

NPY-Venus labeled LDCVs in the chromaffin cells, fixed with 4% formaldehyde, and 100 nm diameter fluorescent beads (FluoSpheres 505/515, cat. F-8803, Molecular Probes, Eugene, OR, USA) settled on the cover glass at low density, were used as immobile control in vesicle tracking experiments. Immobile sub-resolution objects allow

estimation of tracking precision. Imaging parameters were chosen such that the intensity of fixed vesicles and fluorescent beads were comparable.

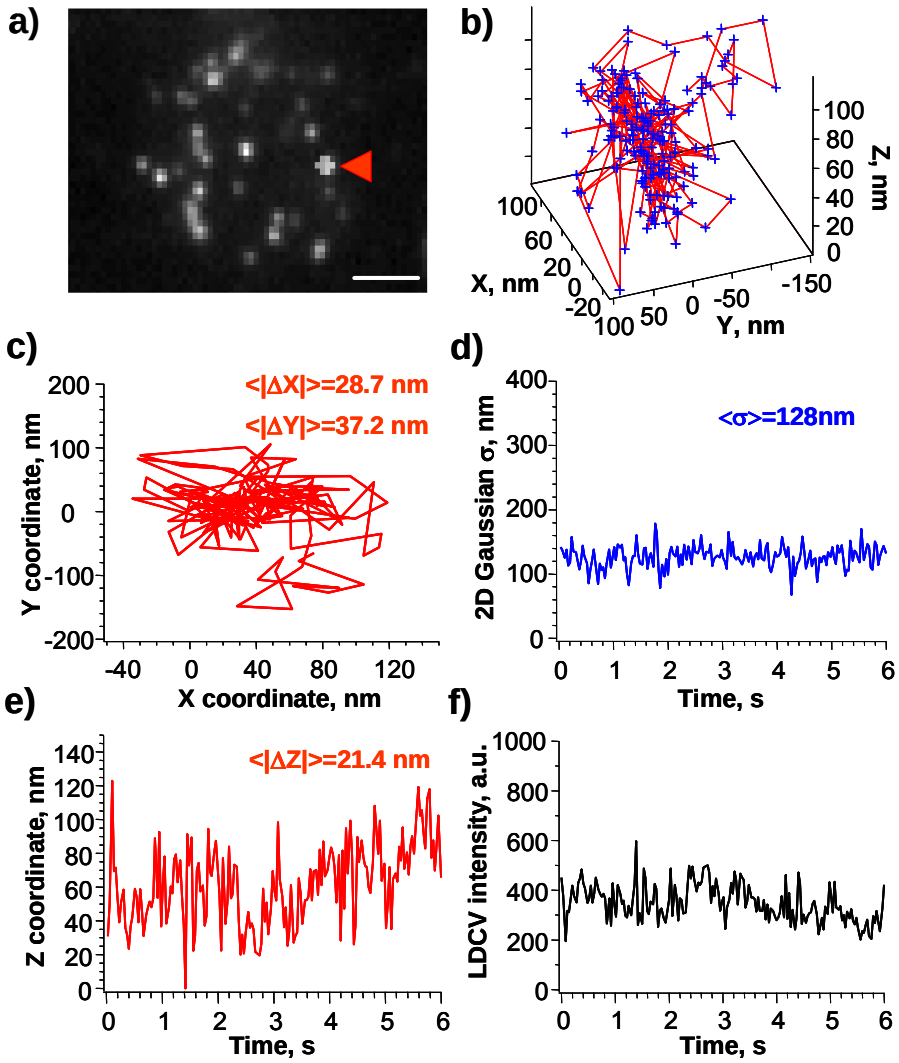

Fig. 2.5. Exemplar single LDCV trajectory determined from TIRFM image series using single particle tracking routines. A tracked vesicle is marked in the footprint image (**a,** scale bar 2 μm). The 3D trajectory of the vesicle (**b**) is determined by tracking its position in xy plane (**c**) with 2D Gaussian image fitting. (**d**) shows the value of the Gaussian width parameter in each frame, confirming convergence of the fit. (**e**) shows the projected z coordinate calculated from the vesicle intensity time trace (**f**).

The density of granules at the footprint was estimated by counting them manually in the average projection image from a 30 s image stack. The obtained number from each cell was divided by the footprint area, which was determined by intensity thresholding the average projection image (thresholding cytoplasmic fluorescent background).

2.2.2 Analysis of LDCV trajectories: mean square displacements

Mean square displacement (MSD, $\left\langle r^2(t)\right\rangle$) of the tracked vesicles over time was calculated in xy and z dimensions using equation (2.11) at high temporal resolution (δt=33 ms). MSDs were then classified into three classes: "free diffusion" (2.12a), "caged diffusion" (2.12b), "directed movement" (2.12c) based on the shape of the curves (Fig. 2.6) and fitted using functions (2.12) to determine diffusion parameters as described elsewhere (Qian et al., 1991; Steyer and Almers, 1999).

$$\left\langle r^2(t)\right\rangle = MSD(t_k) = \frac{1}{n-k}\sum_j\sum_{i=1}^{n-k}\left[r_j(t_i + k\delta t) - r_j(t_i)\right]^2 \qquad (2.11)$$

where $r_j(t_i)$ - vesicle coordinates at the time point t_i in j^{th} dimension (x, y, z, MSD is additive over dimensions), n – total number of trajectory points.

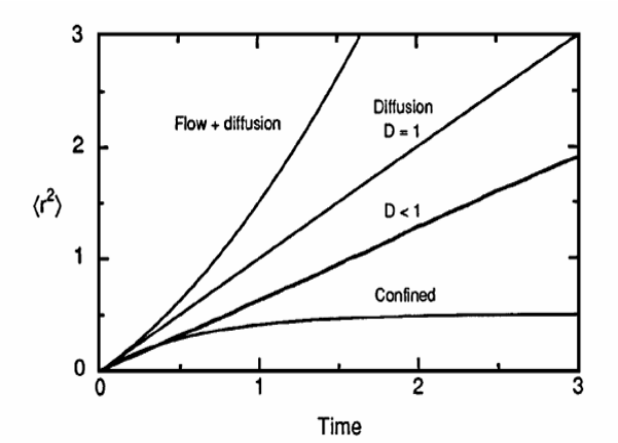

Fig. 2.6. Different shapes of mean square displacement plots over time allowing to distinguish various types of the movement: free diffusion (object displacement is proportional to time), confined diffusion space (object can not leave certain area so that the displacement saturates, revealing the volume of free space), flow superimposed on diffusion (particles have constant directed component of velocity resulting in parabolic MSD curve). *From (Saxton and Jacobson, 1997).*

$$\left\langle r_j^2(t)\right\rangle = 2mD_j t + C \qquad (2.12a)$$

$$\left\langle r_j^2(t)\right\rangle = R_j^2\left[1 - A_1\exp(-2mA_2 D_{j\alpha}t / R_j^2)\right] + 2mD_{j\beta}t + C \qquad (2.12b)$$

$$\left\langle r_j^2(t)\right\rangle = 2mD_j t + (V_j t)^2 + C \qquad (2.12c)$$

where m – number of space dimensions in which MSD was calculated; D – diffusion coefficient in free space; C – unknown constant associated with measurement error; R – cage radius; D_α, D_β - diffusion coefficients of vesicle inside the cage and of the cage itself; A_1=0.99, A_2=0.85 –fixed constants for spherical cage (Saxton, 1993; Steyer and Almers, 1999); V – speed of directed movement.

MSD fitting was preceded by subtracting an offset, measured at the first MSD point ($t = \delta t$). This offset originated from point-to-point noise, similar to the first point of ΔZ -

ACF (see below). Fitting of MSD plots was restricted to small time values (<5 s) because of the increase in error for larger observation times (Qian et al., 1991).

2.2.3 Analysis of LDCV trajectories: velocity autocorrelation function

The velocity autocorrelation function (VACF) is an important characteristic for the description of random motion. It provides information on interaction of moving particles with their environment (Qian et al., 1991). Autocorrelation of any time-dependent function uncovers the 'memory' properties of the underlying process, i.e. its repetitiveness, periodicity or randomness. In application to studies of diffusive motion, autocorrelation function can reveal deviations from pure random diffusion. Velocity and movement direction of diffusing particle can only change during interactions (collisions) with particles from the environment or borders etc. In liquids or gases, for example, these collisions are extremely fast compared to the experimental sampling interval, such that millions of interactions occur between measurements of particle velocity. This way, measured particle movement seems to be random diffusion due to the 'loss of interaction memory', or, in other words, the independence of the particle state from the previously measured time point. In this case, a velocity autocorrelation function decays rapidly to zero at correlation time $\tau > 0$ and basically acquires the shape of a Dirac delta-function (Qian et al., 1991) for an ideal measurement. In cases where interactions leading to a change of the particle movement momentum happen slowly enough, measured VACF amplitude will indicate the presence of such interactions and a the time scale at which they took place.

To my knowledge, VACF analysis was applied for studying vesicle mobility beneath the membrane in TIRFM only once in bovine chromaffin cells (Johns et al., 2001). The authors reported a negative component at τ=0.5 s in average VACF of vesicles, which was interpreted as a repetitive change of vesicle movement direction due to restrictions of vesicle movement beneath the membrane (Fig. 2.7a). At larger values of τ, VACF was expectedly decaying to zero, as well as it did for all correlation times in cases of inanimate control or random diffusion simulations (Fig. 2.7 b,c).

However, the study referenced here was more descriptive concerning VACF analysis and did not provide insight into the possible mechanisms of vesicle movement restriction. Secondly, the data presented in Fig. 2.6 may include artifacts originating from slow sampling, since image acquisition was performed at δt=0.5 s which is the time resolution of the reported VACF. It is important to note that due to the random noise at sampling frequency (point-to-point random noise in fluorescence intensity, thus in determined coordinates and velocity time traces) VACF will have large negative amplitude at $\tau = \delta t$ as demonstrated below. Here, this possible source of artifact was avoided by using a much faster sampling rate than in (Johns et al., 2001) and exclusion of the first negative point after the correlation step.

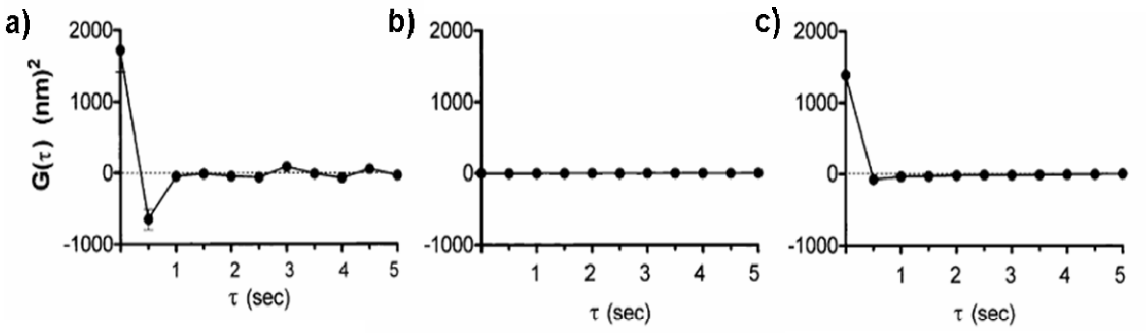

Fig. 2.7. A VACF study of restricted LDCV movement beneath the plasma membrane of bovine chromaffin cells. VACF reveals a negative component (**a**) at τ =0.5 s, indicative of repetitive changes in vesicle velocity direction. In case of immobile control (**b**, immobile dust particles) or free diffusion (**c,** random walk simulations) VACF decays immediately to zero. *Taken from (Johns et al., 2001).*

In this work, ΔZ-ACF ($\langle \Delta Z(\tau)\Delta Z(0)\rangle$) was calculated (Johns et al., 2001) instead of velocity autocorrelation, which is allowed because the timing (sampling interval $\delta t = t_{i+1} - t_i$=33 ms) was preserved in all the experiments, hence $\Delta Z \sim V_z$ and ΔZ-ACF~V_z-ACF. First differences $\Delta Z(t_i)$ of n axial Z positions, calculated as $\Delta Z(t_i) = Z(t_{i+1}) - Z(t_i)$ ($i = 0,1,2,\ldots n-2$), were used for ΔZ-ACF calculation (2.13). A circular correlation algorithm was used, and ΔZ-ACF was truncated at $\tau \geq t_{n-2}/2$ because of the symmetry of circular autocorrelation.

$$\langle \Delta Z(\tau)\Delta Z(0)\rangle = \frac{1}{n-1}\sum_{i=0}^{n-2}\Delta Z(t_i+\tau)\Delta Z(t_i) \qquad (2.13)$$

Zero ($\tau = 0$) and first ($\tau = \delta t$) points of ΔZ-ACF were excluded from the analysis because they respectively reflected the mean of the squared $\Delta Z(t_i)$ values (large positive value) and the point-to-point sampling noise (large negative value). The origin of the first negative point at $\tau = \delta t$ is explained below. As follows from the equation (2.13), the first ΔZ-ACF point is given by the expression (2.14):

$$\langle \Delta Z(\delta t)\Delta Z(0)\rangle = \frac{1}{n-1}\sum_{i=1}^{n-1}(Z(t_i+\delta t) - Z(t_i))(Z(t_i) - Z(t_i-\delta t)) \qquad (2.14)$$

It is convenient to present the coordinate trace $Z(t_i)$ in differential form: $Z(t_i) = \delta Z_i + \overline{Z}$, where $\overline{Z}$ is a time-averaged coordinate, δZ_i - positive or negative deviations from $\overline{Z}$ at each time point t_i. With this notations, $Z(t_i+\delta t) = \delta Z_{i+1} + \overline{Z}$, $Z(t_i-\delta t) = \delta Z_{i-1} + \overline{Z}$, and the expression (2.14) develops into the equation (2.15)

$$\begin{aligned}\langle \Delta Z(\delta t)\Delta Z(0)\rangle &= \frac{1}{n-1}\sum_{i=1}^{n-1}(\delta Z_{i+1}\delta Z_i - \delta Z_i^2 - \delta Z_{i+1}\delta Z_{i-1} + \delta Z_i \delta Z_{i-1}) = \\ &= 2\langle \delta Z_{i+1}\delta Z_i\rangle - \langle \delta Z_{i+1}\delta Z_{i-1}\rangle - \sigma_Z^2\end{aligned} \qquad (2.15)$$

Here, σ_Z^2 is a variance of Z coordinate. As a positive value, it produces a negative contribution into the sum. The other terms, in general, depend on the signal properties. The first two terms ($2\langle \delta Z_{i+1}\delta Z_i\rangle$ and $\langle \delta Z_{i+1}\delta Z_{i-1}\rangle$), however, have zero expectation values in case of white noise. The ΔZ-ACF points at larger $\tau > \delta t$ will not be directly

influenced by the variance σ_Z^2 in the expression (2.15) but instead by the higher-order terms containing the products of $\delta Z_{i\pm k}$ at larger time steps ($k > 1$). The first point of ΔZ-ACF is thus strongly influenced by the random noise and tends to posses large negative values (verified also with simulations of noise traces) and needs to be treated separately.

ΔZ-ACFs from individual vesicles were noisy, as also reported by (Johns et al., 2001), thus the initial sampling rate was reduced to 10 Hz by 3-points binning of intensity traces ($\delta t' = 3\delta t$ =99 ms) before running the correlation procedure. Obtained functions from each individual vesicle were further binned by 4 points in time and ensemble-averaged in order to minimize the influence of noise sources. Zero and first ΔZ-ACF points were eliminated before the binning step. The final temporal resolution of average ΔZ-ACF reported in this study is thus 0.396 s. This is not much improved time resolution of ΔZ-ACF, compared to results shown in (Johns et al., 2001), but the faster sampling rate used here allowed to exclude the sampling artifact without loss of information on real interactions. Negative persistence amplitude (NPA) was defined as a parameter to compare ΔZ-ACF between different experiments. It was calculated as an absolute value of the sum of first two points of binned ΔZ-ACFs.

The velocity autocorrelation and mean square displacement analysis (see 2.2.2) are complementary methods because they emphasize different aspects of the information contained in the ΔZ-ACF and MSD_Z plot. The connection between these functions is given by equation (2.16):

$$\left\langle r_Z^2(t)\right\rangle = \frac{2t}{\delta t^2}\cdot\left(\int_0^t \left\langle \Delta Z(0)\Delta Z(s)\right\rangle ds - \int_0^t s\left\langle \Delta Z(0)\Delta Z(s)\right\rangle ds\right) \qquad (2.16)$$

2.2.4 Analysis of LDCV residency time at the membrane

To automatically detect single vesicles, filtered stacks of TIRF images (Fig. 2.6) were subjected to a two-dimensional *à-trous* wavelet transformation (Olivo-Marin, 2002) with iteration level k =3 and detection level l_d =1.0. This transformation was shown to be effective in automated detection of spots of varying intensity from biological images (Olivo-Marin, 2002). Wavelet transformation of a single image results in a segmented mask image in which pixels from the area covering detected objects have zero intensity and non-zero elsewhere in the image as shown exemplarily in Fig. 2.8.. The transformation was applied to every image of the acquired time series, which yielded a stack of segmented masks. The spots on the mask images, each representing potentially detected vesicles, were recognized with available routines in IgorPro 4.09 (IgorPro function *ImageAnalyzeParticles*), and separate mask images for every such object were generated. Detection threshold of the routine was set to four or five (see below) pixels minimal mask area, and recognized spots were analyzed from frame to frame to track the objects with time. Lateral position of an object at each frame was determined as the center-of-intensity of all pixels covered by the corresponding mask.

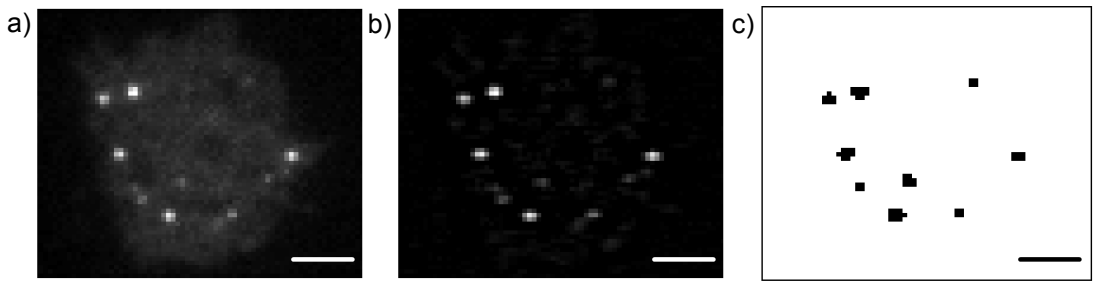

Fig. 2.8. Automated detection of vesicles using *à-trous* wavelet transformation. Raw images of NPY-Venus labeled vesicles (**a**) were first Fourier-filtered (**b**) and then subjected to wavelet transformation, yielding a segmented image mask of detected vesicles (**c**). Scale bar 2 μm.

Objects in adjacent frames whose centers moved less than 1.5 pixels laterally (threshold chosen empirically) were considered to be the same object. Objects that could not be detected for at least one frame, were scored as 'disappeared'; those not detectable on the preceding frame, were counted as 'newly appeared'. For residency time analysis, objects with life times less than or equal to two frames ($\tau \leq \delta t$=0.3 s) were excluded, since they most often represented false detection events due to the noise in images, as empirically noticed.

Further selection criteria were applied in order to remove falsely detected objects and to narrow down object detection to real fluorescently labeled vesicles. The choice of selection criteria is explained in the two following figures. First, stacks of wavelet mask images were subjected to a detection algorithm with a five-pixels threshold for minimum mask area (Fig. 2.9a-c). This threshold yielded reliable detection of masks corresponding to real vesicles, as judged by visual inspection. The scatter plots of detected object residency times (Fig. 2.9) revealed low residency time 'tails' originating from false vesicle masks. Thus only objects were selected whose time-averaged areas were between 6 and 12 pixels, circularities between 0.7 and 1.2 (calculated as $mask\ perimeter^2 / area / 4\pi^2$), and whose intensities were at least 20% higher than cytosolic background were scored as vesicles. Cytosolic background was measured as time-averaged fluorescence from the ROIs drawn at the cell footprint where no vesicles were present. Manual inspection of results obtained after applying the aforementioned selection criteria revealed that most vesicles at individual frames indeed were detected. However, the overall number of detected vesicles from the time lapse series was up to 10 fold larger than estimated visually. For example, out of 11871 detected objects in 30 cells during observation time 3 min per cell (Fig. 2.9a-c), 6111 objects were scored as true vesicles. It corresponds to the number of ~200 vesicles appearing at the footprint of each cell during 3 min observation time, which is an overestimation as could be concluded after visual inspection of original image series.

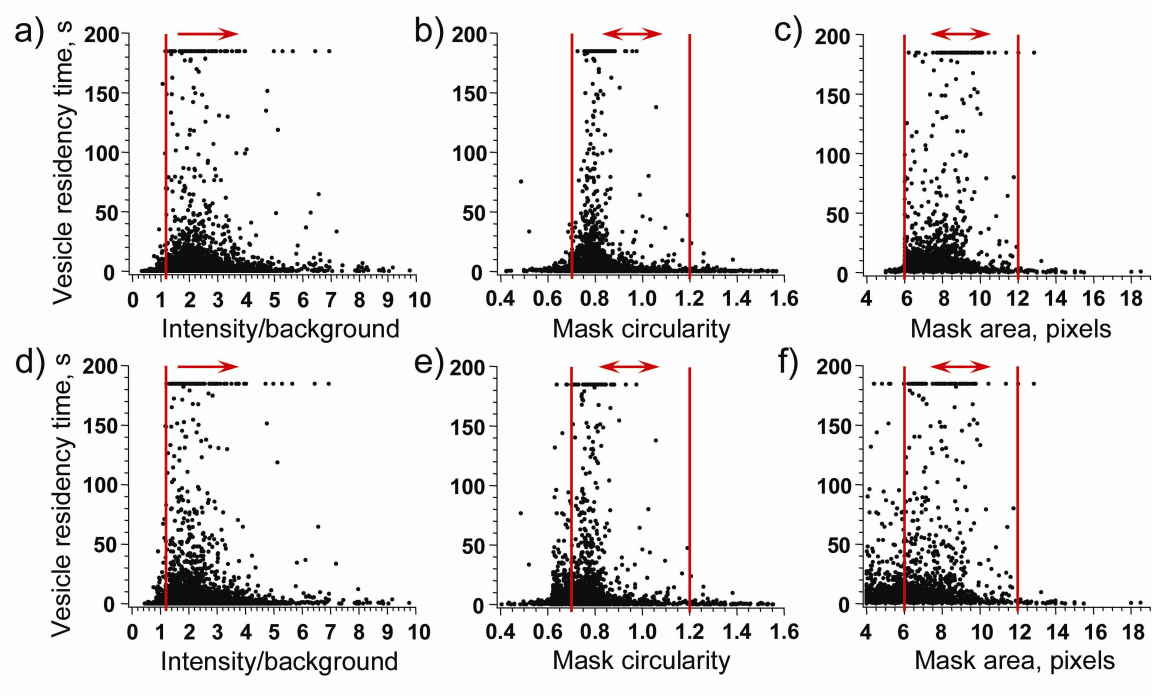

Fig. 2.9. Choice of criteria to select true vesicles from total ensemble of automatically detected objects. Object detection threshold based on wavelet mask area was set to five (**a-c**, n =11871 detected objects) or four (**d-f**, n =15541) pixels for the same data set (N =30 cells). Every dot represents a detected object in the scatter plots of residency times over time-averaged intensity-to-background ratio (**a,d**), wavelet mask circularity (**b,e**) and wavelet mask area (**c,f**). Acceptance criteria for vesicles were empirically determined from an object ensemble detected using five pixels mask threshold (a-c, red lines), and then transferred onto the four pixel thresholded ensemble (d-f); see text for further explanations.

The reason for overestimation of vesicle number with five-pixel minimal mask area threshold were random fluctuations of the wavelet mask area down to four pixels several times in the vesicle lifetime. It resulted in truncation of single vesicle residency time at these points because four pixel masks were rejected from detection, as a result of which long-lived vesicles were instead scored as several shorter lived ones.

In order to correct for this and improve detection, the sensitivity first was increased by lowering the mask area threshold to four pixels (scatters are shown in Fig. 2.9d-f). It yielded in total more detected objects (n=15541) compared to the five pixels threshold criterion due to detection of very dim events and intensity artifacts of band-pass filtering, producing small area masks (Fig. 2.9f vs c). At the same time, vesicle lifetime truncation was avoided due to high sensitivity. To keep high selectivity of the algorithm, the same vesicle selection criteria, determined from five pixels threshold detection results (Fig 2.9, red lines), were applied. This is allowed because the original wavelet masks were unchanged, and only mask area detection threshold was different in order to correct for rare vesicle time course truncation. The following calculations justify the use of 'five-pixel' selection criteria on a 'four-pixel' object ensemble. The effect of increased

sensitivity by lowering mask area threshold to four pixels can be looked at as 're-joining' truncated vesicles by insertion of four pixel masks between truncated lifetime episodes. The time-averaged areas $\langle A' \rangle$ and circularities $\langle C' \rangle$ are expected to decrease after vesicle-lifetime re-joining by insertion of, say, M four-pixel masks. However, as shown by (2.17), this decrease in areas and circularities is negligible if re-joining frequency (the ratio $M / \sum_i N_i$) is small.

$$\langle A' \rangle = \frac{4M + \sum_i \langle A_i \rangle N_i}{N'} \geq \frac{4M + 6\sum_i N_i}{M + \sum_i N_i} = 4 + \frac{2}{1 + M / \sum_i N_i} \qquad (2.17)$$

$$\textit{similarly}, \quad \langle C' \rangle \geq 0.4 + 0.3 \Big/ \left(1 + M / \sum_i N_i \right)$$

here, $\langle A_i \rangle$ - average area of i-th vesicle lifetime episode, detected with five pixel threshold; N_i - number of time points in i-th episode; $N' = M + \sum_i N_i$ - total number of points in all episodes re-joined by insertion of M four pixel masks; inequality is obtained by substitution of lower selection criteria for average area or circularity: 6 pixels and 0.7. Circularity of a square four-pixel mask is 0.4.

Application of the pre-determined selection criteria to four-pixel thresholded ensemble excluded small-area false objects and restricted the selection to objects reliably scored as vesicles. For example, analysis of the data set shown in Fig 2.9d-f yielded n'=2398 vesicles which is 3 fold less than the number of vesicles after five-pixel threshold.

Fig 2.10 shows correlation between parameters used for vesicle selection among the whole ensemble of detected objects. When the five-pixel mask area threshold was used, object intensity only very weakly correlated with time averaged object area (Fig. 2.10a): the linear correlation coefficient was ρ=0.05 among selected objects. This indicates reliable vesicle detection where mask area is determined by the object point spread function rather than by its brightness. Mask circularity correlates significantly (ρ=0.61) with the mask area (Fig. 2.10b), which is expected for such small masks. When the four-pixel detection threshold was used (Fig. 2.10c,d), the intensity also correlated only very weakly with mask area (ρ=0.21 for selected objects in red rectangle), but somewhat stronger than after five-pixel thresholding. Mask circularity strongly correlated with mask area (ρ=0.69), and small-area and small-circularity objects were not scored as vesicles according to selection criteria (Fig. 2.10d).

Vesicle detection was followed by residency time analysis. If vesicle docking/undocking reaction had several distinct states (downstream of the first morphological contact with the membrane) related to each other with first-order kinetic transitions, the distribution of vesicle residency times at the membrane (lifetime distribution of different docked states) should provide information about these docking states.

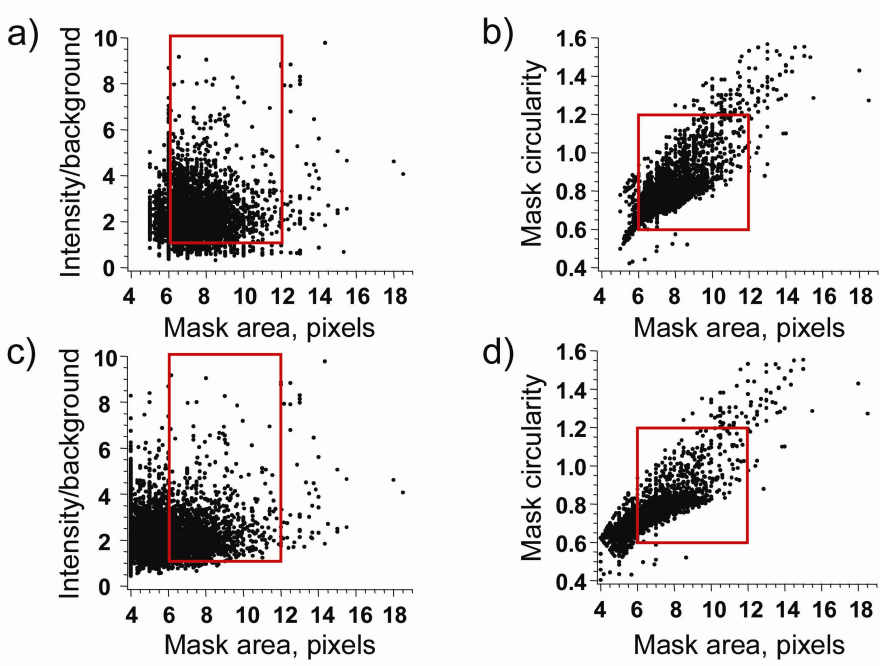

Fig. 2.10. Cross-correlations of parameters used as selection criteria for automated vesicle detection. Scatter plots of objects detected with five (**a,b**) or four (**c,d**) pixel mask area threshold (see Fig. 2.9 and text). Intensity of objects only weakly correlates with the mask area (**a,c**) while mask circularity and mask area correlate significantly (**b,d**). Red rectangles indicate selected ensembles.

In this case, single channel analysis tools can be utilized, namely analysis of histograms for channel shut times (Colquhoun and Sigworth, 1995). On the basis of these assumptions, the probability density function $f_\tau(\tau)$ of residency times in different states is a mixture of exponential distributions with characteristic mean times τ_i for each state (2.18).

$$f_\tau(\tau) = \sum_i a_i \tau_i e^{-\tau/\tau_i}, \quad \sum_i a_i = 1 \tag{2.18}$$

Before binning and displaying the residency time distribution, residency times τ underwent logarithmic transformation: $x = \ln \tau$ (Sigworth and Sine, 1987). Probability distribution functions P_x and P_τ after such transformation are identical in respective coordinates because the logarithm is a monotonic function, and thus $P_\tau(a) = prob\{\tau \le a\} = prob\{\ln \tau \le \ln a\} = P_x(\ln a)$. The histogram, approximating the probability distribution function $f_x(x)$, was calculated for logarithmic bins and plotted in logarithmic scale. This greatly facilitates identification of different docking states: the distribution $f_x(x)$ will display peaks or shoulders around the mean lifetime of each individual state (Fig. 2.11, formula 2.19). Without this procedure, it is very difficult to distinguish closely spaced lifetimes τ_i on a conventional histogram in non-transformed scale.

$$f_x(x) = \frac{dP(x)}{dx} = \frac{dP(x)}{d\ln(\tau)} = \tau \frac{dP(x)}{d\tau} = \tau \frac{dP(\tau)}{d\tau} = \tau f_\tau(\tau) = \sum_i a_i \tau_i e^{x - e^x/\tau_i} \tag{2.19}$$

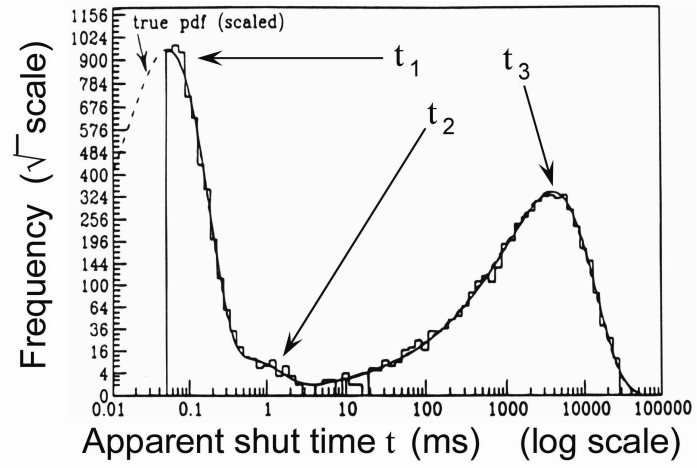

Fig. 2.11. Illustration of lifetime probability density function of ion channels with different closed states (or vesicle residency time in different docking states, in this study) after logarithmic transformation: peaks are around mean lifetime τ_i of each state. *Adapted from (Colquhoun and Hawkes, 1995).*

Obtained histograms were normalized in each cell to the footprint area of the membrane (measured by cytoplasmic fluorescence thresholding) and to the total observation time to reflect 'hit rates' of vesicles per unit area. Average occurrence of vesicles with particular residency time τ was estimated from the whole image stack by first counting the density of vesicles of that residency time at every frame of the stack, averaging obtained densities over the observation time, and finally among the cells. The average occurrence distribution thus provides an expectation value for instantaneous vesicle density at a random snapshot of cell footprint depending on the vesicle residency times.

2.3 Computer simulations of vesicle movement

As described above, mean square displacements and velocity autocorrelation functions provide information on movement restriction or on the time scale of interactions of moving particles with the environment. However, there is no information on the mechanism of interaction or movement restriction contained in these macroscopic characteristics. To be able to interpret experimental results and fundamentally understand the underlying mechanisms, experimental measurements were supplemented by computer simulations of single fluorescent particle movement.

Simulation parameters were chosen to closely match experimental parameters. A fluorescent particle (vesicle) with constant fluorescence quantum yield was allowed to diffuse in the space (intracellular environment) limited by a plane at $z = 0$ (planar coverslip or footprint forming plasma membrane). Evanescent-wave excitation light in the simulation had an exponential profile decaying from the plane of interface ($z = 0$) to $z \to \infty$ with a space constant d =120 nm. Intensity of the evanescent field at the interface

I_0 was selected such that at z_0=0 the particle had fluorescence intensity of 10^4 arbitrary units per second sampled with the hypothetical CCD detector assumed in the simulations. Actual sampling of fluorescent counts by the hypothetical CCD was done at 30 Hz, with 'exposure time' 33 ms per frame: the counts at each simulation time step were integrated between sampling read-outs. Random 'shot' noise (uniformly distributed around 0, with the maximum amplitude up to ±10% of sampled fluorescence value) was added to the sampled intensity. Resulting intensity time courses were used for estimation of particle axial position during the time course according to (2.10). Lateral $(x; y)$ coordinates were directly sampled from simulated time courses at 30 Hz synchronously with fluorescence read-out.

Particle movement was simulated using a Monte-Carlo random walk algorithm for diffusion. Diffusion constants were chosen close to experimentally measured values: $D_x = D_y$=0.05 μm^2/s, D_z=0.005 μm^2/s. The time increment in random-walk simulations was $\Delta t = 10$ μs, the spatial grid was chosen to be $\Delta x \times \Delta y \times \Delta z = 10 \times 10 \times 1$ nm. The space limiting plane $z = 0$ was reflective for the particle: it was not allowed to translocate into the volume voxels where z <0.

As test conditions, different constraints of free diffusion were applied in the described simulation set up. This is illustrated in Fig. 2.12. Mechanical constraints of the diffusion space (boxed or caged diffusion) were implemented as reflective planes positioned parallel to the interface at a certain height H (Fig. 2.12a). In another approach, free random walk diffusion was modified by mechanical forces influencing movement along the z axis (Fig. 2.12b). Two model mechanisms were introduced for generation of these forces: stochastic and elastic tethers.

In a stochastic model (Fig. 2.12c), a number N_{total} of independent 'tethers' with certain strength ς each ($0 \le \varsigma \le 1$), could switch between inactive and active states. This transition was governed with first-order reaction rates (2.20). Stochastic transitions of tethers were simulated with the same time step used for diffusion modeling according to the algorithm developed for stochastic ion channel model simulation (Clay and DeFelice, 1983).

$$C_{active} \xleftrightarrow{k_{on}, k_{off}} O_{active} \tag{2.20}$$

In their active state, tethers could influence the probability of random-walk particle translocations in z-direction by increasing the chance of a particle approaching the plane $z = 0$ (2.21).

$$p_{z-} = p_z\left(1 + \varsigma \frac{n_{active}}{N_{total}}\right), \quad p_{z+} = p_z\left(1 - \varsigma \frac{n_{active}}{N_{total}}\right) \tag{2.21}$$

Here, n_{active} is a number of active tethers at the time point of translocation. The total probability of changing z position $p_{z+} + p_{z-} = 2p_z$ was determined by diffusion coefficient D_z as in free random walk: $2p_z = 2D_z \Delta t / \Delta z^2$.

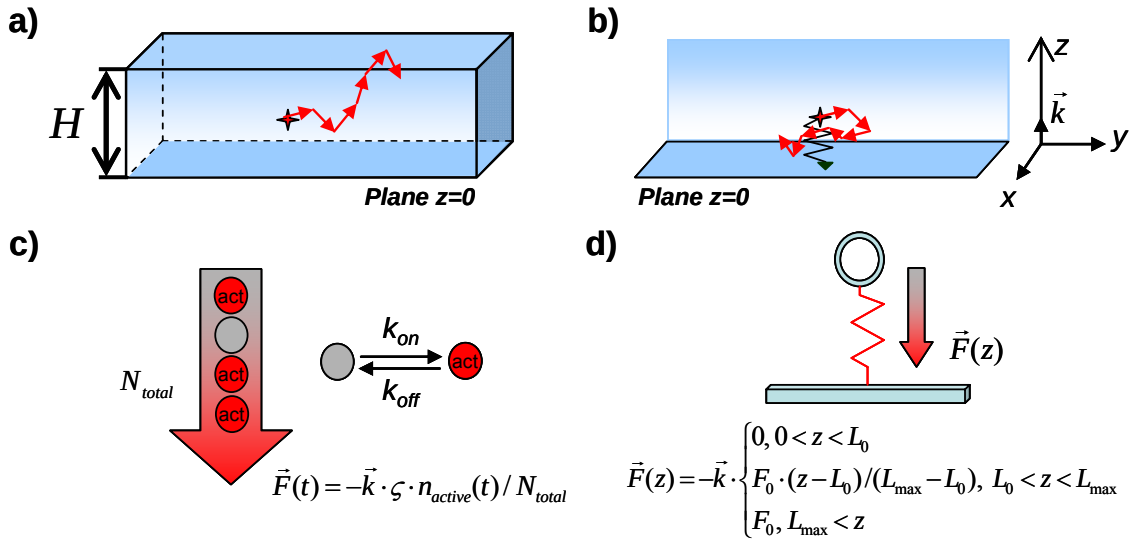

Fig. 2.12. Illustration of the models used in the computer simulation of vesicle movement in the evanescent field beneath the membrane. Mechanical constriction of diffusion space with a reflective plane at height H (**a**), or forces acting on a vesicle (**b**) were applied to modify free random walk diffusion. In case of forces, a stochastic model with several independently activating tethers (**c**) or a deterministic model involving an elastic structure (**d**) were assumed.

In a deterministic model employing elastic tethers (Fig. 2.12d), a weightless 'rubber band' was assumed with which the diffusing object was attached to the surface $z = 0$. Such a band provides a mechanical force described simply by Hooke's law (2.22). In this formula, L_0 is a free band length, $L_{\max}$ the upper limit length, and $K = F_0/(L_{\max} - L_0)$ the spring constant. In order to couple the random walk algorithm with the simulation of such an elastic band, saturation was introduced: maximum elastic force F_0 was produced if the band length exceeded the upper limit ($z \geq L_{\max}$).

$$F(z) = \begin{cases} 0, \; z \in [0; L_0) \\ F_0 (z - L_0)/(L_{\max} - L_0), \; z \in [L_0; L_{\max}) \\ F_0, \; z \in [L_{\max}; \infty) \end{cases} \qquad (2.22)$$

Elastic force simulated by (2.19) was used to modify translocation probabilities of random walk in z (2.23) as for the stochastic case.

$$p_{z-} = p_z \left(1 + \frac{F(z)}{F_0}\right), \quad p_{z+} = p_z \left(1 - \frac{F(z)}{F_0}\right) \qquad (2.23)$$

Vesicle trajectories obtained in simulations were analyzed with the same routines that were used for analysis of LDCV movement measured experimentally, as described in sections 2.2.2-2.2.3. Typically, 200 simulation trials were performed for each condition and resulting characteristics were averaged. IgorPro 4.09 software was used for computing simulation data.

Chapter 3

Experimental Methods and Materials

3.1 Imaging setups

3.1.1 Construction of a new multi-color TIRFM setup

Within the framework of this thesis, a new TIRFM setup was designed and constructed.

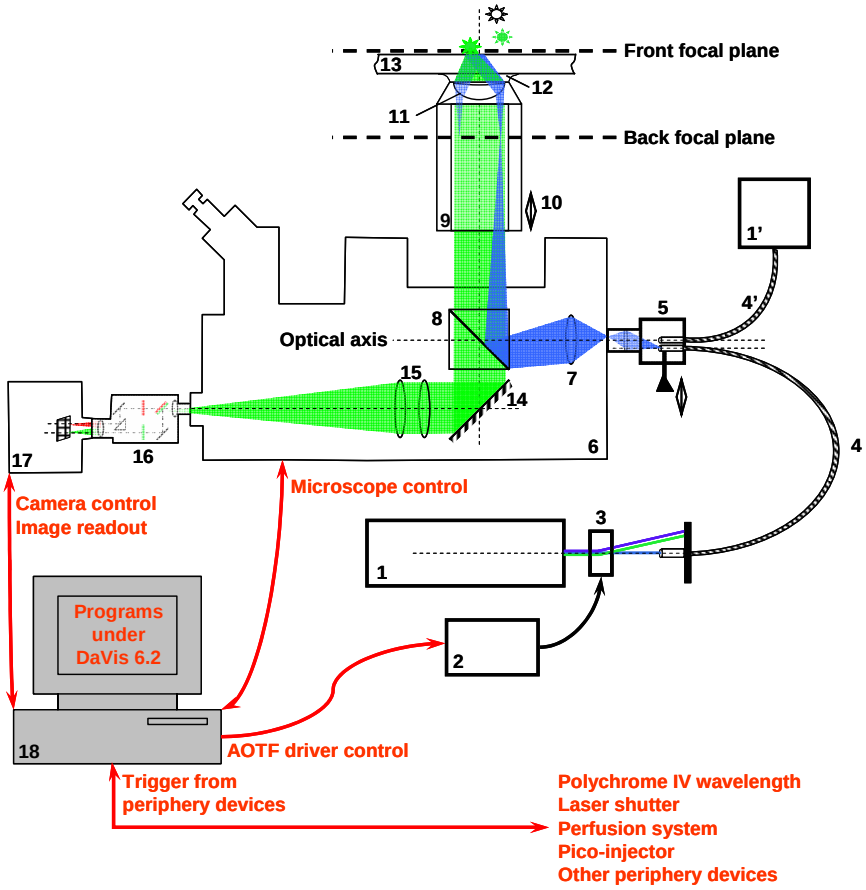

Fig. 3.1. Schematic of the constructed TIRF imaging setup. Devices and items presented in the figure: **1,1'** – laser and monochromator; **2** – AOTF driver; **3** – AOTF; **4,4'** – optic fibers; **5** – TIRF condenser; **6** – inverted microscope; **7** – microscope condenser lens; **8** – filter cube with a dichroic mirror; **9** – TIRF objective; **10** – focus drive; **11** – objective lens; **12** – immersion oil; **13** – coverslip; **14** – light path selector; **15** – tube lens system; **16** – dual viewer for two color channels; **17** – CCD camera; **18** – controlling computer. Red arrows represent hardware connections carrying control signals to/from electronic devices. See text for details and specifications.

It was designed for multi-color fluorescent imaging using evanescent wave or epi-illumination excitation, in vitro or in living cells in physiological conditions. All components of the system were selected to maximize performance in high speed imaging

low light level specimens and flexibility of experimental paradigms and applications possible. Experiments done in later part of the thesis work (e.g. vesicle lifetime analysis) were performed with this setup. The setup schematic is shown in Fig. 3.1.

Objective-based configuration of TIRFM was implemented in the setup. Multicolor excitation is possible due to the multi-line argon gas laser of H800 series (National Laser Company, Salt Lake City, UT, USA) used as a light source for evanescent wave generation (pos. 1). Monochromator of Polychrome series (TILL Photonics, Graefelfing, Germany) can be used in parallel as an excitation source in epi-illumination mode (pos. 1'). The wavelength and intensity of laser excitation light can be selected by the acousto-optical tunable filter unit AA.AOTF.nC controlled by AA.MOD.nC radiofrequency driver (AA Opto-Electronic, Versailles, France, pos. 2-3). The first-order refracted light beam from AOTF is coupled into the multimode optical fiber (Point Source, Southampton, UK, pos. 4) and guided into the TIRF condenser (TILL Photonics, Grafelfing, Germany, pos. 5). The fiber is designed for transmission of 457, 488 and 514 nm wavelengths which determines the available excitation spectrum in TIRF mode. The condenser is used to focus the light beam after the fiber output aperture and introduce a shift from the main optical axis of the system, which provides evanescent wave illumination at the sample. Monochromator generated light is coupled to the same TIRF condenser with another optic fiber (pos. 4') along the main optical axis. Excitation light from condenser is coupled into condenser lens of the inverted motorized Nikon TE2000 microscope (Tokyo, Japan, pos. 6,7), reflected from dichroic mirror in the filter cube (pos. 8) and focused (off-axis in TIRF mode) at the back focal plane of the 100×/1.45NA oil immersion objective ('Nikon TIRF', Tokyo, Japan, pos. 9). In addition to the motorized microscope focus drive, piezo-actuator PIFOC (PZT 725.10) controlled with E-662 LVPZT (Physical Instruments, Karlsruhe, Germany) is used for precise positioning of the focal plane during imaging (pos. 10). Immersion oil (Immersöl 518F, Carl Zeiss, Oberkochen, Germany, pos. 11,) is used to maintain continuous optical medium between the objective lens (pos. 12), glass coverslip (pos. 13) and a sample. Fluorescent light is collected by the objective lens, filtered with the filter cube filters, focused with the tube lenses and directed into the desired detection port with the light path selector (pos. 14-15). The dual-viewer (designed by Rainer Pick, Dept. Nanobiophotonics, MPIbpc, Goettingen, Germany, pos. 16) is attached to the left side detection port of the microscope and allows filter-based spectral separation of fluorescent image into two spectral channels. Two color channels are independently focused onto the two halves of the CCD chip for detection.

Back-illuminated EM-CCD camera (Andor DV-860, Andor Technology, Belfast, UK, pos. 17) is used for image detection. This camera provides cooling of the CCD chip to low temperatures (max -80°C; -50°C used) and utilizes a novel electron-multiplying technique for low noise amplification of extremely low light signals. The small chip size (128×128 pixels) allows high acquisition rate (up to 90 fps) in the whole-chip readout mode with reasonable image resolution (physical pixel size 24×24 μm).

The control of AOTF channels and Polychrome IV wavelength selection are performed via analog lines of I/O board (PCI-DDA04/12, Mesurement Computing, Middleboro, MA, USA) installed on the computer. The other equipment control lines as well as input triggers are wired through the TTL channels of the I/O card. Microscope is controlled via standard RS-232 serial interface.

The setup control is performed from DaVis 6.2 acquisition software (LaVision, Goettingen, Germany) running on a standard personal computer (pos. 18). DaVis 6.2 software package is an object-oriented environment which allows creation of flexible custom-written programs or dialogs on C-like language for control of camera and other devices via installed hardware adapters, software drivers or standard interfaces. A number of programs were written during the construction of the setup, aiming on flexible and user-friendly real-time control of acquisition process and all necessary periphery devices during imaging experiments. Logic structure of the created software functions and their interaction is shown in Fig. 3.2.

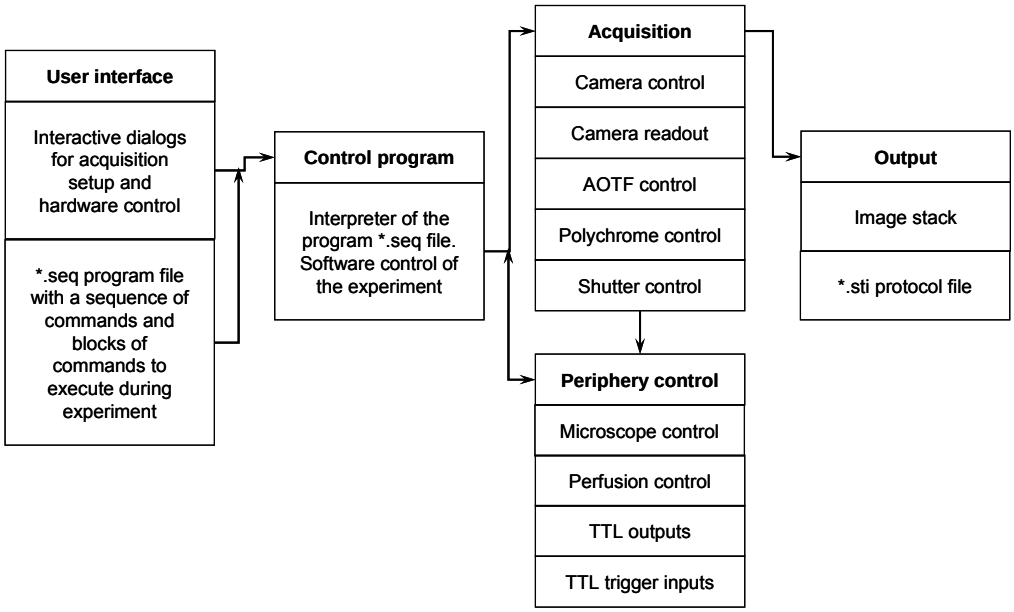

Fig. 3.2. Logical scheme of the software package developed for control of imaging experiment on the constructed TIRFM setup under DaVis 6.2.

A user can control the hardware directly in real time using interactive dialogs. The dialogs can be used for setting imaging parameters such as exposure time, EMCCD gain, background correction, chip readout ROI, excitation light intensity etc., and periphery device control (see detailed description in Appendix A).

Experimental protocol can be designed by user using developed set of commands which specify imaging parameters and hardware settings for acquisition of image stacks. The commands build up a program file, stored in a general text *.seq file. Imaging parameters, set with dialogs and protocol program file, are the inputs into the control program which compiles the command list from *.seq file and interprets a temporal

sequence of events governing the experiment flow. Flexibility is achieved by block structure of the command program, since any combination and cycles of command blocks are supported. The output of control program after acquisition is a stored image stack and *.sti file with actual time stamps for acquired images. See detailed description of programming an imaging experiment in Appendix B of this thesis.

3.1.2 Zeiss microscope and PentaMAX ICCD based TIRFM setup

Early experiments were performed on the setup described in this section, while the new setup construction (see below) was in progress.

For creating evanescent-wave illumination, a laser beam from an air-cooled argon ion laser (mod. 185-F12-NSI1266, Spectra-Physics Lasers, Mountain View, CA, USA) was guided by a single mode (488nm) optic fiber (Point Source, Southampton, UK) and coupled into the side port of TILL Photonics TIRF condenser (TILL Photonics GmbH, Graefelfing, Germany). The condenser was mounted on an inverted microscope (Zeiss Axiovert S100 TV, Oberkochen, Germany) and allowed shifting the focused light beam to the margin of the objective lens in order to obtain objective-based TIRF configuration (Fig. 2.2b). Oil immersion 100×/1.45NA objective (alpha Plan-FLUAR, Zeiss, Oberkochen, Germany) was used in generation of evanescent field. Precise positioning of the objective focal plane in TIRF mode was performed with a piezo-electric nano-positioning device PIFOC (PZT 721.10) controlled with E-662 LVPZT driver (Physik Instrumente GmbH, Karlsruhe, Germany).

As the fluorescence detector at the bottom detection port of the microscope, an intensified CCD camera (PentaMAX, Princeton Instruments, Monmouth Junction, NJ, USA) was used under control of MetaMorph Software (Universal Imaging Corporation, Downingtown, USA). The ICCD camera has an optic fiber coupling between multi-channel plate intensifier and CCD chip with the effective physical pixel size 22.5×22.5 μm.

Accessory devices (perfusion system etc.) were triggered directly by TTL signals generated under control of MetaMorph Software or indirectly via programmable pulse generator Master-8 (A.M.P.I., Jerusalem, Israel).

3.1.3 Imaging parameters and protocols used in measurements

For tracking LDCV with evanescent field, imaging was done at speed of 30 frames per second usually during 30 seconds for each cell. This regime corresponded to exposure time of 33 ms in stream acquisition mode at the setup equipped with PentaMax ICCD or 24 ms exposure time and zero inter-frame interval at the new setup. PentaMax ICCD gain was typically set to 80%, EMCCD gain factor was set to the values of 180-200. During imaging, laser power on the older setup was set to 15 mW at the power supply; on the new setup the power was set to minimum at the power supply, 488 nm line was selected

with AOTF at 3.0 V control voltage. The laser light in both cases was switched on permanently while imaging to avoid possible intensity artifacts from shuttering.

For measurements of LDCV residency time at the membrane, the new setup was used. Image stacks were acquired for 3 min from each cell. Camera exposure was 50 ms, inter-frame interval was set to 237 ms resulting in acquisition speed 3.33 frames per second. Laser light intensity at 488 nm was selected by AOTF at 2.5 V control voltage, and the excitation light was shuttered between exposures to minimize fluorescence bleaching.

Evanescent field penetration depth d was measured (as described in 2.1.3) to be on average ~120 nm and ~110 nm at the older and new setups with 488 nm light, respectively. To improve lateral resolution, an additional magnifier lens in detection light path was used (1.6× in Zeiss microscope, 1.5× in Nikon) resulting in images with 141×141 nm or 160×160 nm pixel size, acquired respectively with the old or new setup.

During imaging with 488 nm wavelength, a dichroic mirror z488 DCLP (cat. F43-500) was used. NPY-Venus fluorescence was detected with HQ 500 LP (F42-018) or HQ 535/50 (F42-001) emission filters. All filters were purchased from AHF analysentechnik AG, Tubingen, Germany.

3.1.4 Confocal microscopy

Confocal scans of chromaffin cells expressing the NPY-Venus large dense core vesicle marker were performed on a Leica SP2 confocal scanning microscope with a 63×/1.2NA water immersion objective (Leica Microsystems, Mannheim, Germany). Pinhole was set to 1 Airy disk diameter. An argon ion laser (488 nm line) was used for Venus excitation and fluorescence was detected using a built-in conventional photomultiplier detector. A dichroic mirror RSP500 was used and fluorescence was sampled in the wavelength range 520–600 nm.

3.2 Cell culture and measurement conditions

3.2.1 Embryonic chromaffin cell primary culture

Munc18-1 null mutation transgenic mouse line was obtained from Dr. Matthijs Verhage (Dept. of Functional Genomics, CNCR, Free University of Amsterdam); SNAP-25A null mutation line was provided by Dr. Jakob Soerensen (Dept. of Membrane Biophysics, MPIbpc, Goettingen). The culture of embryonic dissociated chromaffin cells was made by following the protocol described in (Nagy et al., 2002). Caesar's section was performed in sacrificed mice and embryos (age E18) were extracted. Embryos were first identified phenotypically (paralysis, subcutaneous bleeding in Munc18-1, SNAP-25A null mutants) and selection was then confirmed by DNA extraction and genotyping.

Adrenal glands were dissected and cleared of connective tissue in sterile filtered Locke´s solution (in mM: NaCl 154, KCl 5.6, NaH_2PO_4 0.85, glucose 10, pH 7.0). The

glands were washed in a droplet of sterile filtered digestion solution and then transferred into the 15 ml Falcon's tubes (two glands from one embryo per tube) containing 220 µl of solution and digested at 37°C for 40 min in a shaking water bath. Digestion solution was D-MEM (Gibco-Invitrogen, Karlsruhe, Germany) containing 20-25 units/ml papain (Worthington Biochemical Corp., Lakewood, NJ), supplemented with 200 mg/l L-cystein, $CaCl_2$ 1 mM, EDTA 20 mM, and equilibrated with bubbling 5%/95% $CO_2/0_2$ for 20 min. After digestion, papain activity was inactivated by addition of 150 µl of inactivation solution and further incubation in shaking bath at 37°C for 10 min. Inactivation solution was D-MEM (Gibco-Invitrogen, Karlsruhe, Germany) containing 2.5 g/l trypsin inhibitor (Sigma, St. Louis, MO), supplemented with 10% heat-inactivated fetal calf serum (Invitrogen San Diego, CA), 2.5 g/l bovine serum albumin (Sigma, St. Louis, MO).

After the digestion step, the medium was carefully removed from the tubes and replaced by 200 µl of pre-warmed cell culture medium. Adrenal glands were gently triturated by passing several times through a 200 µl pipette-tip opening. The obtained cell suspension was directly dispensed on 18 mm collagen-coated glass coverslips (50 µl per coverslip) in 12-well culture plates. The culture plates were left in the incubator for 20-25 min to allow the cells to settle. Cell culture medium was gently added after this step (1.5 ml/well), the cells were incubated at 37°C, 8% $C0_2$, 95% RH and used for measurements within 1-2 days. Cell culture medium was complete D-MEM containing 4.5 g/l glucose, Glutamax I and sodium pyruvate (cat. 31966-021) with 100 units/ml penicillin, 100 µg/ml streptomycin and insulin-transferrin-selenium-X (cat. 51500-056) added, all from Gibco-Invitrogen, Karlsruhe, Germany. Coating of cover glasses was performed by distributing ~80 µg/ml collagen solution (collagen type I from rat tail, BD Biosciences, Bedford, MA) over the clean glass coverslip surface. The liquid was allowed to dry, and then coverslips were rinsed once with distilled water and sterilized under UV light for 30 min.

3.2.2 Cells transfection, measurement buffers

Cultured chromaffin cells were transfected using Semliki Forest virus-mediated gene transfer, characterized on this cell type by (Ashery et al., 1999). Frozen inactive Semliki Forest viral stocks were activated by thawing in 450 µl OptiMEM-I (Gibco-Invitrogen) and protease treatment with 0.2 mg/ml chymotrypsin (Sigma) for 30 min at room temperature. Inhibition of chymotrypsin was performed by addition 0.6 mg/ml aprotinin (Sigma). Activated viral medium was aliquoted and frozen before use. Cell infection was done by adding 50 µl activated virus stock to each well containing one coverslip. The cells were used for experiments 8-10 hours after infection. Handling of viral stocks, infected cells and contaminated material were performed according to the safety level S2 requirements.

Cells were imaged in Ringer solution (in mM: 147 NaCl, 2.8 KCl, 5 $CaCl_2$, 1 $MgCl_2$, 10 HEPES, 10 D-glucose). Stimulation of cells was performed by local superfusion with high-K^+ solution (90 NaCl, 60 KCl, 5 $CaCl_2$, 1 $MgCl_2$, 10 HEPES 10

glucose) using a computer-controlled perfusion system (SF-77B, Warner Instruments, Hamden, CT). Osmolality of all solutions was 305-310 mOsm, and the pH was adjusted to 7.35.

3.2.3 Pharmacological treatments

Phorbol esther PMA (phorbol-12-myristate-13-acetate) and its PKC activation deficient analog 4α-PMA (Biotrend Chemikalien, Köln, Germany) were reconstituted in dimethyl sulfoxide (DMSO, Sigma), aliquoted and stored frozen in 1 mM stocks. PMA and 4α-PMA were applied to the cells in measurement buffer at 100 nM final concentration. Measurements were performed immediately.

Latrunculin A (cat. 428021, Calbiochem-Merck Biosciences, Bad Soden, Germany) was reconstituted in DMSO, aliquoted and stored in frozen 10 mM stock. It was applied to cells in measuring buffer at 1 μM final concentration. Measurements started 10 min after application.

3.3 Cloning of Semliki Forest viral vectors

All Semliki Forest virus constructs made within the framework of this thesis, were cloned based on pSFV1-RBN backbone DNA plasmid (designed by Dr. Ralf Nehring). In most constructs, poliovirus internal ribosomal entry site (IRES2) sequence was used to drive expression of LDCV fluorescent marker fusion protein NPY-Venus (Nagai et al., 2002). Use of the IRES sequence allowed expressing bicistronic messages which results in simultaneous expression of the protein of interest (usually placed in front of IRES site) and NPY-Venus marker. As a control virus for only marker expression, a single message construct pSFV-NPY-Venus or bicistronic construct without open reading frame in front of the IRES site (pSFV-IRES-NPY-Venus, see below) were used.

For simplifying the subsequent cloning strategy, pSFV-IRES-NPY-Venus plasmid was first cloned, where *SmaI/BamHI* restriction site in the linker region between NPY and Venus, present in original pSFV-NPY-Venus construct (provided by Ira Milosevic and inherited by pSFV-munc18-1-IRES-NPY-Venus plasmid produced by Dr. Ruud Toonen, Dept. of Functional Genomics, CNCR, Free University of Amsterdam), was deleted by targeted DNA sequence point mutation. For this, the IRES-NPY-Venus sequence was amplified from pSFVli-munc18-1-IRES-NPY-Venus plasmid (Dr. Ruud Toonen) in two overlapping parts in two PCR reactions. Primer sets used for the first reaction were: forward GGG-CTG-GCT-CCC-TTC-CCA-CAA-TGC, reverse GGG-CCC-GA*G-ATC-CAC-CGG-TCG-CCA-CC; for the second reaction: forward GTG-GAT-CT*C-GGG-CCC-GCG-GTA-CCG-T, reverse GGG-CGG-GCT-TTA-CTT-GTA-CAG-CTC. Bases marked with asterisk target the necessary mutation. Two products were fused at overlapping fragments in a fusion PCR reaction and then amplified with forward primer from the first reaction and reverse primer from the second reaction. The IRES-NPY-

Venus product was ligated blunt into the pSFV1-RBN backbone, cut with *SmaI*, and clones with the correct orientation of the insert were selected after analytical digest with *SapI*.

The sequences for expression of proteins of interest were sub-cloned into obtained pSFV-IRES-NPY-Venus plasmid DNA upstream of the IRES sequence.

Tetanus toxin light chain sequence (TeTx, a kind gift from Dr. T. Südhof, Howard Hughes Medical Institute, Dallas, TX, USA) was cut out from the plasmid pCMV5-phGHCMVTeTx (Sugita et al., 1999) with *EcoRI-HindIII* enzymes, restricted ends were filled-in using T4 DNA Polymerase and ligated blunt into pSFV-IRES-NPY-Venus backbone cut with *PmeI*. Insert orientation was checked with *XbaI* analytical digest.

Botulinum neurotoxin C light chain sequence (BoNTc, a kind gift from Dr. T. Galli, INSERM, Paris, France) was cut out from the plasmid with SacI-PstI enzymes, restricted ends were filled-in and ligated blunt into pSFV-IRES-NPY-Venus backbone cut with *PmeI*. Insert orientation was checked with *SapI-XbaI* analytical digest.

Munc18-2 DNA was PCR amplified from pSFVli-EYFP-C1-munc18b plasmid (Dr. Ruud Toonen) with following primers: CGG-GAT-CCA-TGG-CGC-CCT-TGG-GGC-T (forward), TGG-CGC-GCT-CAG-GGC-AGG-GCC-ACA-C (reverse). PCR products were ligated between *BamHI* and *BssHII* restriction sites into pSFV-IRES-NPY-Venus backbone.

SNAP-25A WT, SNAP-25B WT, SNAP-25A (M71A; I192A) DNA sequences were cut from pSFV1-SNAP-25x-IRES-EGFP plasmids (obtained from Drs. Gabor Nagy, Jakob Soerensen) with *BamHI-BssHII* enzymes and ligated into pSFV-IRES-NPY-Venus backbone.

pSFVli-munc18-1-IRES-NPY-Venus and pSFVli-munc18-1(D34N; M38V)-IRES-NPY-Venus constructs were made by Dr. Ruud Toonen. All DNA primers were ordered from IBA GmbH, Göttingen, Germany. Obtained plasmid DNA clones were verified by direct sequencing. Viral particles were made from purified plasmid DNA by Dirk Reuter, according to the standard protocol of Semliki Forest virus particle production.

Chapter 4

Results

4.1 Evanescent-wave imaging of large dense core vesicles in Munc-18 null mutant chromaffin cells

4.1.1 Characterization of NPY-Venus labeled large dense core vesicles

In this work, neuropeptide Y fused to Venus fluorescent protein (NPY-Venus) was used to selectively label large dense core vesicles in embryonic chromaffin cells. As shown in several other studies (Lang et al., 1997; El Meskini et al., 2001; Perrais et al., 2004; Tsuboi et al., 2005), the NPY-Venus fusion construct is specifically targeted to secretory organelles when expressed in bovine chromaffin or other secretory cell types. Here, fluorescence microscopy was used to test NPY-Venus targeting into functional large dense core vesicles (LDCV) of murine embryonic chromaffin cells. In Fig. 4.1a, an exemplar confocal Z-stack of a wildtype (WT) chromaffin cell is shown 8 hours after infection with NPY-Venus Semliki Forest virus. Vesicles appear as bright small (sub-resolution) structures located at or near the plasma membrane. They are typically aligned at the cell horizontal section periphery (Z=2.17-4.33 μm) or found mainly at the bottom or top sections (Z=0-1.08, 5.41 μm), locations which correspond to the 'footprint' and topmost cell membrane areas. The cell 'footprint' is the area of the plasma membrane in contact with the supporting cover glass. In TIRF microscopy, the footprint membrane is selectively illuminated with an evanescent wave. An exemplar TIRF image of a footprint formed by NPY-Venus expressing embryonic chromaffin cell is shown in Fig. 4.1b.

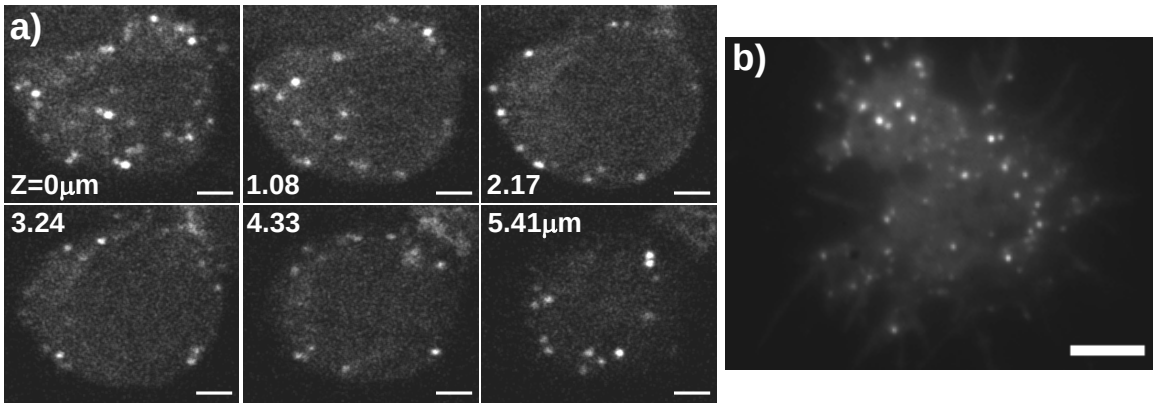

Fig. 4.1. NPY-Venus labeled large dense core vesicles in control murine embryonic chromaffin cells. (**a**) Confocal Z-sections of an infected chromaffin cell. Z=0 corresponds to the cover glass plane. Labeled granules reside mostly at the plasma membrane. (**b**) An example of an NPY-Venus expressing chromaffin cell footprint imaged with TIRFM: bright sub-resolution objects resolved from the cytosolic background are LDCVs. Scale bars are 2 (a) and 5 (b) μm.

Due to the properties of evanescent wave illumination, the vesicles visualized with TIRFM are those located within ~200 nm of the glass-cell interface, and thus of the plasma membrane, which makes TIRF an excellent tool to specifically study the docking of vesicles to the plasma membrane. Note that significant cytoplasmic Venus fluorescence both in confocal and TIRFM images may be caused by strong Semliki Forest virus mediated expression of NPY-Venus, which is faster than the NPY packaging rate into LDCV.

To prove that vesicles labeled with NPY-Venus are functional and ready to fuse upon stimulation, the following experiment was performed. The cells were stimulated by local superfusion with high-K^+ solution containing 5 mM Ca^{2+} while TIRFM images were acquired at 30 Hz frame rate. Occasionally, some NPY-Venus containing vesicles increased their intensity after stimulation onset and then 'burst' which appeared as a lateral spread of fluorescence (Fig 4.2b). Such behavior has previously been characterized in detail in different model systems and using different vesicle markers (Michael et al., 2004; Perrais et al., 2004; Taraska and Almers, 2004) and was shown to be a result of vesicle fusion with the plasma membrane.

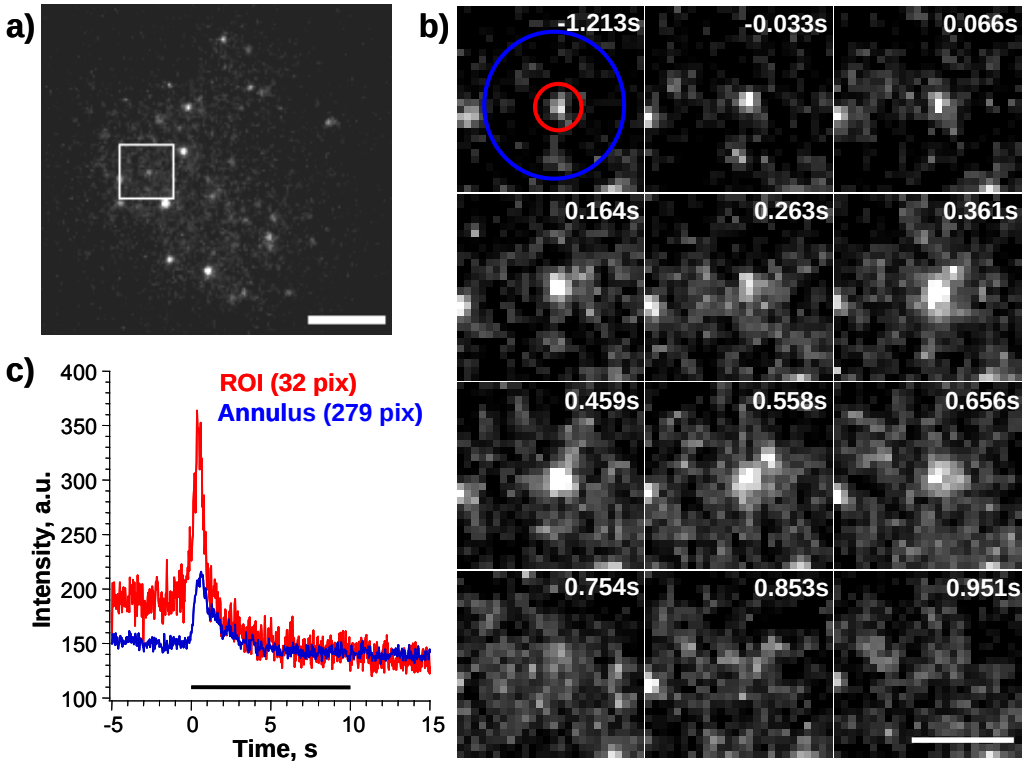

Fig. 4.2. Stimulated fusion of NPY-Venus containing LDCVs with the plasma membrane. (**a**) A snapshot from a time lapse TIRFM image series of the chromaffin cell footprint. The region marks a fusing vesicle. (**b**) Zoomed in time lapse images of the fusing vesicle. Time point at 0 s corresponds to the stimulus onset. The red ROI is used to measure vesicle fluorescence intensity and the blue ROI is used to measure the lateral spread of the fluorescent vesicle cargo after vesicle fusion. (**c**) Time trace of NPY-Venus fluorescence measured from fusing vesicle (red) and circular annular region centered on the vesicle (blue). Black bar shows application of 60 mM K^+/5 mM Ca^{2+}. Scale bars are 5 (a) and 2 (b) μm.

The transient fluorescence increase (Fig. 4.2c, red trace) is due to fluorophore molecules approaching the membrane together with the vesicle, and fluorescence de-quenching upon fusion pore opening and proton outflux from vesicle lumen. The lateral spread of fluorescence occurs when the vesicle collapses into the plasma membrane and the cargo can diffuse laterally under the footprint (Fig. 4.2c, blue trace displays the fluorescence from the annular region indicated in 4.2b).

The NPY-Venus labeled dense core vesicles were utilized in this work for studying mechanisms of vesicle docking. Thus, it is important to verify the correspondence of the labeled vesicles which were observed with TIRFM with the releasable vesicle pool which could be measured using electrophysiological approach. One possible way to check this is to estimate the fusion rate of NPY-Venus vesicles upon high-K^+ stimulation. This was done by simply counting the fusion events in stimulated chromaffin cells, hallmarked by the post-fusion lateral diffusional spread of the NPY-Venus. The frequency of fusion was obtained from normalization by the cell number and total stimulation time, probability of fusion was calculated as a number of fused vesicles normalized by the total number of observed vesicles. The main mutant phenotype studied in this work is the Munc18-1 null mutant (Verhage et al., 2000). The Munc18-1 null mutant (M18 KO) is also a good negative control for measurements of vesicle fusion rate, since exocytosis in M18 KO chromaffin cells is strongly reduced compared to wildtype (WT) cells (Voets et al., 2001). Vesicle fusion rate estimation was performed also for the null mutant cells overexpressing wildtype Munc18-1 (KO+M18-1, or Rescue) or mutated Munc18-1$^{D34N;M38V}$, and WT cells overexpressing wildtype Munc18-1 (WT+M18-1). The results are summarized in Table 4.1.

Table 4.1.

Genotype	Number of cells	Number of vesicles	Fused vesicles	Frequency, ves·(cell·min)$^{-1}$	Fusion probability
M18 KO	16	159	<1	<0.0031	**<0.0063**
Rescue	9	297	10	0.2222	**0.0337**
WT	14	424	7	0.0278	**0.0165**
WT+M18-1	22	147	6	0.0248	**0.0408**
M18$^{D34N;M38V}$	39	866	3	0.0038	**0.0035**

Although the complete fusion of vesicles (events revealing lateral spread of fluorescent cargo) is rare in absolute numbers, the fusion probability correlates with the secretion rates measured from cells of the same phenotype using amperometry and capacitance measurements of exocytosis (Gulyás-Kovács, 2005): M18 KO cells had barely detectable secretion, which could be rescued to high levels (larger than in heterozygotes) by Munc18-1 overexpression. Here, a similar phenotype was found by using TIRFM imaging to monitor NPY-Venus vesicle fusion. No NPY-Venus vesicle bursts were observed, while the null mutant cells overexpressing wildtype Munc18-1, in

addition to the high triggered fusion rate, often produced spontaneous vesicle fusions beyond the time window of stimulation. Expression of Munc18-1$^{D34N;M38V}$, bearing a double point mutation which abolishes its binding to Syntaxin-1 (Naren et al., 1997), resulted in almost ten-fold lower fusion rate of NPY-Venus vesicles. Similarly, Munc18-1$^{D34N;M38V}$ was found to be less effective in rescuing secretion than the wildtype protein (Gulyás-Kovács, 2005).

In spite of the fact that these results demonstrate viability of NPY-Venus labeled vesicles and provide a basis for use of this marker, vesicle fusion can not be used as feasable readout in studying low secretion phenotypes, and thus LDCV fusion is not the main focus of this study.

4.1.2 LDCV density at footprint as a measure of vesicle docking

Evanescent wave microscopy allows selective imaging of near-membrane fluorescent vesicles at the cellular footprint. Here a simple approach was used to estimate the amount of vesicles located close to the plasma membrane, by counting vesicles in a time-averaged footprint image as described in 2.2.1. This method was also used in another study to determine vesicle docking deficiency (Tsuboi et al., 2005). Figures 4.3a-c show representative time-averaged (over 30 s) footprint images of WT, M18 KO and Rescue chromaffin cells expressing NPY-Venus.

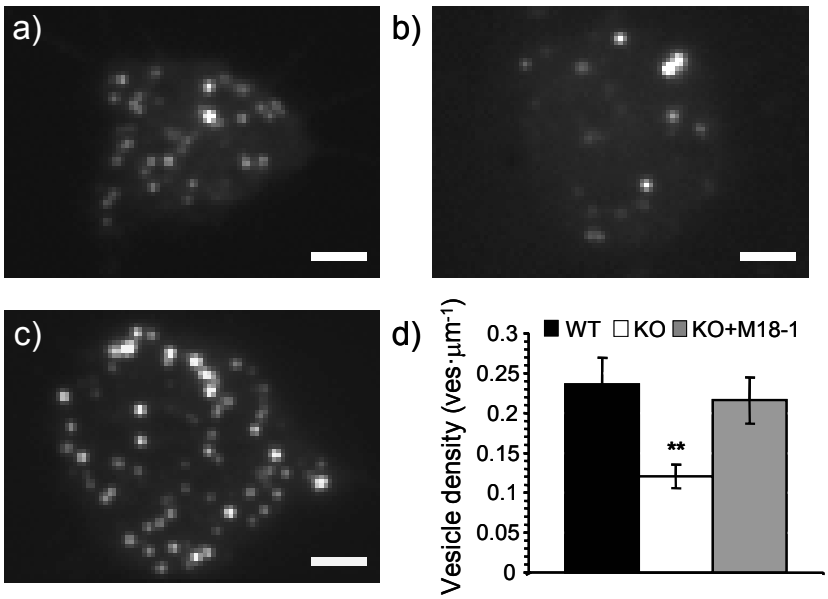

Fig. 4.3. Density of large dense core vesicles at the footprint of chromaffin cells. Time-averaged exemplar footprint images of a WT (**a**), M18 KO (**b**) and KO+M18-1 (**c**) chromaffin cells expressing NPY-Venus. The density of granules per footprint area is quantified in (**d**): it is decreased in KO compared to WT and rescue cells. Scale bars are 2 μm; (**) corresponds to $p<0.005$ (Wilcoxon test).

Quantification of LDCV density per cell footprint unit area shows an approximately two-fold decrease of the near-membrane vesicle population when munc18-1 gene is deleted. This effect could be rescued by overexpression of Munc18-1 in null mutant cells (Fig. 4.3d). These results suggest that Munc18-1 can alter the spatial distribution of vesicles inside the cell and promote their accumulation at the plasma membrane (as shown in Fig. 4.1a).

The characterization of the axial distribution of vesicles with evanescent-wave imaging is not unambiguous. The evanescent field has a space constant d ~120 nm in the setup used, thus the effectively illuminated depth is larger than a single vesicle diameter (80-100 nm). Also, the problem of the unknown $z_0^{\min}$ zero offset (see sub-section 2.2.1) does not allow accurate determination of absolute axial coordinates of vesicles.

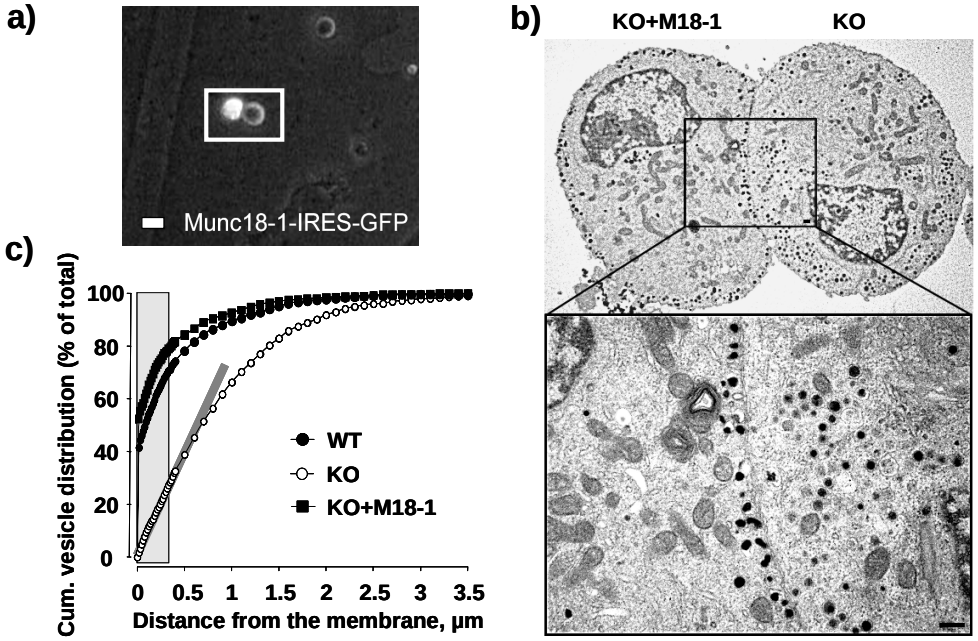

Fig. 4.4. Large dense core vesicle distribution in Munc18-1 null mutant chromaffin cells. (**a**) Fluorescent image of M18 KO cells infected with munc18-1-IRES-EGFP construct: successfully transfected cells expressed EGFP fluorescence. Scale bar 10 μm. (**b**) Electronmicrographs of the same cells (white box in **a**), one of which (left) is infected to induce Munc18-1 expression and shows an increase in docked vesicles. The uninfected null mutant cell (right) shows severely impaired vesicle docking. Scale bar 200 nm on magnified panel. (**c**) Cumulative plots of vesicle distribution in WT, KO and null cells after acute overexpression of Munc18-1. The grey line emphasizes the linear relation between vesicles and distance over the first 0.5 μm in M18 KO. The rectangular box covers three evanescent wave space constants $3d$ ($1/3e$ intensity drop). *Figure provided by Dr. Heidi de Wit*.

For this reason, all experiments performed here with TIRF microscopy were corroborated with electron microscopy measurements of the intracellular LDCV distribution (Dr. Heidi de Wit, Dept. of Functional Genomics, CNCR, Free University of Amsterdam). Fig 4.4

shows the results of electron microscopic quantification of LDCV docking in M18 KO versus WT and Rescue cells. The effect of munc18-1 deletion on vesicle distribution is indeed striking and can be visually appreciated in Fig. 4.4b (dark stained structures are LDCVs). Vesicles are scattered inside the cytoplasm in KO cells and acquire a membrane-associated phenotype (like in WT cells, Fig. 4.1a) upon rescue with Munc18-1 overexpression. High-resolution quantification of vesicle-to-membrane distances reveals almost perfectly random vesicle distribution in KO cells without detectable offset (Fig. 4.4c), while WT and Rescue cells demonstrated ~50% offset at zero distance due to vesicle accumulation at the plasma membrane. Assuming that in the vesicle density estimation method used in this work the vesicles can be detected from $\sim 3d$ layer beneath the plasma membrane, TIRFM and EM analysis reveal similar quantitative results. Electron microscopy also reveals approximately two-fold difference in submembrane vesicle population between WT/Rescue and M18 KO cells (compare areas under distribution curves in Fig. 4.4c, selected by the rectangular box of $3d$ thickness). The total number of vesicles in all experimental conditions was not significantly different from the control, as shown by EM. These findings validate the use of TIRFM-based method for estimation of vesicle docking.

4.2 Tracking large dense core vesicles with evanescent wave microscopy in Munc18-1 null mutant chromaffin cells

4.2.1 Characterization of large dense core vesicles lateral (xy) movement

Evanescent field imaging, in contrast to electron microscopy, provides the opportunity to study dynamics and movement of single vesicles in living cells. In this work, movement of individual vesicles was studied in Munc18-1 null mutant versus wildtype chromaffin cells using single particle tracking techniques with high temporal resolution (as described in the sub-section 2.2.1). Lateral trajectories (xy plane) of vesicles in all trials most often had confined shape, i.e. the vesicle did not leave a certain area but rather showed jittering movement during observation time (see e.g. Fig. 2.5c). It is difficult, however, to characterize the speed and nature of movement from the raw trajectories. Quantification of movement parameters such as the diffusion coefficient was first performed using mean square displacement (MSD) analysis, as widely used in single particle tracking (see theory in the sub-section 2.2.2). Fig. 4.5 summarizes the results of MSD curve fitting for vesicles tracked in M18 KO, WT and Rescue cells. Immobile controls (vesicles in fixed cells and fluorescent beads) were analyzed in order to determine tracking precision. MSD results for lateral movement from these and the other experimental conditions examined in this work are summarized in Supplementary Table S.2.

Exemplary MSD plots calculated from two NPY-Venus vesicle xy-trajectories are shown in Fig. 4.5a,b. The trajectory of a vesicle was classified by the shape of the MSD

(see Fig. 2.6) into 'confined' or 'free' types of diffusional motion. MSD plots fitted with theoretical models (2.12) resulted in curves shown in red, and returned parameter values estimating the cage size and diffusion coefficients (Fig. 4.5a,b).

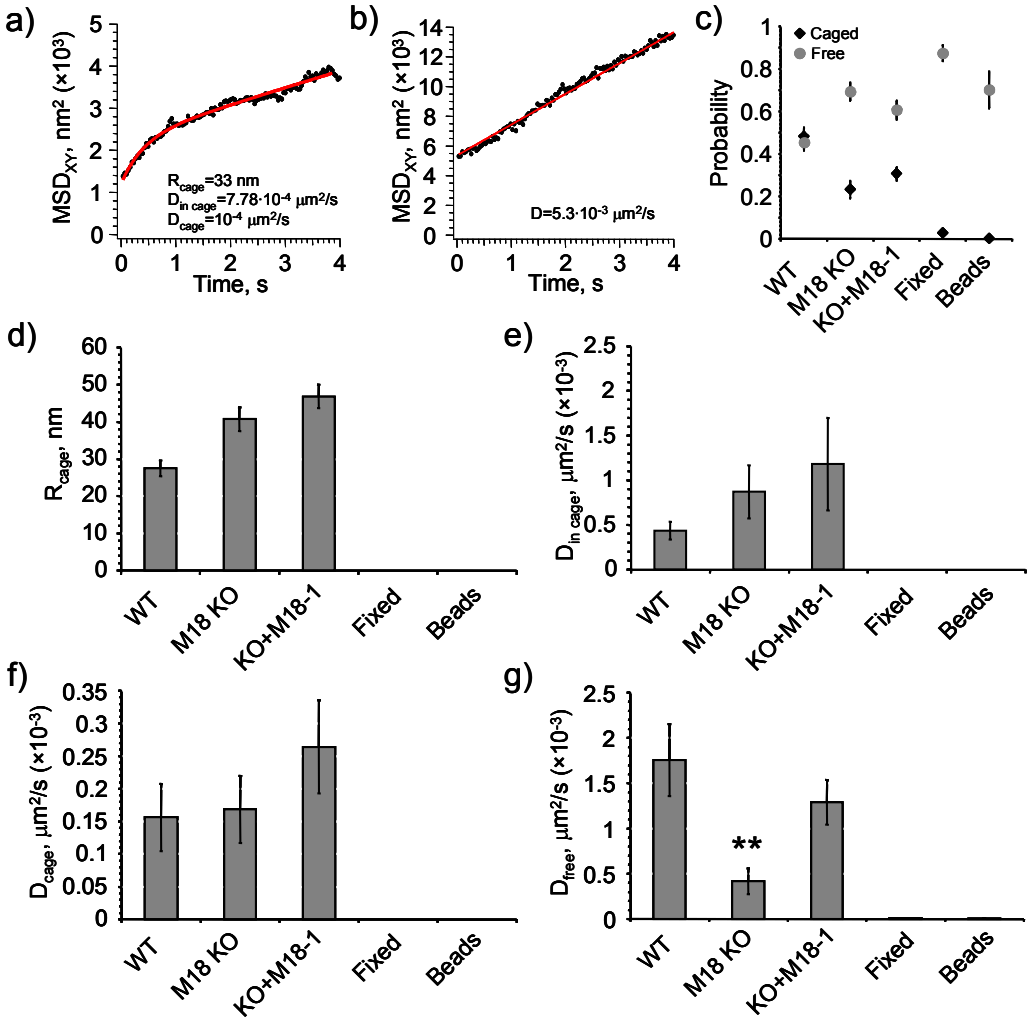

Fig. 4.5. Summary of mean square displacement analysis for vesicle lateral diffusion in M18 KO chromaffin cells. (**a,b**) Exemplar MSD plots measured from two NPY-Venus vesicles, fitted respectively with 'caged' and 'free' diffusion models. Majority of vesicles displayed 'free' diffusion MSD as shown by cell-wise average probability to meet different MSD shapes (**c**). Average confinement cage radius (**d**), diffusion coefficient of vesicle inside the cage (**e**) and diffusion coefficient of the cage itself (**f**) show no significant differences between phenotypes (also see text for explanations). (**g**) Free diffusion coefficient of the vesicles is decreased in M18 KO cells compared to WT and Rescue cells ($p<0.005$, t-test). Immobile controls, determining tracking precision threshold, revealed ~20 fold lower diffusion coefficient than measured from live vesicles.

Interestingly, despite the fact that visually most of the trajectories could be classified as confined, a majority of MSD plots were better fitted with a free diffusion model (Fig. 4.5c). This does not mean that vesicles classified as freely diffusing can travel laterally

over long distances, but rather that their confinement 'cage' is either too large in relation to the observation time (30 s) or too small for detection, but diffusing freely on its own. Only a small fraction of vesicles (<9% in all experiments) displayed MSD plots corresponding to 'active transport' mechanisms, i.e. movement with constant velocity in a selected direction. Immobile controls did not display lateral 'caged' diffusion (expected for physically stable point) but rather 'free diffusion' MSD plots. This is probably an artifact due to the limited precision of the tracking algorithm or lateral image drift. Physically, fixed vesicles or beads did not move at detectable scale but the tracking noise led to slowly increasing MSD with essentially zero cage size. Diffusion coefficient for inanimate controls was $\sim 8 \cdot 10^{-6}$ $\mu m^2/s$.

Diffusion coefficients measured from live cells (0.5-2 $\mu m^2/s$) are at least 20 times larger than those measured from immobile controls, which indicates sufficient precision of vesicle tracking. A small portion of beads and fixed vesicles showed 'active transport' MSDs due to the small lateral shift or drift of the sample during imaging.

Average values of MSD fitting parameters for a group of 'caged' MSD plots are shown in Fig. 4.5d-f. The cage radius is smaller for WT cells, probably due to the fact that WT data set contains vesicles measured on a new TIRFM setup (3.1.1) with lower image noise level and thus better tracking precision. Other control data sets measured with two different setups showed consistently ~10 nm smaller xy-cage radii when vesicles were tracked at the new setup. Cage radius as well as diffusion coefficient inside the cage are parameters which directly depend on vesicle jittering and thus critically on tracking precision.

There was no significant difference detected between cage diffusion coefficients in WT, M18 KO and Rescue cells (Fig. 4.5f). However, there is a decrease in the free diffusion coefficient for vesicles in M18 KO cells compared to WT. This can be reversed by Munc18-1 overexpression in null mutant cells, indicating that Munc18-1 function influences lateral mobility of vesicles beneath the membrane.

4.2.2 Characterization of vertical (z) vesicle movement with MSD

In analogy to the xy plane movement characterization in the previous sub-section (xy coordinates were determined with the 2D-Gausiian fitting to the vesicle intensity distribution), vesicle trajectories along z axis in WT, M18 KO and Rescue cells were also subjected to MSD plot analysis (z coordinates were determined from the time course of fluorescence intensity as described in 2.2.1). A summary of MSD fitting parameters determined for all experiments performed is given in Supplementary Table S.3.

Exemplar MSD traces from two different vesicles tracked in control cells, which were classified as 'caged' or 'free' according to our diffusion model, are shown in Fig. 4.6a,b. The absolute MSD amplitudes are up to two orders of magnitude lower for z movement than for xy (Fig. 4.5). This may be due to higher resolution of z tracking with

the sharply decaying evanescent wave, but may also be influenced by a biophysical peculiarity of the intracellular environment: the plasma membrane, its associated protein complexes and the cortical cytoskeleton might form layers that produce different conditions for movement in axial direction than for movement in the plane of the membrane.

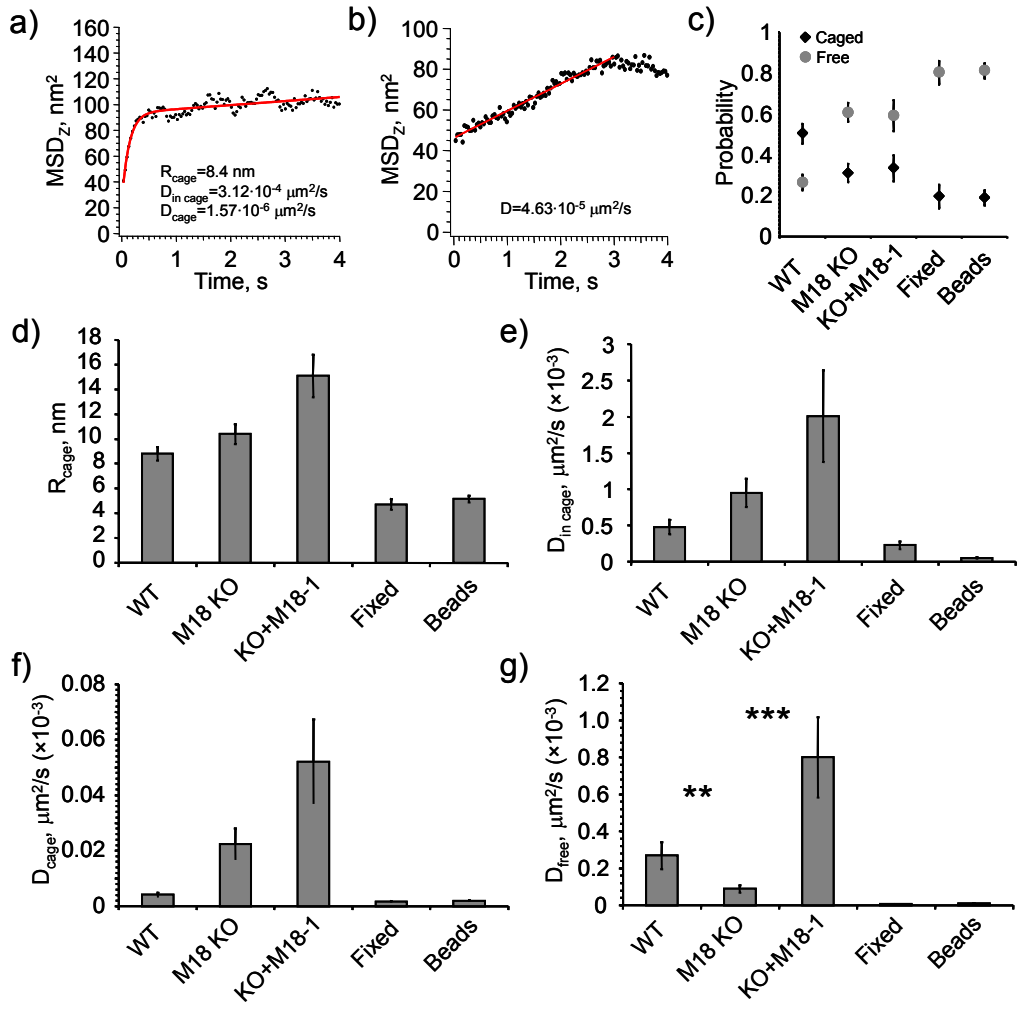

Fig. 4.6. Mean square displacement analysis summary for vesicle axial diffusion in M18 KO chromaffin cells. (**a,b**) Exemplar MSD plots measured from two vesicles, classified respectively as 'caged' and 'free' diffusion scenario. WT but not KO or rescue vesicles displayed 'caged' diffusion MSD as shown by cell-wise average probability to meet different MSD shapes. (**c**). Average confinement cage radius (**d**) is only twice larger than caged diffusion tracking precision determined with immobile controls. Diffusion coefficient of vesicle inside the cage (**e**) and diffusion coefficient of the cage itself (**f**) are low in absolute values and comparable to immobile controls, thus conclusions on differences between phenotypes are problematic. (**g**) Free diffusion coefficient of the vesicles is decreased in M18 KO cells compared to WT and Rescue cells ($p<0.005$ and 0.001, t-test), as for lateral diffusion.

The apparent cage sizes for axial caged diffusion are thus 4-5 times smaller than for lateral diffusion. Estimated diffusion coefficients for caged and free diffusion are also one to two orders of magnitude smaller than corresponding values in lateral diffusion. However, most of vesicles in KO or Rescue but not WT cells displayed 'free' diffusion characteristics in axial direction (Fig. 4.6c), as they did in the lateral direction. Immobile controls predominantly display MSD plot shapes corresponding to 'free' diffusion. As in the case of lateral movement, it can be explained by tracking noise. Z-tracking relies on measurements of fluorescence intensity (see 2.2.1), which is a source for several types of noise of optical and mechanical origin. As a result, the noise produces an effect of apparent slow free diffusion even for immobile controls. The estimation of 'caged' diffusion parameters shows that immobile controls reveal similar cage sizes (only two-fold lower than live objects, Fig. 4.6d). Also, the smallest measured vesicle diffusion coefficients inside the cage and of the cage itself are not much larger than artificial coefficients of immobile controls. This makes any biological interpretation of differences in 'caged' diffusion between phenotypes questionable. In contrast, the apparent free diffusion coefficient for immobile controls is ~10 times smaller than the smallest diffusion coefficient measured for live vesicles. Thus the difference in 'free' diffusion coefficient between WT, Rescue and M18 KO vesicles can be trusted (Fig. 4.6g). The difference in 'free' diffusion coefficient shown here for axial movement is in line with results obtained from MSD analysis in xy plane. The results demonstrate that the absence of Munc18-1 function appears to reduce the vesicle diffusion speed beneath the membrane, which can be rescued by Munc18-1 overexpression.

4.2.3 Velocity autocorrelation analysis of vesicle vertical movement

Despite theoretically strongly enhanced resolution in axial direction, tracking fluorescent objects with evanescent wave microscopy is still subject to errors induced by different noise sources associated with fluorescent measurements (e.g. Poisson shot noise, camera readout noise etc.). The analysis of 'caged' diffusion presented in the previous sub-section (comparison of cage sizes and diffusion coefficients of immobile controls to vesicles in live cells) show that the noise in measured intensities strongly limits the precision of z-tracking assayed with MSD plots. Therefore, another way of trajectory analysis was applied and used as a major tool in this work – the velocity (or ΔZ-) autocorrelation function, referred to as ΔZ-ACF (see 2.2.3 for theory and details). ΔZ-ACF analysis is also affected by the noise in fluorescence intensity signal, but, in contrast to MSD, it avoids the sampling artifact of the first ΔZ-ACF point (at $\tau = \delta t$, see 2.2.3) making ΔZ-ACF analysis more powerful and sensitive to small alterations in vesicle movement than the MSD approach.

Fig. 4.7a shows results of ΔZ-ACF analysis obtained from tracked NPY-Venus vesicles in live cells or immobile controls (vesicles in fixed cells or coverslip-attached fluorescent beads).

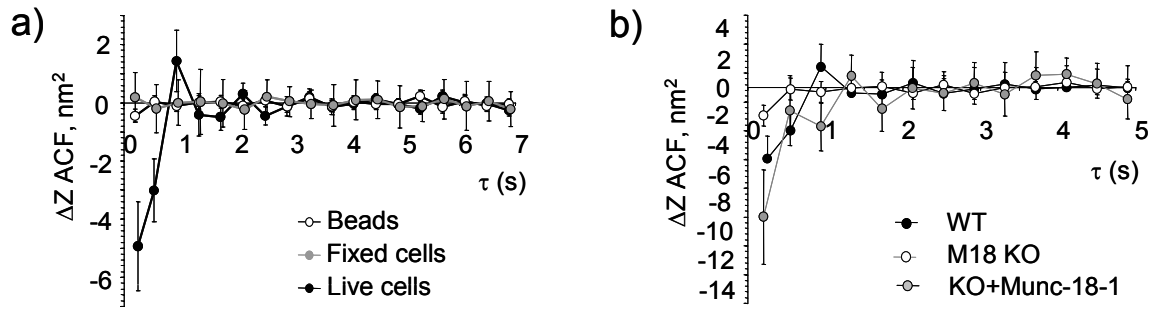

Fig. 4.7. Average ΔZ-autocorrelation functions of NPY-Venus vesicles axial movement in different phenotypes. (**a**) ΔZ-ACF functions measured from live cells (wildtype) and immobile controls: vesicles in fixed cells and fluorescent beads attached to the cover glass. (**b**) ΔZ-ACF functions measured in M18 KO cells versus WT and Rescue cells.

As expected from random (or pseudo-random) diffusion, autocorrelation functions decay to zero with increasing correlation time τ. Remarkably, at correlation time $\tau \leq 0.5$ s, vesicles from live cells have a prominent negative component in ΔZ-ACF. In contrast, the vesicles in fixed cells did not reveal any significant deviation of ΔZ-ACF from zero even at small τ values, as is expected from non-correlated fluctuations of fluorescence intensity. Only the first point of the ΔZ-ACF function from fluorescent beads has a significantly negative value (-0.44±0.22 nm^2). This deviation from zero is probably due to the small fluctuations of fluorescent beads from their positions induced by Brownian motion (beads were not glued to coverslip by any special treatment). When ΔZ-ACFs were compared between M18 KO, WT and Rescue cells (Fig. 4.7b), the negative component at $\tau \leq 1$ s was found to be of the smallest amplitude in M18 KO cells. It was larger in WT and could be rescued by Munc18-1 overexpression in null mutant background.

Differences in negative ΔZ-ACF amplitudes were classified using the NPA parameter introduced in this work (described in detail in sub-section 2.2.3). Fig. 4.8a shows the vesicle ensemble-averaged NPA values obtained for NPY-Venus vesicles in living cells versus immobile controls. NPA values reflect the amplitude of negative ΔZ-ACF component at small correlation time τ, which is significantly smaller in fixed cells (0.01±0.84 nm^2, n=113) or beads (0.40±0.22 nm^2, n=127) compared to control live cells (7.94±1.32 nm^2, n=244). The NPA also shows a significant decrease of the ΔZ-ACF negative component in M18 null mutant cells (2.06±0.75 nm^2, n=137) in comparison to wildtype (7.94±1.32 nm^2, n=244) or KO cells overexpressing Munc18-1 (10.6±2.9 nm^2, n=123) (Fig. 4.8b).

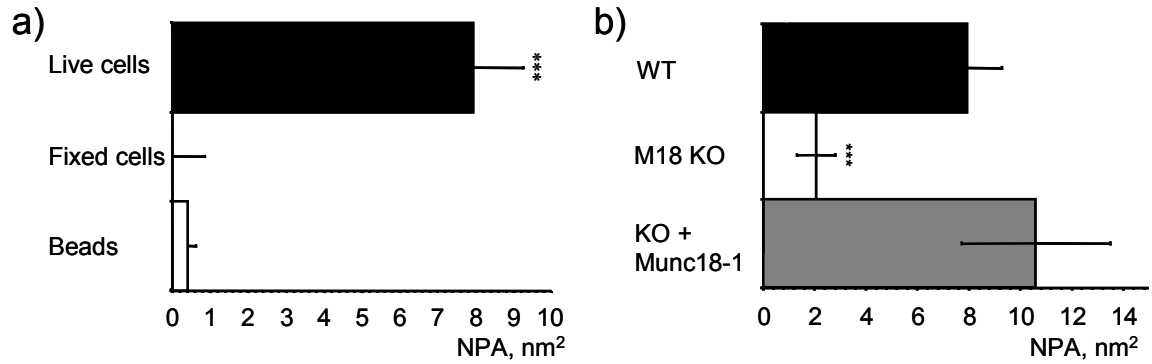

Fig. 4.8. Average NPA values calculated from the ΔZ-autocorrelation function. (**a**) NPA values from vesicles in living cells compared to immobile controls (fixed cells and fluorescent beads). (**b**) NPA values measured in M18 null mutant cells compared to the NPA from WT and Rescue cells. (*** indicates p<0.001 significance level, Wilcoxon test).

These data suggest that ΔZ-ACF and thus the NPA may be useful parameters to characterize differences in the properties of vesicle movement beneath the plasma membrane. Immobile controls demonstrate sufficient resolution of the analysis for detection of subtle differences in vesicle restricted movement. However, the interpretation of differences in the NPA between different phenotypes, and their correlation with biological mechanisms are not entirely straightforward. From Fig. 4.8 one might conclude that vesicles in M18 KO cells tend to be more immobile in the proximity of the plasma membrane than in WT, which, at least intuitively, seems to clash with the vesicle distributions measured with EM. The aim of the next section is to introduce and characterize possible mechanisms that may underlie these differences.

4.3 Computer simulations of vesicle diffusion with different models of movement restriction

4.3.1 The effect of diffusional space restriction with a rigid cage

Simulations of diffusional movement were performed as described in section 2.3. In this sub-section, a reflective wall was introduced at different heights H parallel to the plane of the coverslip (see Fig. 2.12a). A diffusing fluorescent object hence was enclosed inside the spatial cage $0 < Z < H$, because it bounced back after every collision from the coverslip or the wall during random walk diffusion. As expected, this constraint resulted in deflection of the MSD plots from the straight line ('free' diffusion) and formation of the saturation plateau, indicative of 'caged' diffusion (Fig. 4.9a). The saturation level of the MSD plots corresponds to the effective cage radius (approximately $H/2$). A simulated 'immobile control' (an object fixed at the coverslip plane Z=0 and generating Poisson noise with the average intensity 100 a.u.) revealed a flat MSD with a small (50 nm^2) vertical offset due to noise. When the cage size was kept constant (H=150 nm) but the diffusion coefficient was variable (Fig. 4.9b), it became apparent that the speed of

MSD plot saturation strongly depends on the diffusion coefficient, i.e. on the average speed of the diffusing object reaching the opposite walls of the cage. These results also confirmed that the algorithm employed for simulations (section 2.3) functioned correctly.

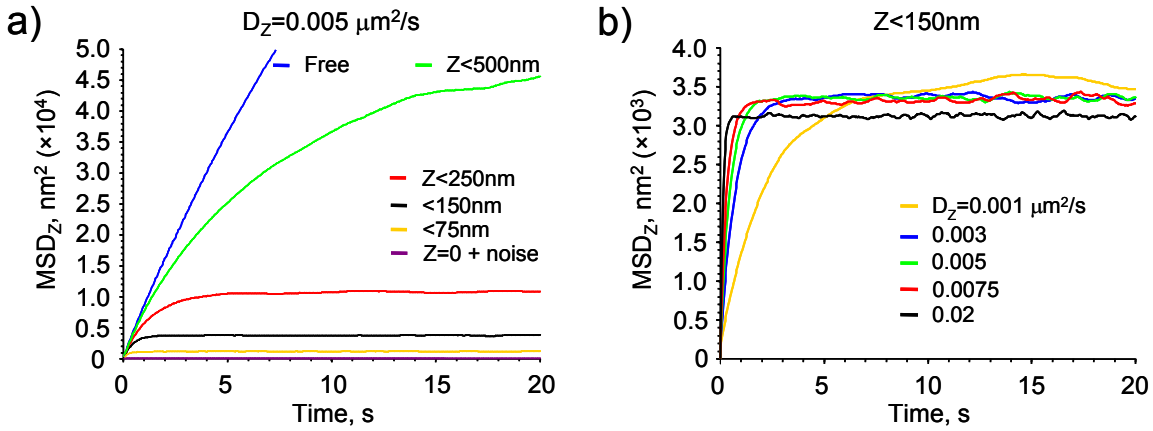

Fig. 4.9. MSD plots calculated from the Z-trajectories, obtained using random-walk diffusion simulations in restricted space. (**a**) A restrictive wall enclosing the object in the space $0 < Z < H$ led to MSD saturation at the level corresponding to the cage size H. 'Immobile control' (Z=0, only Poisson noise) revealed a flat MSD. Z-diffusion coefficient assumed was 0.005 μm²/s. (**b**) The Z-diffusion coefficient was varied while the cage size kept constant: H=150 nm. MSD plots plateau faster (larger D_Z) or slower (smaller D_Z) to the same level.

Next, the velocity autocorrelation functions (ΔZ-ACF) were examined, that result from the simulated trajectories with diffusional space restrictions. The data shown in Fig. 4.10 demonstrate the effect of diffusional space constriction on the ΔZ-ACF. The 'immobile control' (Poisson noise only) resulted in an autocorrelation function not differing significantly from zero (Fig. 4.10a), as in the TIRFM experiments with immobile controls described in the previous section. When the object was allowed to diffuse by increasing the height H of reflective cage from zero, the negative amplitude of ΔZ-ACF also increased. This increase was due to the more prominent signal component arising from repetitive collisions with the walls compared to the random noise from random walk and fluorescence intensity. Additionally, the negative component's decay time to zero became longer with increasing H. The latter is explained by longer time required for the object to reach the opposite wall of the cage after collision. However, further increase in H, along with slowing ΔZ-ACF decay time course, leads in turn to a decrease of the ΔZ-ACF negative amplitude and elevation of the variance (error bars are ±SEM). This decrease is caused by the fact that at large H the object can travel far from the coverslip plane, and changes in the direction of its movement direction are determined more by the random walk probability than by reflections from the restricting wall. Interestingly, when the object is set free in the simulated semi-space ($H = \infty$), the negative component can still be detected only if no additional intensity noise is added in the simulations (or if the number of averaged traces is increased). This small negative component results from the

restriction of the space only by the coverslip, since random walk diffusion loses its symmetry and randomness due to possible reflections of the object from the coverslip plane. The described behavior of the ΔZ-ACF is illustrated by the NPA value (Fig. 4.10b): it is essentially zero for Poisson noise (fixed object) and increases with the object freedom until random changes in movement direction become prevalent over the reflections from restrictive walls at a given diffusion coefficient. An object in a semi-free space is found to have an NPA value different from zero, but the significance of this difference may be compromised by random noise.

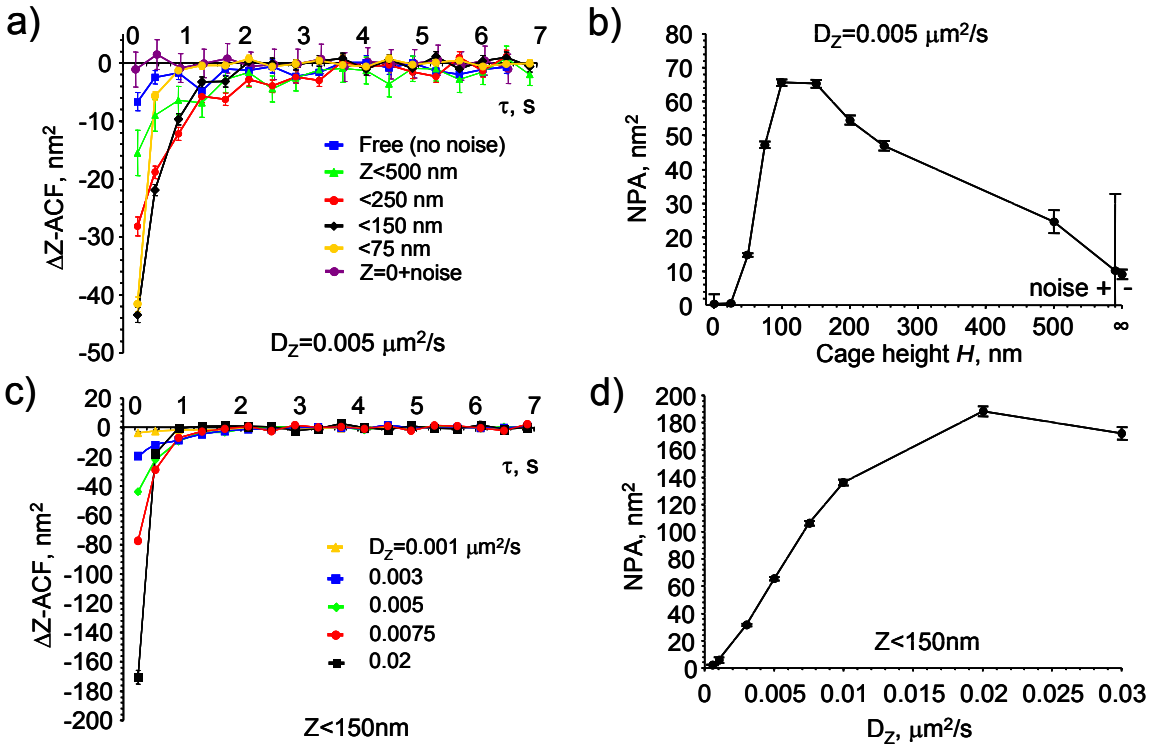

Fig. 4.10. Summary of the ΔZ-ACF analysis of the simulated diffusion trajectories in restricted space. (**a**) Average ΔZ-ACF functions obtained for diffusion coefficient D_Z=0.005 in a space with the restrictive wall at $Z = H$. Fluorescence noise was added in all cases except $Z < \infty$ (which otherwise resulted in a very noisy function). (**b**) Quantification of ΔZ-ACF negative amplitude by the NPA value reveals maximum at intermediate H values (100-200 nm) and small amplitudes for either strongly restricted or free objects. (**c**) Average ΔZ-ACF functions obtained for different diffusion coefficients in the space restricted at H=150 nm. The negative amplitude component, quantified in (**d**) with the NPA, increases within the range of diffusion coefficients assumed in simulations.

Similar effects are produced by varying the diffusion coefficient for the object in the cage with fixed size. Fig. 4.10c illustrates the increase in ΔZ-ACF negative amplitude and acceleration of the autocorrelation decay when D_Z increases, due to shortening time intervals between collisions of the object with the walls. The NPA (Fig. 4.10d) reports the rise in the negative ΔZ-ACF amplitude in the range of tested diffusion coefficients.

Faster diffusion coefficients could not be probed for the spatial grid size used, but the tendency of decay in NPA could be noticed already at D_Z=0.03 μm^2/s. One can predict further amplitude decay with increasing D_Z, since it is equivalent to reducing the cage size while keeping the diffusion coefficient unchanged (shoulder at small H <150 nm in Fig. 4.10b).

4.3.2 The elastic tethering forces

Different kinds of restrictions can be applied to diffusion. In this sub-section, an elastic tethering structure ('rubber band') was assumed to be connecting the object to the coverslip. The space restriction is thus not due to the strictly reflective cage borders, but due to a restoring force that increases in amplitude in accordance to the Hooke's law (see section 2.3) when the object diffuses away from the plane of coverslip. Results from this simulation are shown in the following. The 'rubber band' models were used with fixed free band length L_0=20 nm and differing spring constants $K = F_0/(L_{max} - L_0)$.

Fig 4.11a shows ΔZ-ACF curves for different spring constants. As in the case of restriction with reflective walls, increase in K, corresponding to a strengthening of the tethering, resulted in the transition from the slow decaying autocorrelation functions with small negative amplitude (green) to fast decaying ΔZ-ACF (blue, black). NPA quantification of the negative autocorrelation amplitude (Fig. 4.11b) shows the dependency of ΔZ-ACF on the tether strength in more detail.

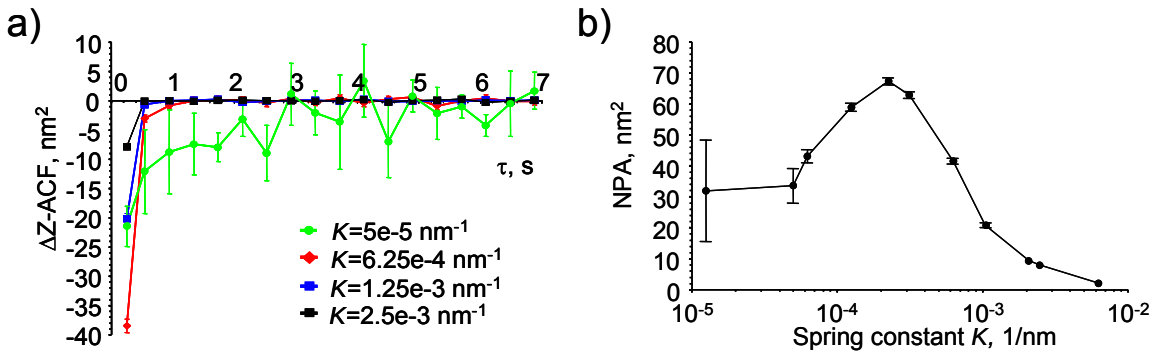

Fig. 4.11. Summary of ΔZ-ACF simulations for a 'rubber band' elastic tethering model. (**a**) ΔZ-ACF results for elastic tethers of the same free length (20 nm) but different spring constants K. Increasing K leads to acceleration of the autocorrelation decay and an initial increase in the negative amplitude (green vs. red) followed by a decrease (red vs blue and black). (**b**) NPA shows the transition of ΔZ-ACF negative amplitudes from small to large values (70 nm^2) at intermediate spring strength (K ~5e-4 nm^{-1}) and the decay to small values upon further increase in K due to the stronger space restriction.

At small K values, the average NPA is low and has a large error (NPA$_{K=1.3e-5}$=31.9±16.4 nm^2), similar to free space or large H in case of restrictive walls. The NPA then increases (up to 67.3±1.2 nm^2 at K=2.25e-4 nm^{-1}), when the spring becomes more rigid

due to the noticeable influence on the diffusing object: it is forced to reverse its direction upon traveling over large distances from the coverslip. When the tether is strong, the forces significantly modify the random walk movement already at small distances, equivalent to the smaller effective cage sizes. It results in the decrease of NPA (and acceleration of ΔZ-ACF decay) because at a given diffusion coefficient (D_Z=0.005 μm^2/s), the object needs less time to cross the cage. These results are very similar to the space restriction with reflective walls. The NPA turns out to be a function of the cage size H and/or elastic tether strength. In both cases, this relationship has a characteristic shape, with a maximum NPA for intermediate space restriction (at the given diffusion coefficient), and small values resulting from either free (loosely restricted) or strongly bound object movement.

4.3.3 The effect of stochastic tethering forces on free diffusion restriction

When a reflective cage or elastic band is introduced to restrict the free object diffusion, the negative component of ΔZ-ACF is determined by the cage size or elastic band parameters and diffusion coefficient, i.e. by the average time needed to cross the cage or stretch the elastic band. In the simulations described here, a stochastic force was implemented which influenced the probability of random walk dislocations at every computed time step (see section 2.3). A set of stochastic 'tethers' with specific first-order activation/deactivation kinetic constants (k_{on}, k_{off}) were introduced in a semi-free space limited only by the coverslip plane at Z=0. Fig. 4.12a shows ΔZ-ACF obtained from the object in which free diffusion (D_Z=0.005 μm^2/s) was influenced by the ensemble of N_{total}=4 tethers with the same strength factor ς=0.25 but different kinetics. It is apparent that the random tethers are able to evoke the effect of restricted space as well as deterministic models (walls or 'rubber band'). The amplitude of the negative component and the decay of the autocorrelation function both depend on the kinetic tether parameters. For convenience, different display colors were assigned to different kinetics of the tethers. The kinetic constants, theoretically expected average lifetimes, and steady-state activation values are listed in the Supplementary Table S.4. The ΔZ-ACF curve shown in red (Fig. 4.12a) corresponds to the tether with fast activation/deactivation kinetics (k_{on}=50 s^{-1}, k_{off}=100 s^{-1}). The negative autocorrelation amplitude is small with negligible error and decays quickly to zero. It corresponds to the strong spatial restriction of the object diffusion like in the case of very small H or rigid elastic band (confirmed also with MSD plots, see Supplementary Figure S.1a). According to the ΔZ-ACF shape of larger amplitude and slower decay, the blue curve corresponds to a weaker tether. This is due to the slower activation kinetics of the blue tether (k_{on}=5 s^{-1}, k_{off}=10 s^{-1}) compared to the constants of the red tether. Similarly, kinetics of the black tether are 10 times slower than of the blue tether, which results in weakening of the effective restrictive force. Interestingly, the steady-state activation rate (the time-averaged ratio n_{active}/N_{total} in the ensemble) is the same in these three cases: $k_{on}/(k_{on}+k_{off})$=1/3. The difference lies

in the duration of the active (as well as inactive) state of the tethers (for an example of tether ensemble activity see Supplementary Figure S.1b-d). The faster the tether fluctuation between its states, the stronger its effect on the effective space restriction.

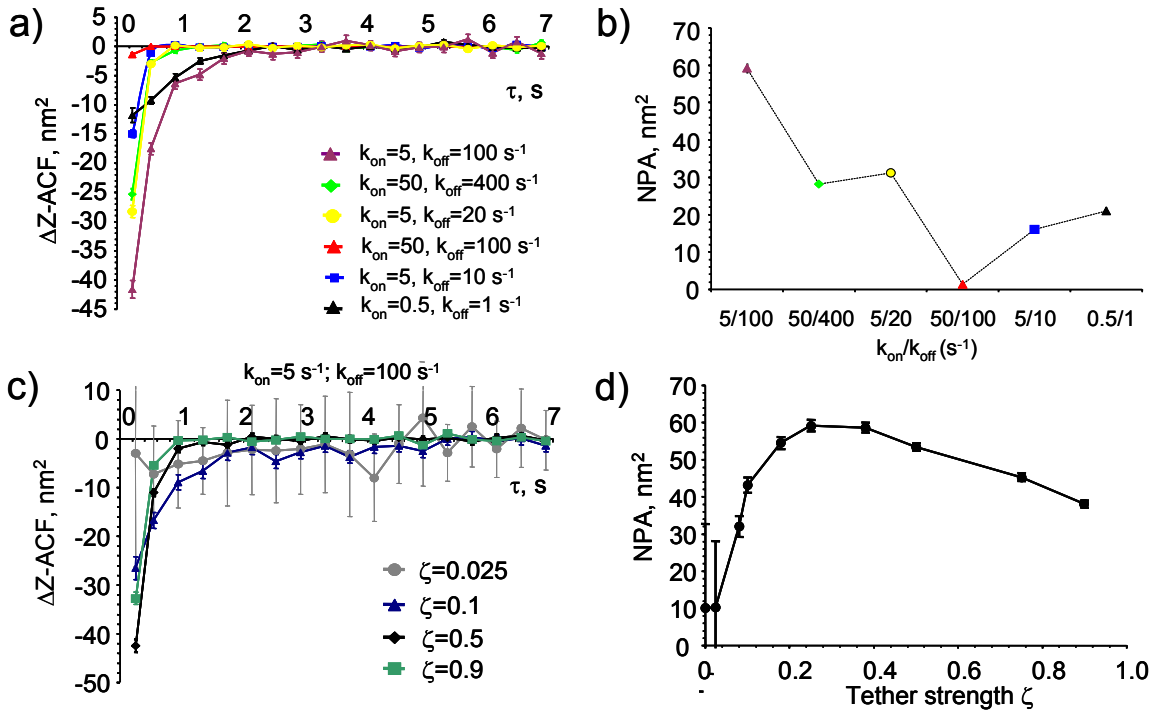

Fig. 4.12. Summary of ΔZ -ACF analysis of diffusion in semi-free space with stochastic tethers. (**a**) ΔZ -ACF obtained from the four-tether ensembles differing only in their kinetic constants k_{on}, k_{off}. The tether kinetic parameters and their correspondence to different display colors are listed in the Suppl. Table S.4. (**b**) NPA quantification of the autocorrelation negative amplitude shows a dependence of effective space restriction on kinetics of the force-producing tethers. (**c**) ΔZ -ACF from the ensemble of four tethers of the same kinetics but various strength factor ς: transition from nearly-free diffusion (small ς) to restriction (large ς). (**d**) NPA reports the dependence of negative ΔZ -ACF amplitudes on the strength factor with a maximum at intermediate ς values. Small or large ς are the limits of free or maximally restricted diffusional space by a given tether.

This relation should also depend on the diffusion speed of a free object (D_Z) because the probability of translocation to a position with a different coordinate at every time step will be more often affected by a faster activating tether then by a slow one. In case of slower tether kinetics and a comparably large diffusion coefficient, the object will be able to cover larger distances by free diffusion while the tether is inactive, than in the case of faster tether with shorter lifetime of the inactive state. On the other hand, the yellow and green tether models resulted in a comparable ΔZ -ACF shape even though these tethers had ~ two-fold different steady-state activation levels. A lower equilibrium level of the active state population for the green tether was compensated by its faster kinetics. Among the tested models, the purple curve corresponded to the weakest effect on space restriction (see also Suppl. Fig. S.1a). Quantification of the negative ΔZ -ACF amplitude component

using the NPA (Fig. 4.12b) does not show the simple correlation between the tether strength and the NPA. A tether yielding to a smaller NPA (black) is less effective in space restriction than stronger tethers (yellow or green), but the strongest tether model (red) yields in turn the smallest NPA.

To investigate the role of tether strength on the velocity autocorrelation function and NPA, the same tether kinetics were assumed in simulations (model corresponding to purple color: k_{on}=5 s^{-1}, k_{off}=100 s^{-1}, $N_{total} = 4$), but with various strength factors ς. The resulting series of the ΔZ-ACF are shown in Fig. 4.12c. At ς=0.025, the average ΔZ-ACF is close to zero and has large error bars because this case is close to the limit of diffusion in a semi-free space (Fig. 4.10a-b, noise added), due to the small influence of the tether. Increasing ς results in the appearance of a distinct negative component in the simulated ΔZ-ACF, which first increases in amplitude and decay rate (ς=0.1 vs 0.5). However, even larger strength factors lead to a decrease of the negative amplitude (ς=0.5 vs 0.9). Quantification of the negative amplitude is given by the NPA (Fig. 4.12d). It shows that a small (NPA$_{\zeta=0}$=10 nm^2) negative amplitude corresponds to free object diffusion. The NPA increases until $\varsigma\approx$0.3 (NPA$_{\zeta=0.25}$=59.1±1.3 nm^2) due to the increase in diffusion restriction and thus expression of non-random time correlation in movement. A further increase in the strength factor leads to a smaller NPA again reaching a minimum at the largest value of ς=1.0 (NPA$_{\zeta=0.9}$=38±1 nm^2) due to the stronger restriction. With this particular tether model parameters, ς=1.0 does not correspond to a dramatic space restriction like with a strong tether (red) already at ς=0.25 (Fig. 4.12a). This is because the tether with purple display color, whose model was used for Fig. 4.12c-d, had slower kinetics and smaller steady state activation (Suppl. Table S.4) which effectively resulted in a weaker restriction force.

To summarize the aforementioned results in this section, the diffusional space restriction can be a product of either real mechanical barrier, or of the action of tethering forces, which can vary in their nature. Monotonic restriction of the space available for random walk diffusion does not lead to monotonic behavior of the ΔZ-ACF negative amplitude, characterized by the NPA. The NPA is small in both weakly and strongly restricted space and reaches a maximum (Fig. 4.10b,d, 4.11b, 4.12d), when free diffusion and entraining forces act at a certain optimal time scale.

4.4 Studying the mechanism of LDCV docking by analysis of single vesicle movement

4.4.1 NPA at different distances from the membrane and during stimulation in Munc18-1 KO cells

As demonstrated by simulations in the previous section, the NPA value can be a valuable tool to characterize the differences in axial vesicle movement. In this section this technique was applied to detect differences between NPY-Venus vesicle movement in

different phenotypes of chromaffin cells (as in 4.2.3). The NPA can report on the vesicle movement restriction and its interaction with the environment to characterize different molecular conditions of vesicle docking. However, the NPA value dependence on the tethering efficiency can be described with a bell-shaped curve where small values of the NPA can result from both very weak or strong tethering forces. Therefore, the characterization of docking mechanisms and mechanistic explanation in M18 KO chromaffin cells require additional analysis. It was previously shown (Johns et al., 2001; Li et al., 2004) that the movement of vesicles close to the plasma membrane is more restricted than of those residing deeper inside the cytoplasm.

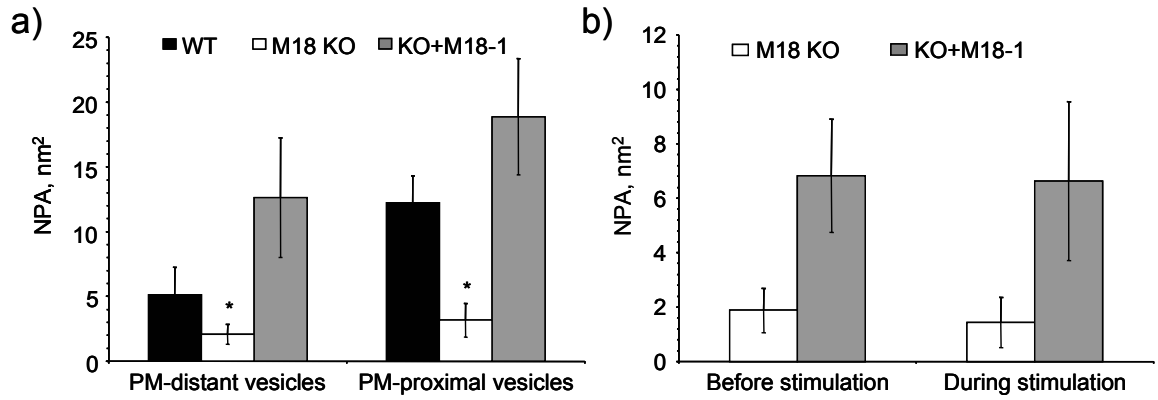

Fig. 4.13. Differences in the NPA for vesicles located at different distances from the plasma membrane and during stimulation. (**a**) The NPA for vesicles in WT, M18 KO and Rescue cells, classified into plasma membrane-distant and proximal groups by their brightness relative to the cytoplasmic NPY-Venus background (I / I_{cyt}): Z ~0-110 nm (proximal); Z ~110-330 nm (distant group). (* indicates $p<0.05$ significant differences between KO and the other phenotypes in each group, Wilcoxon test). (**b**) The NPA measured from the same vesicle population in M18 KO and Rescue cells before and during stimulation with high potassium superfusion.

Thus, vesicles were sorted according to the ratio between time-averaged vesicle brightness I over the average intensity I_{cyt} of the local cytosolic background from cytoplasmic NPY-Venus expression. Under the assumption that the intra-vesicular probe concentration is proportional to the cytoplasmic expression level, this ratio can be used in TIRFM to estimate the vesicle's distance from the plasma membrane. The vesicles were divided into two groups according to their distance from the plasma membrane: a distant group (I / I_{cyt} ranged from 0.1 to 0.6) and a proximal group ($0.6 < I / I_{cyt} < 1.5$). According to the equation for the Z coordinate (2.10), this grouping corresponded to the proximal and the distant adjacent 'layers' of 110 and 220 nm thickness beneath the membrane, respectively. From the vesicle population measured in M18 KO cells (n=137), 78 vesicles were sorted into the distant, and 51 into the proximal group. In contrast, 75/25 (out of n=123) and 129/21 (out of 256) vesicles were sorted into the proximal/distant groups in Rescue and WT cells, respectively. This differential distribution, in addition to the differences in vesicle density at the footprint, supports the notion of a defect in

morphological docking phenotype in the Munc18 null mutant, as also seen in EM (Fig. 4.4).

Fig 4.13a shows the average NPA calculated from the two groups of vesicles in M18 KO, WT and Rescue cells. The data show a slight increase (however not statistically significant) in the average NPA for proximal vesicles compared to the distant vesicle group in all three phenotypes, supporting the finding of stronger restriction at closer distances to the membrane. However, the average NPA remains significantly smaller in M18 KO cells (2.10±0.76 and 3.17±1.31 nm^2 in distant and proximal groups) compared to the WT or Rescue cells. This means firstly that the observed difference in the NPA between phenotypes is neither simply caused by the distinct spatial distribution of vesicles inside the M18 KO cells (where they are randomly scattered beneath the membrane), nor by a possible signal-to-noise problem (the velocity autocorrelation from the dimmer, i.e. more distant vesicles could be dominated by the uncorrelated fluorescence noise). Secondly, these results indicate that the difference in the NPA between phenotypes is intrinsic to the presence or absence of Munc-18, and the NPA thus reports the Munc-18 dependent differences in the properties of vesicle tethering.

The effect of stimulation on the NPA is summarized in Fig. 4.13b. Munc18-1 null mutant or Rescue cells were stimulated with 10 s local application of high-K+ solution (as described in 3.2.2). Those vesicles were selected, whose lifetimes covered both time periods before and during stimulation (n=66 and 50 for M18 KO and Rescue). The graph shows that the average NPA did not change significantly in M18 KO (1.88±0.81 before vs 1.44±0.92 nm^2 during stimulation) as well as in the Rescue cells (6.82±2.09 vs 6.62±2.92 nm^2).

4.4.2 Effect of actin cytoskeleton disruption on the NPA in Munc18-1 KO cells

The tethering forces acting on vesicles and the NPA depend on the local environment in which the diffusing vesicles reside. Any influence of the environment can be due to the interactions with neighboring structures or molecular complexes or due to the restriction of free movement by obstacles with reflective or binding characteristics. One candidate for creating an environment that interacts with the large dense core vesicles is the actin cytomatrix. The actin cytomatrix forms a cortex-like structure beneath the membrane that influences exocytosis in bovine chromaffin cells, reviewed in (Trifaro et al., 2002). In M18 KO embryonic chromaffin cells, the actin cortex is thickened compared to the control cells (shown with phalloidin staining by Bas Konijnenburg, Heidi de Wit, unpublished observation), suggesting a role of actin in vesicle tethering. The first step to address this issue was made in the previous sub-section: stimulation was shown to thin the actin cortex in chromaffin cells (Trifaro et al., 2000). Next, an experiment was performed where actin dynamics were pharmacologically shifted towards G-actin by latrunculin A (LatrA, see 3.2.3). Results from the TIRFM

assay are summarized in Fig. 4.14. In parallel the effect of LatrA was also analysed by electron-microscopy (Heidi de Wit) and electrophysiological characterization of the stimulated secretion (Gulyás-Kovács, 2005).

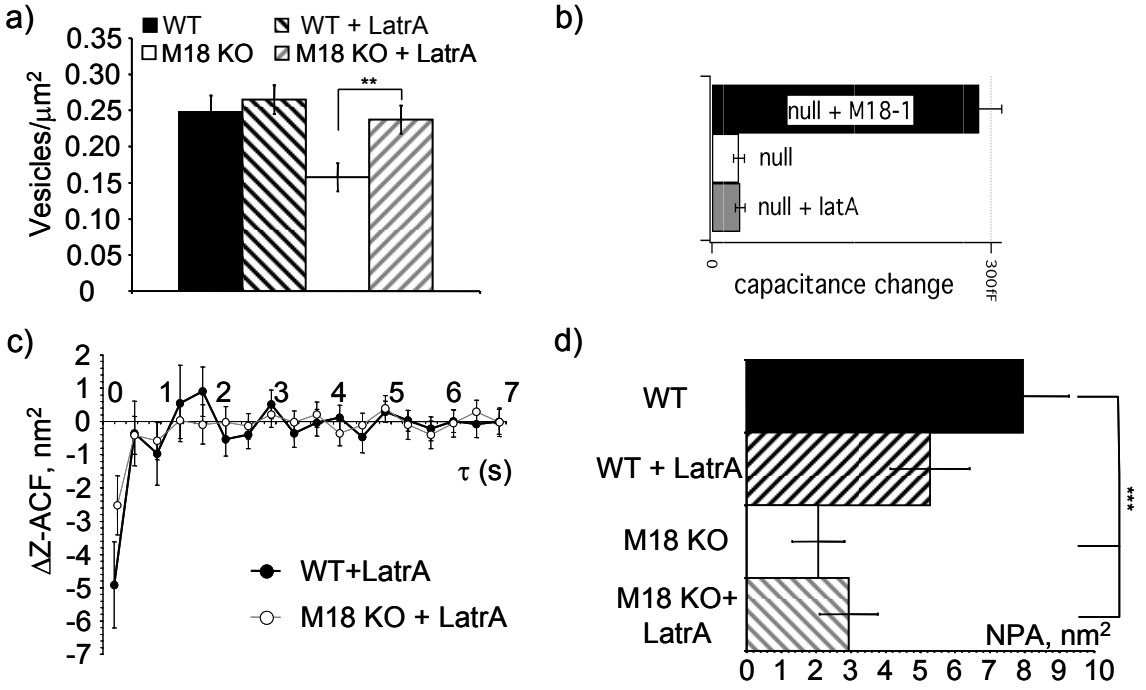

Fig. 4.14. Effect of actin depolymerization in Munc18-1 null mutant cells. (**a**) Actin disruption by the LatrA leads to the rescue of morphological LDCV docking in M18 KO cells, as shown by the density of vesicles per footprint unit area. Vesicle density restoration to the WT level is in agreement with results from electron microscopy (Heidi de Wit). ** indicates $p<0.005$, t-test. (**b**) The cumulative secretion in LatrA treated embryonic M18 KO cells is however not distinguishable from residual secretion in M18 null mutant cells (data from Attila Gulyás-Kovács). (**c**) ΔZ -ACF did not significantly change upon LatrA treatment in M18 KO cells (see Fig. 4.7). (**d**) The average NPA is slightly decreased in WT after actin depolymerization, but did not significantly change in the M18 KO cells despite morphological rescue of the vesicle docking (*** indicates $p<0.001$, Wilcoxon test).

The density of labeled LDCVs at the footprint (Fig. 4.14a) was not changed in the WT cells upon LatrA treatment but was restored back to the wildtype level in M18 KO cells. This is in agreement with the rescue of the drastic LDCV docking defect in M18 KO cells by actin depolymerization, assessed by electron microscopy (Heidi de Wit, unpublished data). Interestingly, the rescue of docking did not lead to the restoration of secretion in M18 KO cells (Fig. 4.14b, data by Attila Gulyas-Kovacs). Also, the WT secretion was not significantly enhanced as assayed by the capacitance measurements, while in bovine chromaffin cells thinning of actin cortex by different treatments increases exocytosis (Zhang et al., 1996; Trifaro et al., 2000; Gulyás-Kovács, 2005). This indicates that the docking rescue is only morphological in LatrA-treated M18 KO cells, and Munc18-1 is

necessary for the functional switch from morphologically docked to functinally primed states.

The movement analysis of single large dense core vesicles upon actin depolymerization revealed a decrease in free XY diffusion coefficients compared to untreated cells (Suppl. Tables S.1), suggesting a role for actin in the lateral vesicle movement beneath the membrane, as reported previously (Steyer and Almers, 1999; Oheim and Stuhmer, 2000; Manneville et al., 2003). However, there was no significant difference found in the axial (Z) diffusion coefficient after LatrA treatment (Suppl. Table S.3). In line with this, the ΔZ -ACF negative component was not significantly changed in the M18 KO cells (Fig. 4.14c vs Fig. 4.7) or in WT cells treated with LatrA. The negative amplitude component quantification (Fig. 4.14d) shows that the actin cortex disruption does not increase the NPA in M18 KO cells (2.93±0.84 nm^2), and it remains significantly smaller than in WT cell. The average NPA was slightly (not significantly) decreased (5.27±1.23 nm^2) by LatrA compared to untreated WT cells.

The results described in this and the previous sub-sections suggest that the NPA correlates with the presence of Munc18-1 and the 'functional' docking of LDCVs, which can develop into the primed state with subsequent fusion. The fact that more vesicles docked morphologically in M18 KO when the actin cytomatrix was dissolved provides an 'internal control'. The vesicles were located as close to the membrane as those in WT, which helped to exclude the possibility of an effect of vesicle distance from the target membrane on the NPA as well as of actin as a physical barrier. This control permits the conclusion that Munc18-1 is a specific factor that determines the properties of vesicle tethering, which can be reported by the NPA. However, it seems likely that Munc18-1 has an additional function in actin cytomatrix regulation or at the stage of LDCV trafficking through the actin cortex towards the plasma membrane.

4.4.3 The effect of phorbol ester on the NPA in Munc18-1 KO cells

The treatment with phorbol ester was shown to depolymerize the sub-membrane actin cytomatrix (Trifaro et al., 2000) by activating a cascade of actin-regulating enzymes. Also, phorbol esters are known activators of protein kinase C (PKC) and Munc-13-1 protein involved in vesicle priming (Ashery et al., 2000; Rhee et al., 2002). Thus, it is interesting to examine the effect of phorbol esters treatment on vesicle docking in M18 KO cells using evanescent wave microscopy (phorbol ester PMA was used in this study, see 3.2.3). Experiments reported in this sub-section were in parallel performed using TIRFM, electrophysiological measurements of secretion (Gulyás-Kovács, 2005), and electron microscopy (Heidi de Wit).

Fig. 4.15 summarizes the results of PMA application experiments performed with TIRFM imaging. PMA induced an increase of the vesicle density at the footprint in both WT and M18 KO cells (Fig. 4.15a). The increase was statistically significant for the M18 KO group and indicated the rescue of docking by PMA in the munc18 null mutant cells.

This result was confirmed by vesicle docking quantification with EM (Heidi de Wit, unpublished data). The observed effect was expected because the effect of PMA on the actin cortex is similar to the effect of LatrA-mediated actin depolymerization.

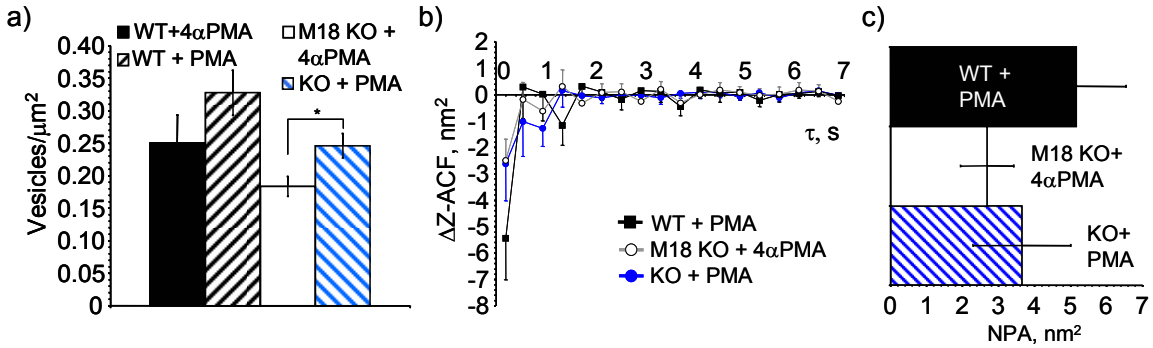

Fig. 4.15. Effect of the M18 KO cells treatment with the phorbol ester PMA. (**a**) The density of vesicles at the footprint revealed an increase in docked vesicle number in both WT and M18 KO (* indicates $p<0.05$, t-test). Significant rescue of vesicle docking in M18 KO by PMA was confirmed with EM (Heidi de Wit). (**b**) The ΔZ-ACF negative component was not significantly changed by PMA in M18 KO cells. (**c**) The NPA quantification revealed no differences between PMA-treated and control M18 KO cells, while the NPA was decreased in WT due to acceleration of ΔZ-ACF decay (see Fig. 4.7).

The rescue of docking, surprisingly, was not only morphological (as in the case of LatrA treatment) but also functional: PMA induced capacitance responses to stimulation by Ca^{2+}-uncaging in M18 KO cells that almost reached the magnitude of control WT responses (Gulyás-Kovács, 2005). The secretion was potentiated in WT control cells by PMA as also reported in (Smith et al., 1998). Single vesicle tracking in PMA treated cells demonstrated that the free XY diffusion coefficient was decreased in WT (Suppl. Table S.2, $p<0.05$, t-test) but did not change significantly in M18 KO cells. The analysis of axial movement (Fig. 4.15b) revealed ΔZ-ACF to be similar in PMA-treated and control (4α-PMA treated) M18 KO cells. The first three points (τ <1 s) had more negative amplitudes in PMA treated cells, but the error bars (SEM) of ΔZ-ACF overlapped. Autocorrelation in WT had at the first point a negative amplitude (-5.45±1.56 nm^2) similar to control cells (see Fig. 4.7) but recovered to zero already at the second point. It resulted in a smaller NPA than in untreated cells (Fig. 4.15c), which might correspond to a stronger vesicle tethering after PMA treatment, thereby leading also to reduced mobility in XY. The NPA in PMA-treated M18 KO cells, despite a slight increase, was not different from the NPA in control cells (3.65±1.35 vs 2.68±0.74 nm^2).

These results suggest that either PMA treatment enables a strong mechanism of vesicle tethering to the plasma membrane even without Munc-18 being present, or that it acts as LatrA by removing the barrier of actin cortex without a change in vesicle tethering. In the latter case, PMA should activate a Munc18-1 and tether-independent bypass, after which the vesicles in M18 KO cells can exocytose upon calcium influx.

4.4.4 Rescue of Munc18-1 null phenotype by expressing a mutated Munc18-1 or another Munc18 isoform

To further on investigate the molecular mechanism of large dense core vesicle docking, the effects of Munc18-1$^{D34N;M38V}$ and Munc18-2 overexpression on the *munc18-1* null genetic background were investigated. The double amino-acid mutation Munc18-1$^{D34N;M38V}$ affects the negatively charged Syntaxin-1a-interacting cavity of Munc18-1 (Naren et al., 1997; Misura et al., 2000). As a result, the binding affinity of mutated Munc18-1 to GST-bound Syntaxin-1a was almost completely abolished (Ruud Toonen, unpublished). EM quantification of the vesicle docking in the M18 KO cells, overexpressing Munc18-1$^{D34N;M38V}$ mutant, showed only partial rescue of vesicle docking compared to the overexpression of the wildtype Munc18-1 (Heidi de Wit, unpublished data). Similarly, the burst component of exocytosis triggered with Ca^{2+}-uncaging was significantly smaller (≈60% of the value measured with wildtype Munc18-1 overexpression) in the cells overexpressing the mutant (Attila Gulyás-Kovács, unpublished data). The second isoform Munc18-2 had a different effect when overexpressed at the null Munc18-1 background: it produced a complete rescue of morphological vesicle docking assayed with EM, but yielded only partial rescue of the secretion burst component (≈30%) with an unchanged sustained component. Moreover, when these two proteins were overexpressed in WT cells, Munc18-2 but not Munc18-1$^{D34N;M38V}$ had a dominant negative effect on secretion by decreasing the size of exocytic burst.

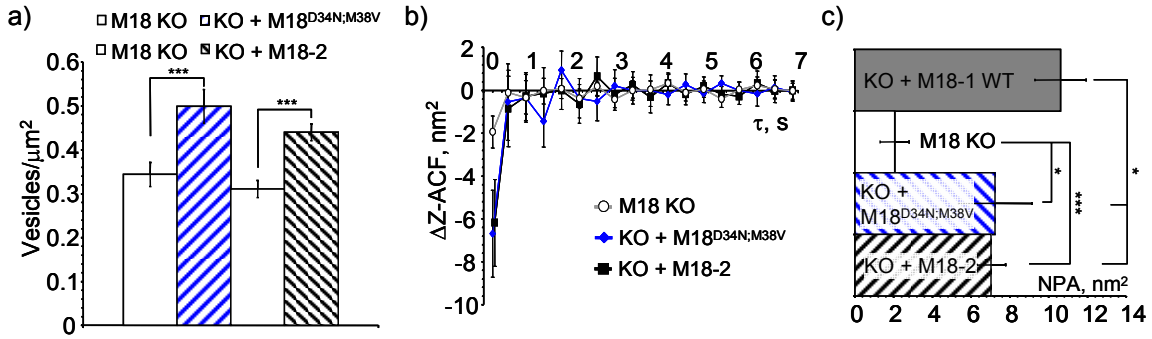

Fig. 4.16. Effect of the Syntaxin-binding deficient mutant Munc18-1$^{D34N;M38V}$ and Munc18-2 on vesicle docking and tethering in M18 KO cells. (**a**) The density of vesicles at the footprint revealed an increase in docked vesicle number in both WT and M18 KO (*** indicates p<0.001, t-test). Significant rescue of vesicle docking by Munc18-2 was confirmed with EM, but the effect of Munc18-1$^{D34N;M38V}$ contradicts the low level of docking rescue, seen with EM. (**b**) Both Munc18-1$^{D34N;M38V}$ and Munc18-2 significantly increased the amplitude of ΔZ -ACF negative component in M18 KO cells. (**c**) The ΔZ -ACF negative amplitude in M18 KO overexpressing Munc18-1$^{D34N;M38V}$ or Munc18-2 is restored. The NPA in these cells was however slightly (but significantly) lower than after wildtype Munc18-1 overexpression (***, * indicate p<0.001, 0.05, Wilcoxon test).

These data from the two parallel approaches made it important to verify the effect of the mutated protein and its isoform on the vesicle tethering using TIRFM. Fig. 4.16 summarizes the Munc18-1$^{D34N;M38V}$ and Munc18-2 overexpression experiments. The vesicle density at the footprint (Fig. 4.16a) was significantly increased after the mutated Munc18-1 or Munc18-2 were overexpressed in M18 KO cells. This increase indicates the rescue or significant increase in number of morphologically docked vesicles which agrees with the EM results for Munc18-2 isoform. However, the Munc18-1$^{D34N;M38V}$ mutant induced a similar increase in the number of docked vesicles. This effect contradicts the EM measurements where the vesicle docking was still perturbed. The contradiction may be due to different expression levels of the Munc18-1$^{D34N;M38V}$ protein in the EM and TIRFM experimental groups. The velocity autocorrelation function ΔZ -ACF (Fig. 4.16b) shows the rescue of the negative component by either Munc18-1$^{D34N;M38V}$ or Munc18-2 overexpression on the null background. ΔZ -ACF shape at small correlation times τ is almost identical between the mutant and the isoform. The NPA quantification (Fig. 4.16c) shows that indeed the negative component was similar in Munc18-1$^{D34N;M38V}$ and Munc18-2 overexpressing cells (7.24±1.91 and 7.03±0.76 nm^2) but significantly larger than in M18 KO cells. The NPA reached the level of WT (see Fig. 4.14d), however, it was somewhat smaller than after wildtype Munc18-1 overexpression (10.6±2.9 nm^2, significance verified with Wilcoxon test).

The data suggest that both Munc18-1 $^{D34N;M38V}$, lacking affinity to Syntaxin-1, and the Munc18-2 are able to rescue the vesicle distribution inside the Munc18-1 null cells by restoring the sub-membrane large dense core vesicle population. Additionally, the vesicle tethering properties were changed by expression of these proteins and approached WT phenotype, as indicated by the ΔZ -ACF analysis.

4.4.5 Probing the role of Synaptobrevin and Syntaxin in LDCV docking

Munc18-1 is a known high-affinity binding partner of the t-SNARE Syntaxin-1a (Hata et al., 1993; Misura et al., 2000), and it was suggested to play the role of a conformational modulator of the Syntaxin before/during the SNARE complex formation (Dulubova et al., 1999; Misura et al., 2000). On the other hand, SNARE complex assembly from both membrane- and vesicle-associated molecular components, is thought to drive vesicle fusion with the plasma membrane. Thus, the SNARE complex formation is one of the candidates to provide tethering forces acting on the vesicle in the vicinity of the plasma membrane. In this sub-section the viral constructs encoding the catalytic light chains of tetanus toxin (TeTx) and clostridium botulinum neurotoxin C1 (BoNT-C) were used to selectively cleave the v-SNAREs Synaptobrevin II, cellubrevin and t-SNARE Syntaxin-1 (Foran et al., 1996; Xu et al., 1998) in wildtype chromaffin cells.

Fig. 4.17 summarizes the effect of TeTx and BoNT-C light chain overexpression on the vesicle docking and tethering. Tetanus toxin (Fig. 4.17a) did not change the number of docked vesicles. This is in agreement with the absence of a docking defect in central

synapses of Synaptobrevin null mutant mice (Deak et al., 2004), Drosophila neuromuscular junction (Broadie et al., 1995) and in chromaffin cells (Borisovska et al., 2005). However, a small (17±3%) decrease in the number of docked vesicles was observed upon BoNT-C expression. Decrease in the number of docked vesicles by botulinum toxin C in chromaffin cells provides evidence against the conclusion that Syntaxin acts downstream of vesicle docking at the neuromuscular synapse (Broadie et al., 1995; O'Connor et al., 1997). However, the mechanism of LDCVs docking in neurosecretory cells might be different from docking of small synaptic vesicles in central or neuromuscular synapses.

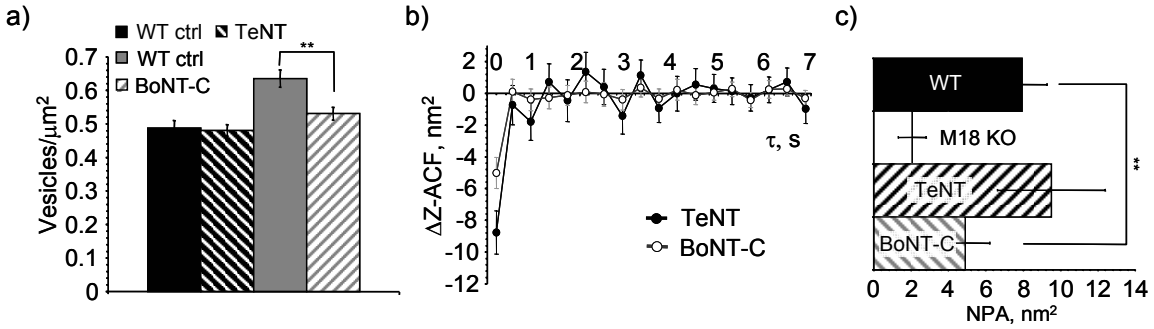

Fig. 4.17. Effect of the TeTx and BoNT-C mediated SNARE cleavage on vesicle tethering in chromaffin cells. (**a**) Density of vesicles at the footprint shows 17% decrease in number of docked vesicles after BoNT-C mediated Syntaxin cleavage, but not after Synaptobrevin cleavage by tetanus toxin (** represents p<0.005, t-test). (**b**) ΔZ -ACF had a decreased negative component after BoNT-C, but not after tetanus toxin light chain overexpression. (**c**) The decrease in ΔZ -ACF negative component resulted in a decrease of the NPA by BoNT-C as compared to the wildtype, but it is still larger (p<0.001) than the NPA value for M18 KO (** indicates p<0.005, Wilcoxon test).

The ΔZ -ACF negative component after TeTx overexpression (Fig. 4.17b) was the same in WT or Rescue cells (Fig. 4.14), but was reduced to only one significantly negative point of smaller amplitude upon BoNT-C expression. The NPA (Fig. 4.17c) thus was not changed by tetanus toxin (9.51±1.30 nm^2), however, it was significantly reduced by BoNT-C (4.90±0.87 nm^2). This reduction though was not as dramatic as the effect of Munc18-1 deletion (p<0.001, Wilcoxon test).

These results suggest that Syntaxin-1a participates in sub-membrane vesicle dynamics and tethering in chromaffin cells, in a similar manner to Munc18-1. Absence of vesicle fusion in synaptic terminals of neurons with genetic deletions of Munc18-1 and Syntaxin (Broadie et al., 1995; Verhage et al., 2000) leads to the hypothesis that Syntaxin, as a Munc18-1 interaction partner, can play a role in LDCV docking in chromaffin cells.

4.4.6 Vesicle docking in SNAP-25A null mutant chromaffin cells

Botulinum toxin C1 was shown to proteolytically cleave not only Syntaxin-1, but also another t-SNARE - SNAP-25A (Foran et al., 1996). In order to separate the possible

effects of Syntaxin and SNAP-25A cleavage on vesicle tethering, the vesicle dynamics in chromaffin cells from SNAP-25A null mutant animals were investigated. The summary of the experiments is shown in the Fig. 4.18.

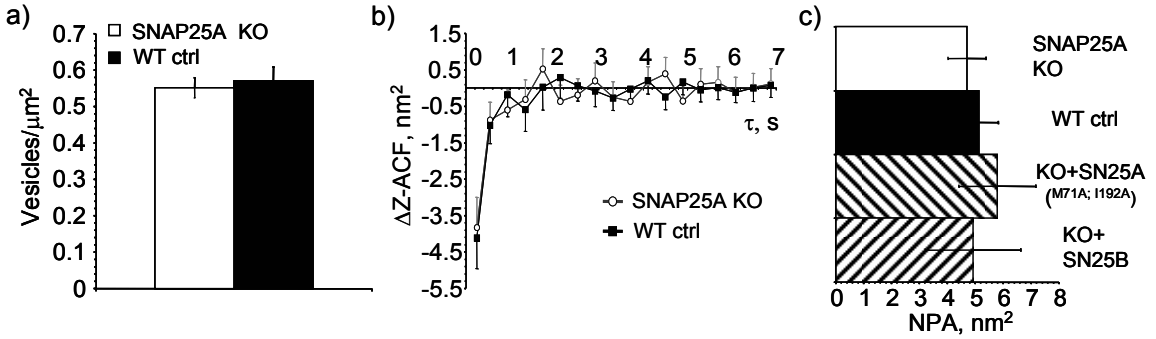

Fig. 4.18. Vesicle docking and tethering in the SNAP-25A null mutant cells. (**a**) SNAP-25A deletion does not change the number of docked vesicles as shown by the density of granules per footprint unit area. (**b**) The shape of ΔZ-ACF is not different between the SNAP-25A KO and control wildtype cells. (**c**) According to the ΔZ-ACF, the NPA quantification shows no difference between vesicle tethering properties in SNAP-25A KO and WT. Overexpression of the SNAP-25A bearing the 5-th layer zipper mutation (M71A; I182A) or the SNAP-25B isoform on the null mutant background did not change the average NPA value.

The density of LDCVs per unit area in SNAP-25 null mutant cells was not significantly different from the control (Fig. 4.18a). The vesicle density was also not changed when SNAP-25B (neuronal isoform of the SNAP-25) or SNAP-25A$^{M71A;I192A}$ (SNARE complex 5-th layer 'zipper' mutation, provided by Dr. Jakob Sorensen) were expressed on the SNAP-25A null genetic background. It confirms the results of the vesicle docking EM analysis performed in the SNAP-25A null mutant cells (Sorensen et al., 2003) which revealed intact morphological vesicle docking. The shape of the ΔZ-ACF is almost identical for SNAP-25A KO and WT control cells (Fig. 4.18b). The NPA reports no differences between the amplitudes of the ΔZ-ACF negative component in the WT, SNAP-25A KO, or when the mutated SNAP-25A or the SNAP-25B isoform were expressed. These data suggest that SNAP-25A is not required for the vesicle docking upstream of the priming/fusion step, for which it was shown to be essential (Sorensen et al., 2003).

4.5 Analysis of the vesicle residency time at the membrane in Munc18-1 null mutant chromaffin cells

4.5.1 Dynamic docking of vesicles in Munc18-1 null mutant chromaffin cells

The data described in the previous sections demonstrate that Munc18-1 is important for vesicle docking to the plasma membrane. According to the results of single vesicle tracking experiments and the ΔZ-ACF analysis, Munc18-1, along with having a function

in the fusion machinery downstream of the morphological contact between the vesicle and the plasma membrane, provides a distinct mechanism of vesicle movement restriction beneath the plasma membrane, or vesicle tethering. Parallel ultrastructural morphological analysis (EM) and TIRFM imaging suggest that the vesicles might in fact be tethered to the plasma membrane. In this case, the vesicles would be expected to have a certain affinity to the membrane. The affinity to the membrane can be due to several subsequent steps or molecular events after the vesicle makes physical contact with the plasma membrane. These steps and thus the affinity might be different in the munc18-1 null mutant cells, which could explain the differences in morphological docking and tethering properties of large dense core vesicles.

The results of the analysis of vesicle residency time at the membrane are described in this section. The vesicle appearance and disappearance events were detected with the automated algorithm described in 2.2.4. The average normalized histograms of residency time, measured from the M18 KO, WT and Rescue chromaffin cells with NPY-Venus labeled vesicles, are summarized in Fig. 4.19. The histograms (Fig. 4.19a) were binned logarithmically after log-transformation of the measured vesicle residency times (see sub-section 2.2.4), normalized to the unity area for each cell and averaged between cells.

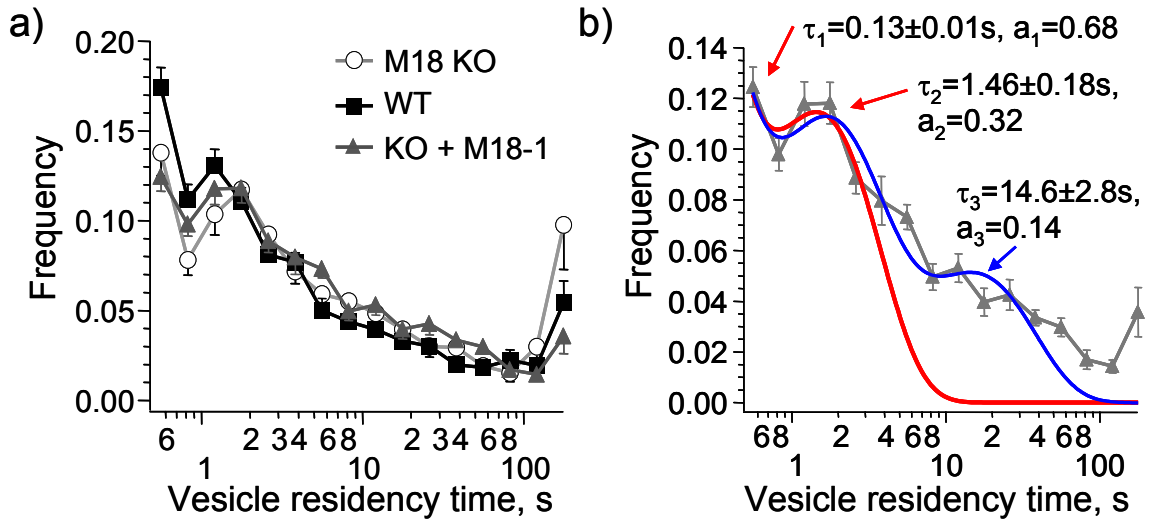

Fig. 4.19. Normalized histogram (frequency) of vesicle residency times. (**a**) Normalized histograms of logarithmically transformed residency times for the total set of detected vesicles in M18 KO, WT and Rescue cells (averaged over multiple cells). Two peaks can be distinguished: at low residency times (≤0.6 s) and between 1 and 2 seconds. The total amount of vesicles binned into the histogram: n=2398 (M18 KO, N=30 cells), n=2997 (WT, N=35 cells), n=3536 (Rescue, N=34 cells). (**b**) Fitting example of the residency time histogram from the Rescue experiments with the two- or three-state model (red and blue respectively). The first two peaks determined the average residency times ~0.13 and ~1.5 s. A three-state model fit provided a good approximation only of the first two peaks but the third peak alone (τ_3 =14.6s, blue arrow) was not sufficient to explain the long tail with a single average-lifetime state.

Displaying the obtained histograms in log-scale is meant to enhance the separation of close maxima around the average residency times in the different docked states. Indeed, there are at least two distinct maxima (corresponding to states with different average residency time): at low residency times close to the sampling interval (0.3 s) and at slightly higher residency time between 1 and 2 seconds. The histograms decay for higher residency times except for the last bin. The last bin contain of the vesicles which were at the membrane practically during the whole observation period of 180 s and thus represent a distinct population of 'static' or very long-lived vesicles. Interestingly, the M18 KO cells reveal a larger average fraction of 'static' vesicle among the total number of detected vesicles (9.77±2.48%), than the WT cells (5.45±1.19%).

The equation (2.19) was used to fit the histograms in order to determine the locations of the histogram maxima. An example of such fitting is shown in Fig. 4.19b, where the histogram from Rescue cells was used as a template. The two- or three-state model functions were used to approximate the first two peaks of the histogram. It was determined that the first peak (extrapolated to the average residency time τ_1=0.13 s) had the largest partial contribution ($a_1 \approx 68\%$), the second (τ_2=1.4 s) had smaller contribution ($a_2 \approx 32\%$). The two-component function decays to zero too fast and can not explain the long-residency time tail of the distribution. The three-state fitting function is able to accommodate the first two peaks as well as the two-state model, but the third peak alone failed to approximate the full length of the distribution tail. This suggested that there were probably more than one state enveloped in the long-residency time part of the distribution tail, that are difficult to distinguish.

The histograms on the Fig. 4.19 were obtained from the whole ensemble of detected vesicles at the footprint, irrespective of the footprint area. The next figure 4.20 shows the averaged histograms after normalizing cell-by-cell to the footprint membrane area and the observation time. Thus, the Fig. 4.20a shows the relationship of vesicle 'hit-rate' (in vesicles/μm^2/min) and residency time at the membrane. The 'hit-rate' distributions, as used here, reflect the appearance frequency of the vesicles of certain residency time at the membrane. The hit-rate curves in M18 KO, WT and Rescue cells had the same characteristic shape as the ensemble histograms (Fig. 4.19): there were two distinct components at the same residency times τ_1, τ_2. However, the amplitude of the hit-rate distribution (Fig. 4.20a), in contrast to the ensemble histogram, reveals a difference between M18 KO, WT and Rescue cells due to the normalization by the footprint area. The amplitude of the first two peaks is smaller in M18 KO than in the WT or Rescue cells. For residency times between the second and the third peaks (τ=5-15s), the magnitudes of hit-rates in M18 KO and WT come close to each other.

Zooming in on a range of residency times from 10 to 120 s (Fig. 4.20b) shows the distribution tail likely containing a mixture of different residency times/docking states which made it difficult to fit with a theoretical model (2.19). The average hit-rate in WT is larger than that in M18 KO, particularly seen in the last bins, while the hit-rate distribution from the Rescue cells is significantly above the KO curve at all residency

times. This result, in principle, could be expected given the vesicle docking defect in M18 KO cells leading to the smaller average vesicle density at the footprint (Fig. 4.3). The hit-rate distribution, however, supplies additional information on vesicle residency time at the membrane. The last bin of the distributions at τ =177 s, containing the 'static' vesicles, was excluded from the Fig. 4.20b, since the static vesicles do not conform to the definition of 'hit-rate' and should be excluded from the analysis because of unknown real residency time (>180 s of observation time). The last bin amplitude in M18 KO was not larger than in the WT (as in the case of ensemble histograms), reflecting the overall lower density of the docked vesicles in M18 KO cells.

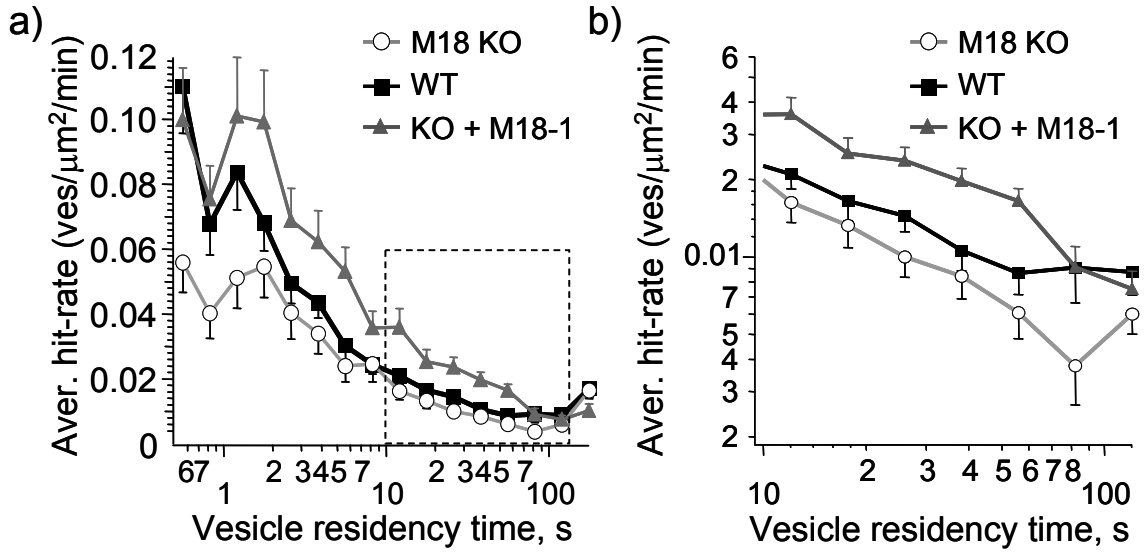

Fig. 4.20. Vesicle hit-rate distributions over vesicle residency times at the cell footprint membrane. (**a**) Average hit-rate distributions obtained from the ensemble histograms after normalization by the footprint membrane area and observation time (the ensemble data sets are as in Fig. 4.19: M18 KO, WT, Rescue cells). (**b**) Zoom-in of tails from the full-length hit–rate distributions shown in (a), for the lifetimes range 10-120s (dotted rectangle).

The hit-rate distributions shown in Fig. 4.20 are effectively weighted with the inverse of the residency time. This is because the short-lived vesicles appear at the membrane more often than the vesicles with longer residency time, which results in a larger cumulative number of 'hits' by shorter-lived vesicles than by longer-lived ones during a finite observation time. In order to obtain a steady-state 'snapshot' distribution of residency times, the average occurrences were obtained by counting the average density of vesicles with certain residency time at single images of the time lapse movie (see 2.2.4). It avoids the bias in the distributions towards short-lived events, and gives the expectation value of vesicle density for different residency times. The results of this analysis are shown in Fig. 4.21.

Fig. 4.21a shows the vesicle density distribution at a random snapshot of the footprint, i.e. the expectation value for vesicle density, depending on the vesicle residency

time. In contrast to the hit-rate distribution, it reveals the increase of vesicle density with residency time. It indicates that most of the vesicles seen on a snapshot footprint image have rather long residency times. In relation to electron microscopy, it means that the morphologically docked pool is dominated by the vesicles with long residency time in all phenotypes: M18 KO, WT or Rescue. The vesicle density for short residency times corresponding to the τ_1 (<1 s) peak is similar between the M18 KO, WT and Rescue. In the range of the second peak in hit-rate distribution (τ_2), the Rescue cells demonstrate a more significant increase in vesicle density in comparison to the M18 KO and WT cells. At larger residency times (τ >10 s) corresponding to the right tail of hit-rate distributions (Fig. 4.20), the vesicle density in the WT and Rescue cells increases significantly above the M18 KO level.

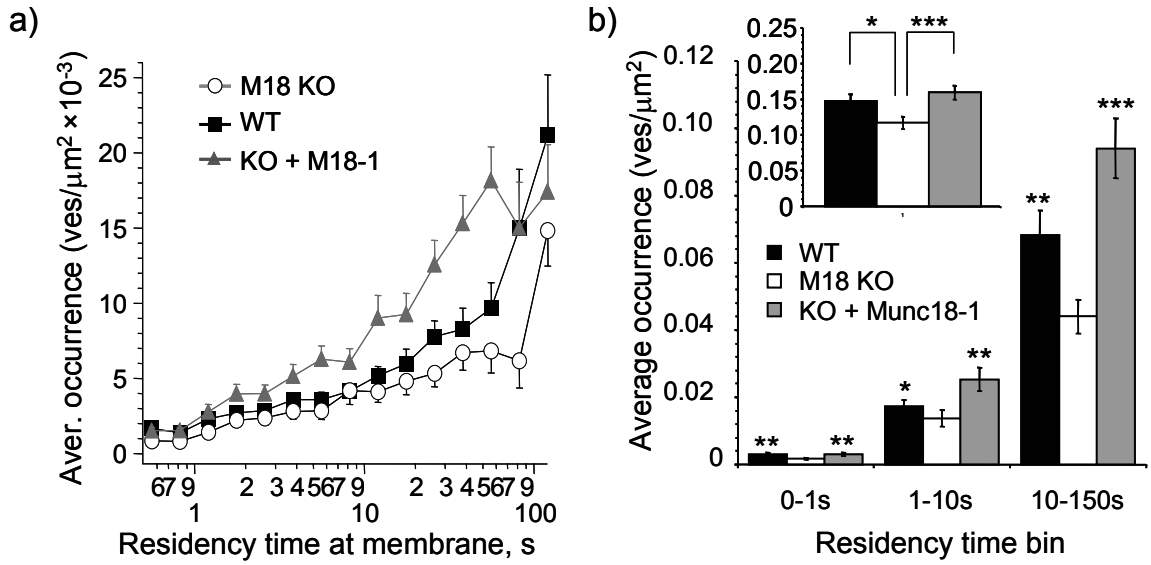

Fig. 4.21. Average occurrence distribution (instantaneous vesicle density) over the residency times. (**a**) Average density of vesicles of certain residency time at a random steady-state snapshot of M18 KO, WT or Rescue cell footprint. (**b**) Vesicle density in the three residency time bins, corresponding to the two first peaks around τ_1 (<1 s), τ_2 (1-10 s), and longer residency times in the tails of the hit-rate distributions (10-150 s). The last bin ($\tau \geq 177$ s) is excluded. The inset shows the vesicle density binned over the whole range of residency times (0-180 s). *, **, *** correspond to the significance levels p<0.05, 0.01, 0.001 respectively, Wilcoxon test. Student's t-test did not detect differences (p=0.24) between WT and M18 KO in the 1-10 s bin.

This trend could be quantified by further binning of the average occurrence distribution (Fig. 4.21b). The binning was performed for residency time ranges according to the first two peaks and the tail in the hit-rate distributions, as discussed above: τ <1 s, 1-10 s, 10-150 s. There was a significant difference between M18 KO, WT and Rescue cells for the vesicles that spent a very short time (<1 s) at the membrane. This difference was less significant between the WT and M18 KO cells (t-test did not find any difference at all, p=0.035 with Wilcoxon test) in the second bin (1-10 s), i.e. for vesicles that were

retained at the plasma membrane for relatively short times. The Rescue cells, however, displayed an increased vesicle density in this time bin compared to the M18 KO cells (p=0.005, Wilcoxon test). In the last bin (10-150 s) of long-lived vesicles, the instantaneous vesicle density was larger in WT and Rescue (p=0.007 and 5e-6, Wilcoxon test) compared to the M18 KO cells. The last points of the hit-rate distributions (τ =177 s, 'static' vesicles) were not included in the analysis in Fig. 4.21a,b for the reason of unknown residency time. Because of the limited observation time window, the last bin contains all the vesicles with residency time τ >180 s.

The overall density of vesicles at the cell footprint, calculated by binning of residency times from zero to the total observation length (180 s), resulted in a significantly smaller value in the M18 KO (Fig. 4.21b, inset), indicative of the impaired large vesicle docking in munc18-1 null mutant cells (Fig. 4.3, 4.4).

These results propose a separation of all the vesicles into at least three categories or 'pools': 'unretained visitors' with very short residency times (τ <1 s); the vesicles that transiently dock for a relatively short time (1-10 s); and vesicles that spend a rather long time at the membrane (10-150 s). The vesicles with the large residency times are those that comprise the morphologically docked pool measured with electron microscopy. The most pronounced difference between the M18 KO, WT and Rescue cells is observed within this pool (residency time bin), which prompts association of this pool with the pool of functionally releasable vesicles that is probed with electrophysiology.

4.5.2 Vesicle residency time distribution in Munc18-1 KO cells overexpressing Munc18-1 mutant or Munc18-2

It was shown previously in this work in section 4.4.4 that the Syntaxin1-binding deficient mutant Munc18-1$^{D34N;M38V}$ or Munc18-2 isoform overexpression led to the rescue of M18 KO phenotype, both in terms of the vesicle density at the footprint, or in terms of negative component of the ΔZ-ACF. In this sub-section, the effect of overexpression of these molecules on the residency time distribution was examined. Figure 4.22 summarizes the experiments and compares the obtained residency time distributions with the ones from M18 KO and Rescue cells (the same cells as in 4.5.1).

Fig. 4.22a shows the average hit rate distributions. As before, after Munc18-1$^{D34N;M38V}$ or Munc18-2 isoform overexpression, there where two apparent peaks around τ_1=0.14 s and τ_2=1.4 s, which were determined in sub-section 4.5.1 to correspond to the 'unretained visitors' and transiently docking vesicles. Both peaks in Munc18-1$^{D34N;M38V}$ or Munc18-2 cells had larger magnitudes than in M18 KO cells, reaching the level of the hit-rate peaks in Rescue cells. Similarly, the longer residency time tails were increased in amplitude compared to the M18 KO in both groups (Fig. 4.22b), reflecting the rescue of vesicle density by these constructs (see 4.4.4).

The average vesicle occurrence distributions (Fig. 4.22c) demonstrate an increase in the instantaneous density of vesicles with longer residency times. Like for the Rescue

cells, the cells overexpressing Munc18-1D34N;M38V or Munc18-2 revealed larger densities for the short residency times (<1 s) and for the range of longer times (1-10 s).

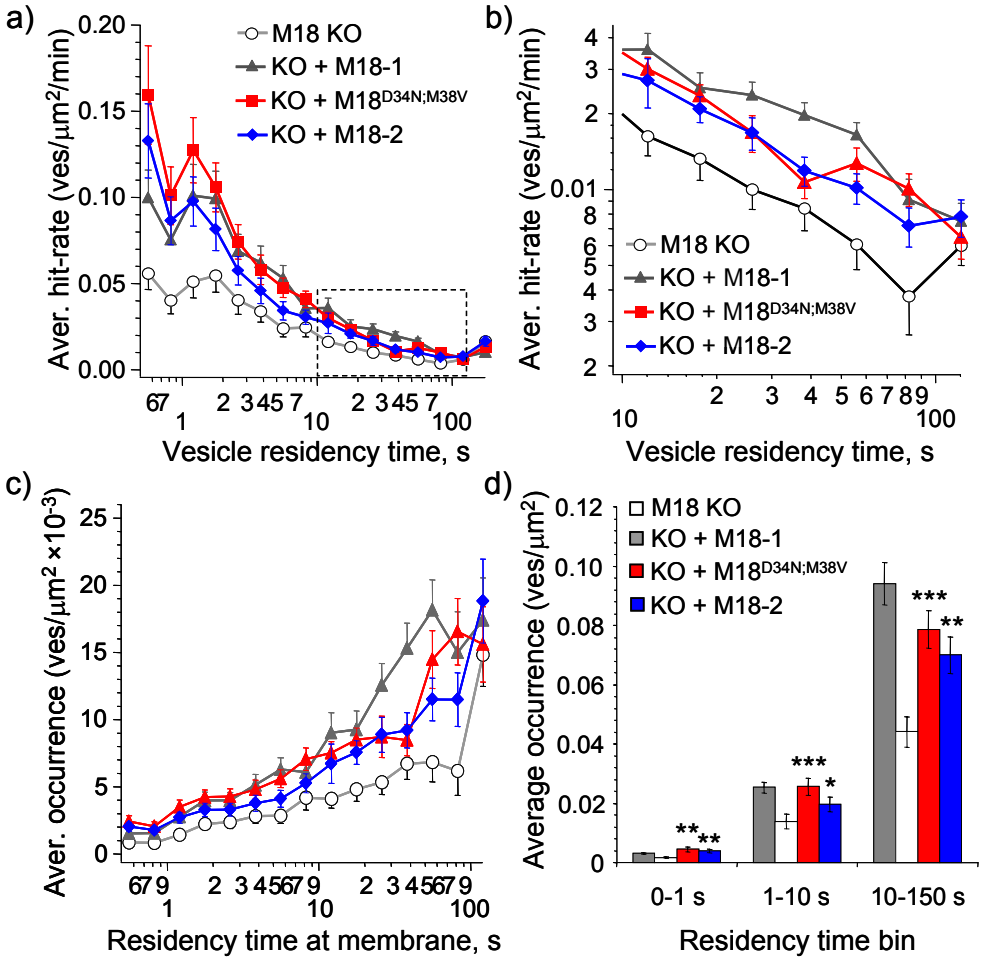

Fig. 4.22. Summary of the residency time analysis in M18 KO cells overexpressing Munc18-1$^{D34N;M38V}$ or Munc18-2. (**a**) Average hit-rate distribution in M18 null cells after overexpression of Munc18-1$^{D34N;M38V}$ mutant (red) or Munc18-2 (blue), compared to M18 KO or Rescue (wildtype Munc18-1 overexpression) cells. The total amount of vesicles binned into the histogram: n=4218 (M18-1$^{D34N;M38V}$, N=36 cells), n=3884 (M18-2, N=33 cells). (**b**) Zooming in on the long residency time tail (10-120 s) of the hit-rate distribution (dotted rectangle in a) shows an increase in hit rate for these vesicles upon Munc18-1$^{D34N;M38V}$ or Munc18-2 overexpression. (**c**) Average occurrence distributions display a density increase similarly to the Rescue cells. (**d**) Vesicle density for the three residency time bins, corresponding to the two first peaks (<1, 1-10 s), and the tail of longer residency times (10-150 s) of the hit-rate distribution: rescue of null mutation by Munc18-1$^{D34N;M38V}$ or Munc18-2. *, **, *** correspond to the significance levels p<0.05, 0.01, 0.001 respectively, Wilcoxon test, comparison was performed with the M18 KO cells.

Also, like in the case of the WT (Fig. 4.21a) and Rescue cells, the density rose to the larger values for τ >10 s than in the M18 KO cells. Quantification using binning of residency times (Fig. 4.22d) shows the same effect after Munc18-1$^{D34N;M38V}$ or Munc18-2

overexpression as in the Rescue cells. There was an increase in all three bins, which corresponded to an overall increase in density of NPY-Venus expressing vesicles at the footprint. In the case of M18-2 overexpression, this effect was less significant in the middle bin (1-10 s) than in the short and long residency time bins, similarly to the WT cells.

To summarize, overexpression of the mutant Munc18-1$^{D34N;M38V}$ and the second protein isoform Munc18-2 resulted in a rescue of the M18 KO residency time distribution (shape and amplitudes) to the level of cells overexpressing wildtype Munc18-1 protein.

Chapter 5

Discussion

Evanescent wave microscopy (or TIRFM) was utilized in this work to delineate the mechanisms of large dense-core vesicle docking to the plasma membrane in chromaffin cells. The cells used in the experiments were of different genetic backgrounds having impaired morphological vesicle docking and/or calcium dependent secretion, in order to dissect the players in the cascade of molecular interactions leading to docking and subsequent Ca^{2+}-dependent fusion with the plasma membrane. Thus, the apparent docking states and mechanical characteristics of vesicle movement beneath the plasma membrane were studied in the cells with altered molecular composition of the exocytic machinery, and used as read-out for the properties of vesicle docking/tethering mechanisms.

Electron microscopy and electrophysiological secretion assays were performed in parallel by Drs. Heidi de Wit and Attila Gulyás-Kovács, as parts of a collaboration. In the discussion I will reference their data for argumentation of the conclusions.

5.1 Technical approaches and biophysical background of the analysis of vesicle docking mechanisms

5.1.1 Important choice: fluorescent probe for vesicles

Tracking of single vesicles using TIRFM requires selection of a proper fluorescent marker. Firstly, the fluorophore chosen to label vesicle cargo molecules should have a large fluorescence yield at low pH 5.5 of vesicular lumen. This requirement makes the fast maturing YFP variant called Venus (Nagai et al., 2002) a suitable candidate to be a fluorescent reporter of the cargo marker. Secondly, specificity of fluorophore targeting is required. The sorting signal sequence of neuropeptide Y, a native cargo of chromaffin granules (Hexum et al., 1987), determines the specificity of NPY-Venus fusion construct targeting into the large dense-core secretory vesicles (Lang et al., 1997; El Meskini et al., 2001). The NPY-Venus construct labels the vesicular structures when expressed in the chromaffin cells (Fig. 4.1). NPY-based fluorescent vesicle markers were used in several studies describing vesicle dynamics and exocytosis in different cellular systems (Perrais et al., 2004; Schutz et al., 2005; Tsuboi et al., 2005). Specific targeting of NPY to the LDCVs is advantageous because other non-peptidergic markers like FM dyes, acridine orange or Lysotracker probes are much less selective and label virtually all recycling (for FM dyes) or acidic membranous compartments making true vesicles indistinguishable from other structures using imaging approach.

However, the correspondence of the NPY-Venus labeled vesicles to the functional exocytic vesicle pool has to be established more carefully. One line of evidence that NPY-Venus vesicles are indeed functional fusion-competent LDCVs comes from the

estimation of fusion probability for NPY-Venus vesicles upon stimulation (summarized in Table 4.1). There was a direct correlation found between the frequency of NPY-Venus vesicle fusion and the amplitude of the fast exocytic component in the cells of different genotypes with altered content of Munc18-1 (electrophysiological data from (Gulyás-Kovács, 2005) which suggested that NPY-Venus vesicles belong to the fusion-ready population of vesicles. The low absolute numbers of NPY-Venus vesicle fusion events are most likely caused by underestimation of fusion rate due to: a) counting only the events that were followed by the lateral fluorescence spread and neglecting fusions with transient pore openings (Taraska and Almers, 2004); b) restriction of the analysis only to the footprint membrane in TIRFM; c) possible heterogeneity in the state of TIRFM imaged vesicles in the exocytic cascade which makes upstream (undocked/unprimed) vesicles temporarily reluctant to the stimulus.

A second line of arguments comes from the study in bovine chromaffin cells employing a 'color-ageing' fluorophore fused to the ANF vesicle cargo protein (Duncan et al., 2003). It was shown in that work that preferentially only 'young' vesicles (aged <16 hours) displayed a highly restricted character of lateral movement beneath the membrane and, moreover, could readily undergo stimulated exocytosis. Similarly, NPY-Venus cargo molecules are packaged into the LDCVs on the stage of their biogenesis, thus the vesicles imaged with TIRFM in this work are 'young' (used at <8-10 hours after infection), and their trajectories were as well restricted down to jittering movement around steady positions (Fig. 2.5). Aforementioned arguments provide the validation to the use of NPY-Venus probe in studying dynamics of the fusion-competent large dense core vesicles.

With specific NPY-Venus labeling of LDCVs, measuring the surface density of granules calculated from the time-averaged TIRFM image is an approximate method to estimate the morphological vesicle docking at the plasma membrane. Good agreement of the vesicle density measured in this work with the results of electron microscopy quantification of LDCV distribution indicated that indeed this method can be used in TIRFM for fast screening of alterations in vesicle docking. This method, however tends to overestimate the size of the docked vesicle pool because of the relatively large depth illuminated by the evanescent wave ($3d$ ~360 nm) in comparison to the LDCV diameter (~80-120 nm). This means that for subtle differences in vesicle docking electron microscopy should be preferred, while estimation by TIRFM can be used with more pronounced effects (Tsuboi et al., 2005). The total number of labeled granules in a cell is important to consider but here it was assumed that investigated cellular genotypes did not affect either LDCV biogenesis nor loading them with the fluorescent label, as demonstrated e.g. in PC-12 cells (Schutz et al., 2005). Electron microscopy (data by Heidi de Wit) reported unchanged total numbers of LDCV in all experimental groups of chromaffin cells.

5.1.2 Tracking of single LDCVs: methods giving insights into biological mechanisms and its associated error sources

The properties of vesicle interaction with its environment can be studied by single particle tracking techniques. Deviations from unconstrained, random-walk-like diffusion would indicate the presence of some mechanism constraining free movement, providing drag or attaching tethers to the vesicle. The geometrical arrangement of vesicles scattered in the cytoplasm beneath the plasma membrane of a coverslip-attached (or rounded) cell suggests an axial symmetry of the system where the preferred axis is oriented perpendicular to the plane of the footprint membrane (or to the closest point at the plasma membrane in rounded cell). In other words, while intuitively the movement in the plane of the membrane should be isotropic for X and Y directions within that plane, the axial direction along Z seems to be unique. Indeed, the vesicles are generated in the central parts of the cell and need to make their way towards the membrane before they can be released. The membrane in this respect is the target with distributed affinity sites for the vesicles; thus the studies employing electron microscopy (Broadie et al., 1995; Voets et al., 2001; Sorensen et al., 2003; Borisovska et al., 2005) usually characterize the distance distribution of vesicles from the membrane (as also done in Fig. 4.4). The actin filaments form a significant cortical layer mainly parallel to the membrane (Trifaro et al., 2000) which may also contribute to the symmetry of the space where vesicles reside. This suggests that the properties of vesicle movement in XY plane may differ from those along Z axis. In addition, position measurements with TIRFM principally differ for XY and Z directions. Each method has its own source of error and precision: the spatial intensity distribution in the vesicle image and its integral (total intensity) are used for determining the vesicle position in respective cases (2.2.1). These arguments stress the importance of separating XY and Z movement analysis.

A large proportion of the known studies utilizing single vesicle tracking techniques did not distinguish between diffusion in XY and Z directions, reporting a composite, so-called 3D diffusion coefficient $D^{(3)}$ (Steyer and Almers, 1999; Oheim and Stuhmer, 2000; Li et al., 2004). Only few consider XY and Z movement of labeled vesicles as different processes (Johns et al., 2001; Manneville et al., 2003). Indeed, a study of Weibel-Palade body movement with TIRFM (Manneville et al., 2003) reported up to two orders of magnitude smaller D_Z (~10^{-5} $\mu m^2/s$) compared to the D_{XY} (~10^{-3} $\mu m^2/s$). Similarly, approximately one order of magnitude smaller D_Z (~10^{-4} $\mu m^2/s$ and 10^{-5} $\mu m^2/s$) compared to D_{XY} (~10^{-3} $\mu m^2/s$ and 10^{-4} $\mu m^2/s$) for caged and free diffusion, respectively, were found in this study for NPY-Venus vesicles in chromaffin cells (Suppl. Tables S.2-S.3).

Mean square displacement analysis for different modes of movement (Saxton and Jacobson, 1997) was so far the most common approach introduced first for analysis of singe vesicle movement in (Steyer and Almers, 1999). More recently, it was applied in a number of other studies of single vesicle dynamics (Oheim and Stuhmer, 2000; Johns et

al., 2001; Manneville et al., 2003; Li et al., 2004). It is useful to determine the diffusion coefficient of tracked vesicles in free space or inside the apparent cage when movement is restricted. However, there are several problems associated with this analysis. First, the shape of experimentally determined MSD plots does not necessarily report the mode of underlying movement due to the limited tracking precision by e.g. noise or mechanical drifts. On the other hand, classification of the movement mode based on the MSD plot can be problematic for certain combinations of parameters of the diffusion model. For example, small physical cage size or large $D_{in\,cage}$ can result in a MSD plot that can be misclassified as 'free' diffusion with the diffusion coefficient indeed equal to the true diffusion coefficient of the cage. The combination of these factors was most likely a reason why MSD analysis of most of immobile controls revealed 'free' diffusion with very small D_{free} while 'caged' diffusion corresponding to the tracking noise was expected. Also, the fitting of experimental MSD plots with the model equations can be problematic. The error increases with increasing time in MSD plots (Qian et al., 1991) thus making the estimation of D from only the first two points of a MSD plot most accurate. This, however is not possible for a 'caged' model where the MSD at late time points determines the cage movement.

For analysis of Z movement these concerns become even more critical because the axial position is directly derived from the fluorescence intensity and thus the apparent diffusion estimate (also the first pair of points in the MSD plot) is strongly affected by noise in fluorescence intensity. Especially at the fast image sampling rate, when the signal-to-noise ratio is compromised in favor of high time resolution, the precision of MSD analysis drops dramatically. This is illustrated by the MSD_Z analysis results (Fig. 4.6) where the precision determined by tracking immobile objects (beads or fixed vesicles) was of the same order of magnitude the order of magnitudes as for vesicles in living cells. This means, firstly, that the vesicles are strongly restricted compared to the free particles of similar size as noticed already e.g. in (Steyer and Almers, 1999). Secondly, one needs another way method for analysis of single vesicle trajectories and movement restriction.

In this work, an alternative analysis was used for axial (Z) movement, namely the velocity autocorrelation function (or ΔZ-ACF) analysis. Autocorrelation analysis reveals the time range at which interactions take place between the vesicle and its environment, modifying the Brownian diffusion (Qian et al., 1991). Velocity autocorrelation should be used with TIRFM rather than correlation of coordinates because differentiation of Z before correlation (eq. 2.13) solves the problem of unknown $Z^0_{\min}$ offset. In addition, ΔZ-ACF serves as a 'barrier filter' for fast uncorrelated noise in coordinates e.g. shot noise or camera read-out noise. Being more sensitive to interactions which influence the movement, ΔZ-ACF works on the same data as MSD, and these functions are related. It can be seen from the equation 2.16 that for a ΔZ-ACF with only one non-zero point at $\tau = 0$, the corresponding MSD plot would be a straight line (Fig. 2.6), i.e. signifying random free diffusion (Qian et al., 1991). The negative component in the ΔZ-ACF,

depending on its amplitude and decay kinetics corresponds to a decrease of the slope in the MSD plot, approaching the shape of 'caged' diffusion. The NPA parameter defined in this work is thus an appropriate measure of tethering forces acting on the diffusing vesicle, because the time binning with subsequent summation of the first two binned points approximates the negative part of the ΔZ-ACF integral over the time $\tau > \delta t$ (see 2.2.3 for detailed explanations). The negative area under the ΔZ-ACF curve is the result of the movement restrictions provided by the environment.

Correlation analysis can be used on practice in conjunction with single particle tracking. Time correlation of coordinates, for example, was recently employed in TIRFM analysis of microspheres tethered to the coverslip (Blumberg et al., 2005). Velocity autocorrelation analysis of vesicle dynamics in living cells is rather a novel approach. It was applied, to my knowledge, in only one paper (Johns et al., 2001). In this valuable study, where Z-movement of vesicles and its restriction were investigated and discussed in detail, the authors performed ΔZ-ACF analysis of axial vesicle movement beneath the plasma membrane of bovine chromaffin cells. The authors described the negative component in ΔZ-ACF at τ=0.5 s as a property due to vesicle diffusion restriction or tethering (Fig. 2.7). However, the reported sampling rate of vesicle tracking was also δt=0.5 s. Taking into account the possible problems associated with the zero and the first points of ΔZ-ACF (discussed in sub-section 2.2.3, eqs. 2.13-2.15) and the fact that the amplitude of their ΔZ-ACF negative component (~600 nm^2) was comparable in absolute value to the zero point amplitude (Fig. 2.7), one should be cautious in interpreting these data. In contrast, in this work, the artifact of the first point was avoided resulting in much smaller negative amplitudes (NPA~10 nm^2) of the ΔZ-ACF, in line with the small size of the Z-cage (Fig. 4.6).

In addition to assessing tethering by single vesicle tracking, different docking modes were investigated by analysis of vesicle residency times at the plasma membrane using an automated algorithm (see sub-section 2.2.4). In contrast to the ΔZ-ACF assay where subtle axial displacements of docked vesicles beneath the membrane ('jittering') were probed, the residency time analysis measures 'all-or-none' events of vesicle docking, whereby any vesicle detected by the algorithm (i.e. at a small distance to the membrane as determined by the evanescent wave penetration depth) was considered to be 'morphologically docked'. This approach is intended to estimate the kinetic rates of reversible vesicle docking, i.e. affinity of docked state(s), while ΔZ-ACF analysis allows estimation of the tether quality of docked vesicles. Combination of these two approaches allowed distinguishing between two different aspects of docking: affinity of vesicles to the hypothetic docking platform and mechanical properties of the vesicle connection to that platform or the membrane.

5.1.3 Computer simulations as a tool to aid understanding underlying mechanisms of vesicle movement restriction

Simulations of single vesicle movement with parameters mimicking the experimental conditions, performed in this work (section 4.3), proved to be useful for understanding the processes responsible for axial movement restriction. On the other hand, simulation results reassured the functionality of the analysis software used also on the experimental data and suggested possible interpretations of experimental findings.

Three different mechanisms of vesicle movement restriction can be envisioned: mechanical barriers and tethering forces, the latter of stochastic or deterministic nature.

An interesting effect in the NPA was discovered with all restriction models tested. The NPA (or negative component of ΔZ-ACF) reached the maximum amplitude only within a certain optimal range of the restriction degree or tether strength. When the simulated vesicle was either allowed to diffuse freely or was restricted within the small space, or strongly tethered, the NPA was approaching its minimum. Thus, the NPA decreases at both limits: for very weak and very strong tethering. The location of the maximal NPA value depends on the diffusion coefficient of the vesicle in the free space, i.e. on how fast the vesicle can reach the opposite wall of the restricting cage or how much space it can freely explore until the tethers activate. The free diffusion coefficient of the vesicle thus functions as an additional parameter which can bring the NPA to its maximum in certain range of diffusional speed. On the other hand, in the simulations usually only one parameter was varied at a time, but in experiment, most likely multiple parameters are subject to change between cellular phenotypes. This suggests that correct interpretation of the measured NPA and the underlying mechanisms of vesicle docking/tethering requires additional control experiments (e.g. cage removal by actin depolymerization) refining the conclusions. The information on tethering mechanisms is contained not only in the NPA amplitude but also in the ΔZ-ACF decay to zero when correlation time τ increases. Unfortunately, quantification of this property in measured ΔZ-ACF was complicated by the functions decaying to zero practically within the first couple of points and usually displaying large fluctuations within this decaying phase.

Another interesting and not straightforward finding made with the simulations of stochastic tethers was that not only the steady state activation of tether ensembles, but also their kinetics influenced effective tethering and the NPA (Fig. 4.12). This finding is important because it is likely, that the vesicle docking machinery consists of several tethering units with several states or conformations. Kinetics of switching between conformations (in analogy to activation/deactivation of simulated stochastic tethers) could thus influence the effective tethering.

5.2 Molecular players and properties of the vesicle docking machinery

5.2.1 Munc18-1 as a factor promoting strongly tethered docking of LDCVs upstream of fusion

The main aim of this study was deciphering mechanism of large dense core vesicle docking. As a starting point, chromaffin cells from *munc18-1* null mutant (M18 KO) mouse embryos were used, since Munc18-1 has been identified as an essential vesicle docking factor (Verhage et al., 2000; Voets et al., 2001).

The ΔZ-ACF analysis of vesicle 'jittering' reported decreased NPA values in M18 KO cells by a factor of 4-5 (Figs. 4.7-4.8), indicating that vesicles in embryonic chromaffin cells were tethered differently in the absence of Munc18-1. The NPA value on its own does not provide information on where the vesicles were tethered to, docking sites at the plasma membrane or to other structures near the membrane but separated from it. Also, as discussed above in 5.1.3, smaller NPA values can mean weaker tethering as well as stronger. Thus, there are two possible explanations of the NPA results in M18 KO cells:

a) difference in the NPA reflects different tethering of LDCVs to the plasma membrane, with stronger tethering when Munc18-1 is present. The role of the membrane as a high affinity site is supported by the electron microscopy results (Fig. 4.4) and the fact that the NPA as well as the vesicle density could be rescued with acute Munc18-1 overexpression. The residency time analysis discussed later also supports this interpretation. Small NPA values in M18 KO cells would be then due to vesicle jittering movement, either caused by weaker retaining forces or by a slower (or much faster, on the other limit) diffusion in a restricted space of same cage size as in WT or Rescue cells;

b) smaller NPA in M18 KO cells can alternatively be due to stronger tethering. The ΔZ-ACF in M18 KO decays to zero within one time point which may mean increased tethering forces or strong restriction. However, given the almost random scattering of vesicles in M18 KO cells (Fig. 4.4), it is then likely that the vesicles are tethered without contact to the plasma membrane, e.g. by actin cytomatrix.

The latter possibility suggests a role of actin cytoskeleton in vesicle tethering. It is known, that the actin cytomatrix forms a cortex-like rim beneath the membrane that influences exocytosis in bovine chromaffin cells, reviewed in (Trifaro et al., 2002). The actin cytoskeleton was shown to influence the mobility of LDCVs and other organelles (Oheim and Stuhmer, 2000; Manneville et al., 2003). Moreover, it was found to potentially interact or be regulated by Munc18-1 (Bhaskar et al., 2004). To address this point, actin dynamics were perturbed in M18 KO and WT cells by latrunculin A treatment. Lateral diffusion coefficients were decreased after actin depolymerization in the M18 KO and WT cells, supporting the $D^{(3)}$ measurements performed previously (Oheim and Stuhmer, 2000; Manneville et al., 2003). However, the ΔZ-ACF analysis of axial movement did not reveal significant NPA changes in M18 KO cells after actin

depolymerization. If the intact actin-dependent vesicle tethering in M18 KO was stronger than in WT, reported by smaller NPA, the non-increased NPA after actin removal could indicate a switch to another limit – weak tethering in LatrA-treated M18 KO cells. This is unlikely because the axial diffusion coefficients D_Z did not change significantly by LatrA treatment in either M18 KO or WT cells (Suppl. Table S.3). Another fact is that the vesicle density at the footprint (Fig. 4.14), assayed by TIRFM as well as by EM, was restored by LatrA treatment in M18 KO cells. This suggests the opposite, namely that vesicles in M18 KO cells acquired additional tethering to the plasma membrane. Slight increase in M18 KO NPA by LatrA may thus, indeed, indicate a switch from weak restriction of vesicles to somewhat stronger tethering at the membrane. This small effect may be due to the prevalence of weak membrane-associated tethers in the absence of actin meshwork, which in intact M18 KO cells might favor vesicle undocking/detachment from the membrane. The decrease of NPA in WT+LatrA cells can be, in turn, due to the further increase of tethering forces if one assumes the actin being a barrier or negative modulator of docking/tethering.

To summarize this discussion, the first hypothesis suggesting strong tethering to the plasma membrane in WT and weak in M18 KO reflected by the large and small NPA, respectively, seems more likely. This membrane tethering model is further corroborated by the observation that the average NPA increases in WT and Rescue in vicinity to the plasma membrane but is small at all the distances in M18 KO (Fig. 4.13). This also excludes a simple explanation of differences in vesicle tethering between M18 KO and WT, namely that vesicle movement is constricted to larger degree closer to the membrane (Oheim and Stuhmer, 2000; Johns et al., 2001), given the obvious differences in spatial distribution of vesicles in these genotypes.

Another important finding is that upon dissociation of the submembrane actin cytoskeleton in the M18 KO cells, many vesicles reached the target, and that electronmicrographs were indistinguishable from those of wildtype cells, while the NPA was still very low, and secretion remained fully inhibited (Gulyás-Kovács, 2005). This indicated that a considerable discrepancy can occur between morphological and functional docking. Morphological docking is not sufficient to support secretion, but Munc18-1 dependent strong tethering is a prerequisite in preparation for fusion. Moreover, this also underscores that morphological assessment of docking may not reveal important functional docking defects.

The action of the phorbol ester PMA was principally different. Similarly to the actin depolymerization with LatrA, PMA restored the vesicle docking to the plasma membrane in M18 KO cells, measured with TIRFM (Fig. 4.15) and EM (unpublished data by Heidi de Wit), which could be attributed only to actin cortex disassembly by phorbol ester-activated modulation of actin (Trifaro et al., 2002). However, the LDCV secretion in M18 KO, in contrast to the LatrA-mediated actin depolymerization, was rescued (Gulyás-Kovács, 2005). But the NPA remained small in M18 KO after PMA application and was reduced in WT. How did the PMA modify tethering forces in M18 KO? In case the

tethering is considered to be weak in intact M18 KO (as discussed before), no change in NPA would mean either no change in tethering (remained weak) or a switch to very strong tethering. The latter is supported by a change in the ΔZ -ACF shape (Fig. 4.15) in M18 KO towards WT (Fig. 4.7): the negative component comprises more than one time point. Also, the free diffusion coefficient D_Z increased in M18 KO, to the level of WT cells (Suppl. Table S.3). This suggests that PMA treatment recovered 'functional' tethering in M18 KO which can support downstream secretion of the vesicles as confirmed by electrophysiology. Along this line, the PMA action increased tethering in WT (seen now as decrease in NPA, like in the case of LatrA) due to the absence of actin filaments which most likely contribute to the sub-membrane movement of LDCVs. Similarly to the enhancement of strong 'functional' tethering, PMA potentiated the secretion also in the WT cells. The mechanism of secretion rescue in M18 KO by phorbol ester is not clear. The Munc18-1 independent by-pass from morphological to functional docking can most likely reflect activation of Munc13s (Ashery et al., 2000; Rhee et al., 2002; Gladycheva et al., 2004) believed to stabilize the open state of Syntaxin-1a. Further experiments are necessary to delineate the role of phorbol esters in vesicle docking.

Next, the role of the t-SNARE Syntaxin-1a in vesicle docking was probed by the botulinum neurotoxin C1 light chain overexpression in WT cells. Surprisingly, Syntaxin-1a cleavage resulted in a small decrease of vesicle docking assessed with TIRFM. This is in contrast to the normal synaptic vesicle docking in the Drosophila NMJ and Giant synapse of squid in the absence of Syntaxin-1a (Broadie et al., 1995; O'Connor et al., 1997). But intact synaptic morphology in M18 KO neurons co-existing with the impaired docking in chromaffin cells (Verhage et al., 2000; Voets et al., 2001) suggests that the LDCV docking mechanism may differ from the synaptic vesicle docking in presynaptic terminals. The NPA decreased slightly but significantly upon BoNT-C1 light chain expression, which was not the case when the v-SNAREs Synaptobrevin II (VAMP2) and Cellubrevin or (VAMP3) were cleaved by overexpressed tetanus toxin light chain. The vesicle density at the footprint was also not changed upon TeNT expression, in line with the normal morphological docking in the single VAMP2 or even double VAMP2/VAMP3 null mutants (Schoch et al., 2001; Borisovska et al., 2005). The role of the third SNARE partner, SNAP-25A was examined using chromaffin cells from SNAP-25A null mutant mice. Neither vesicle density at the footprint, in line with the EM phenotype (Sorensen et al., 2003), nor NPA values were different from the control WT cells.

To summarize the SNARE experiments, only proteolytic cleavage of the t-SNARE Syntaxin resulted in modification of vesicle tethering, scored with the NPA value. The SNARE proteins were originally proposed to account for vesicle docking (Sollner et al., 1993), supported by a more recent *in vitro* studies (Fix et al., 2004; Liu et al., 2005). Other studies showed that Synaptotagmin interaction with SNAP-25 might induce vesicle docking to the plasma membrane (Schiavo et al., 1997; Chieregatti et al., 2002). However, studies in living cells, most of which involved transgenic animal models,

showed that SNAREs are required for vesicle fusion but not for morphological vesicle docking (Hunt et al., 1994; Broadie et al., 1995; O'Connor et al., 1997; Schoch et al., 2001; Sorensen et al., 2003; Borisovska et al., 2005; Sakaba et al., 2005; Young, 2005). While the data presented here are in agreement with these studies, a Syntaxin-dependent tethering was identified upstream of priming and/or fusion. Synaptobrevin/VAMP and SNAP-25A seem to be dispensable at this stage of functional docking/tethering upstream of fusion. This proposes a role for Syntaxin as part of the initial 'docking platform', where vesicles can dock morphologically, as well as part of a switch to the functional docking/tethering in preparation for fusion. This is supported by the finding that Syntaxin-1a interacts with the voltage-gated calcium channels to form the molecular clusters implicated in the docking/priming/fusion of vesicles (Catterall, 1999; Lang et al., 2001). Since Syntaxin is a well-known interaction partner of Munc18-1, the absence of Munc18-1 may be one reason for the failure of Syntaxin to transit from the closed state (Dulubova et al., 1999; Misura et al., 2000) to the functional vesicle docking platform associated with calcium channels (Li et al., 2004; Yokoyama et al., 2005), probably in combination with Synaptotagmin (Schiavo et al., 1997; Reist et al., 1998; Chieregatti et al., 2002). The role of Synaptotagmin in docking, suggested also by studies in cells (Reist et al., 1998; Fukuda et al., 2000), should be investigated separately with the TIRFM.

To investigate the role of the interaction between Munc18-1 and Syntaxin-1a in organizing functional vesicle docking, experiments were performed where Munc18-$1^{D34N;M38V}$, a mutant deficient in Syntaxin-1a binding, or the second isoform Munc18-2 were overexpressed on the M18 KO null genetic background. As mentioned in the sub-section 4.4.4, electron microscopy and electrophysiological measurements revealed differential effects of these two molecules. Munc18-$1^{D34N;M38V}$ (Naren et al., 1997) led to the partial rescue of docking (to 25% of Rescue docked vesicles) and secretion (to ~60% of Rescue burst) in M18 KO cells without producing additional effects when overexpressed on the WT background. Munc18-2, an ubiquitous isoform expressed in epithelial cells and functional interaction partner of Syntxin-3 (Riento et al., 2000), is able to bind tightly also to Syntaxin-1a (Hata and Sudhof, 1995). Munc18-2 expression in M18 KO cells was less efficient in rescuing of secretion (~30%), but fully rescued morphological docking. Moreover, overexpression of Munc18-2 on the WT background resulted in a dominant negative effect, probably due to the strong Syntaxin-1a binding but low efficiency in promoting secretion, (Gulyás-Kovács, in preparation).

Using TIRFM, it was surprisingly found that not only Munc18-2 but also Munc18-$1^{D34N;M38V}$ restored the reduced vesicle density in M18 KO cells. The assessment of tethering with the NPA showed that both proteins rescued the NPA from the low level in M18 KO cell to the WT level, i.e. to a similar extend. Both NPA values were, however, still smaller than for cells rescued by the wildtype Munc18-1 expression (Fig. 4.16). These results may be explained in the following. The difference in the rescue of secretion, as measured by capacitance upon Ca^{2+}-uncaging, was not as strong as the difference between the residual M18 KO secretion and exocytic responses of WT or Rescue cells,

meaning that the NPA approach might be not sensitive enough to reliably report such differences. Also, detection of differences in functional tethering (if there are) between Munc18-1$^{D34N;M38V}$ and Munc18-2 cells by the NPA value might be complicated by the larger expression level of these proteins, required for reliable detection of the NPY-Venus loaded vesicles with the TIRFM imaging. Indeed, electrophysiological experiments and EM were preformed as soon as four hours after infection with the Semliki Forest viral particles, while TIRFM experiments were carried out in the time window 8-10 hours after infection, leading to much higher expression levels of the proteins of interest. This can also explain the full rescue of docking by Munc18-1$^{D34N;M38V}$ when assessed by TIRFM. On the other hand, an almost 60% rescue of secretion by the mutant, deficient in binding to Syntaxin, strongly speaks for a Syntaxin-independent function of Munc18-1. This could also be the reason why differences in tethering could not be detected by TIRFM, especially given the high expression levels of the proteins. Syntaxin-independent functions of Munc-18 protein were suggested in at least two other studies employing similar Syntaxin-binding deficient mutants of Munc-18 (Ciufo et al., 2004; Schutz et al., 2005). In these studies, the interaction of Munc-18 with Mint1 protein (Biederer and Sudhof, 2000) was suggested as a possible pathway of Syntaxin-independent action. Mint1, in turn, via CASK, can influence the F-actin nucleation at the plasma membrane-associated neurexin (Biederer and Sudhof, 2001). The possible role for indirect F-actin modulation by Munc18-1 is further supported by its interaction with and possible activation of the cyclin-dependent kinase Cdk5 (Shetty et al., 1995; Veeranna et al., 1997; Bhaskar et al., 2004). The protein kinase Cdk5 can modulate cytoskeletal proteins, including F-actin, via a cascade of phosphorylations (Smith, 2003). Evidence for this pathway in the literature, however, is not very strong. Although the molecular mechanism is not clear, the effect of Munc18-1 overexpression on the actin cortex was also observed in a collaborating group (Bas Konijnenburg, Hedi de Wit) with phalloidin staining. The actin cortex was thicker in M18 KO cells and thinned significantly by Munc18 overexpression, indicative of massive F-actin depolymerization. Thus, one of the Syntaxin-independent Munc-18 functions may comprise modulation of sub-membrane actin, which, as was shown by the LatrA experiments, can facilitate morphological (but not functional) docking.

5.2.2 Munc18-1 increases vesicle delivery rate and favors high-affinity functional docking. Three-state LDCV docking model.

The vesicle tethering to the plasma membrane and its molecular aspects were examined with the analysis of jittering movement, as discussed above. In this sub-section, I shall discuss the results of the complementary analysis of vesicle residency time at the membrane. This analysis addressed the process of the vesicle's approach to the membrane and its capture by tethering mechanisms.

The residency time analysis was introduced as a means to discriminate different docking states. This analysis showed that the majority of the detected vesicles appearing in the TIRF plane were visible only very transiently (less than 1 s), suggesting that they had not attached to the membrane. These vesicles, here referred to as 'unretained visitors', corresponded to the first peak in the residency time histogram (Fig. 4.19). Only some of the arriving vesicles were captured by tethering mechanisms suggesting that successful retention of arriving vesicles is a relatively rare event. Among the vesicles that were captured at the target, at least two groups could be identified from the residency time and vesicle hit-rate histograms (Fig. 4.20): vesicles with residency times between 1 and 10 seconds (short-retained or low-affinity tethered), and vesicles with residency time τ >10 s (long-retained or high-affinity tethered). The existence of the latter state is evidenced by the long tail in the residency time histogram. Since fitting of the distribution with exponentially distributed lifetime states (Fig. 4.19b) showed that the tail could not be copied with only one high-affinity state, the existence of several closely spaced long-lived states is proposed.

It is difficult to conclude that these long-lived vesicles comprising the distribution tail belonged to qualitatively different populations. The analysis of the average occurrence distribution, which corrects for multiple scoring of short-lived events in the whole-ensemble histogram, helped to quantify the relative occurrence of the different states in the different phenotypes and to compare these data to the electron microscopy results. Based on these data one can calculate that at any given time (or in an EM snapshot picture) the population of high-affinity tethered vesicles constitutes approximately 77% of the vesicles at the membrane, the low-affinity tethered vesicles 20% and the 'unretained visitors' 3%. This is a very important piece of information, unique to live imaging, since EM does not retain the information on dynamic properties of observed vesicles.

Taken into account that the NPA analysis was restricted to docked vesicles which spent a certain time at the membrane, the combined data of the residency time and the ΔZ -ACF analysis (discussed in the previous sub-section) were summarized in a three-state model of LDCV docking (Fig. 5.1).

The model introduces three sequential states: an unretained, in which the vesicles are not tethered to the membrane yet, and two docked states. The low-affinity docking is associated in the model with weak tethering (small NPA), and the high-affinity docking state with strong tethering (large NPA). The latter state is suggested to be Munc18-1/Syntaxin-1a dependent. Existence of two populations of tethered vesicles is favored for the following reasons:

1) In M18 KO cells the number of vesicles with residency times longer than 10 s was significantly decreased, whereas the number of vesicles between 1 and 10 s at the membrane was not strongly affected (when compared between KO and WT, Fig. 4.21b);

2) The NPA, reporting stringent tethering of membrane-resident vesicles, was decreased by a factor of 4-5 in M18 KO cells;

3) Latrunculin A treatment rescued docking in M18 KO cells to the WT level, but the morphologically docked vesicles could not fuse and had an unaltered, low NPA;

4) The secretion efficiency was very low in M18 KO deficient cells, while low-affinity docking was unaffected in these cells;

5) Cleavage or deletion of SNAREs inhibited vesicle fusion but not morphological docking. Syntaxin-1a cleavage with BoNT-C1 produced a decrease in tethering strength.

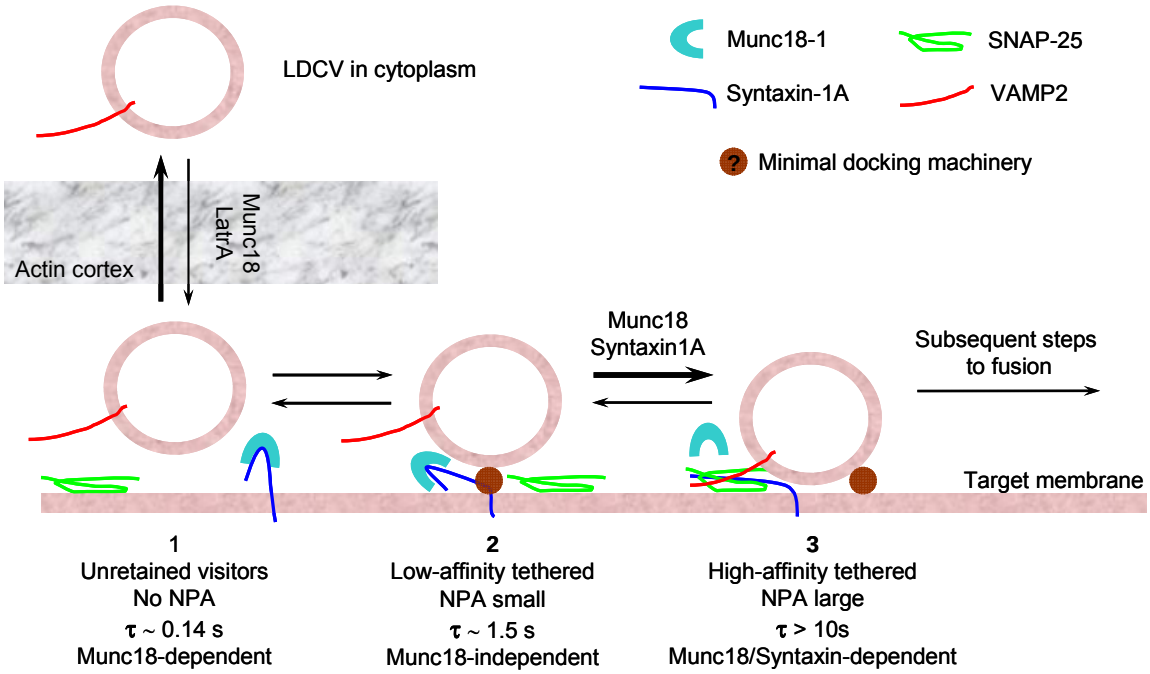

Fig. 5.1. A model introducing distinct steps in large dense core vesicle docking to the plasma membrane. After translocation across the actin cortex, the vesicles can acquire at least three consequent states: 1) 'unretained visitors' – vesicles with very short residency time which do not touch/dock to the membrane. The state is Munc18-dependent due to the most likely facilitation of vesicle translocation or vesicle delivery rate by Munc18; 2) low-affinity docked/tethered state (average residency time τ ~1.5 s) corresponding to 'morphological docking' with the help of unknown minimal docking machinery. The state is fingerprinted with the small NPA (weak tether). Transition to the next state requires and is favored by Munc18-1, Syntaxin and their interaction; 3) high-affinity (τ >10 s) strongly tethered Munc18-dependent docking state corresponding to the 'functional docking' which allows downstream priming/fusion.

For these reasons, it seems necessary to discriminate low- and high-affinity tethered states in the docking process, fingerprinted with the smaller and larger NPA values. Based on the presented data, one may conclude that low-affinity tethering is not sufficient to support secretion. High-affinity state, infrequently occurring among total number of events, is a prerequisite in preparation for fusion. Low-affinity tethering may represent unknown, minimal tethers, which are stabilized and/or converted into high affinity tethers by Munc18-1 involving Syntaxin-1a. The phorbol ester PMA can by-pass the Munc18 requirement for switching between morphological and functional docking states, probably

by direct activation of Munc13-1 (Ashery et al., 2000; Rhee et al., 2002) and thus possible modification of the Syntaxin-1a state.

In addition to its role in establishing the high-affinity tethered state, Munc18-1 appears to be involved also in regulating the vesicle delivery rate. In the model (Fig. 5.1) this is indicated by a translocation step across the actin cytomatrix which is facilitated by Munc18-1 (can be promoted also by LatrA and PMA). Most likely, as discussed already in 5.2.1, this effect reflects an indirect modulation of the actin cytoskeleton by Munc18 (Shetty et al., 1995; Veeranna et al., 1997). Munc18 thus might simply increase the mesh width of the actin cortex and hence vesicle delivery. This can explain the increase in the frequency of 'unretained visitors' in WT and Rescue cells compared to the M18 KO, as well as the significantly increased occurrence of the low- and high-affinity docked vesicles in the Rescue cells – due to the up-regulated supply of vesicles upstream of both docking states. The same argument can be used to explain of the complete rescue of all docking states when overexpressing the Munc18-1 mutant deficient in Syntaxin-1 binding or the Munc18-2 isoform (Fig. 4.22). The actin cytomatrix itself presents a barrier for the translocation step, as supported by studies in bovine chromaffin cells (Vitale et al., 1995; Trifaro et al., 2002).

The collective consequence of the two separate functions of Munc18-1 in chromaffin cells is the control of both, morphological docking and secretion capacity. The data underscore also that morphological assessment of docking may not reveal important functional docking defects. The mechanism of morphological docking, however, remains unclear. The *in vitro* situation, where SNAREs are the necessary and sufficient machinery for vesicle docking and fusion (Fix et al., 2004; Liu et al., 2005) seems not to be applicable to living cells. Also, the study (Liu et al., 2005) demonstrated almost fully irreversible docking, while existence of different docking states with distinct lifetimes demonstrates reversible inter-state transitions (Fig. 5.1), which is supported also by other studies (Steyer et al., 1997; Murthy and Stevens, 1999; Zenisek et al., 2000). Another candidate for reversible minimal docking is Synaptotagmin (Reist et al., 1998; Fukuda et al., 2000). Other studies suggested the t-SNARE SNAP-25 to be a binding partner for Synaptotagmin during vesicle docking (Schiavo et al., 1997; Chieregatti et al., 2002), however deletion of SNAP-25 examined here and previously in chromaffin cells (Sorensen et al., 2003) did not lead to impaired morphological docking. The Sec6/8 proteins of the exocyst complex might be responsible for LDCV docking (Hsu et al., 1999; Tsuboi et al., 2005), but the role of this complex for vesicle docking in chromaffin cells and synaptic terminals is not clear.

On the other hand, existence of a minimal morphological docking machinery proposed here may explain the intact LDCV and synaptic vesicle docking phenotypes in most of deletion mutants of proteins belonging to the exocytic machinery and most likely acting downstream of morphological docking (Hunt et al., 1994; Broadie et al., 1995; O'Connor et al., 1997; Schoch et al., 2001; Washbourne et al., 2002; Sorensen et al., 2003; Borisovska et al., 2005). The dual function of Munc18-1 for vesicle delivery and

promoting functional docking, proposed here, could explain why the Munc18-1 null mutant is almost the only example of impaired vesicle docking (Voets et al., 2001; Weimer et al., 2003). Additional functions of Munc18-1 in secretion pathway like interaction with Mint1 (Schutz et al., 2005) may exist.

5.3 Outlook

In this work, two distinct docking states of LDCV were proposed: morphological and functional. The precise molecular mechanisms and constituents of the minimal docking machinery are not yet uncovered and the models existing in the literature remain controversial. The next steps in delineation of the docking mechanisms may be the investigation of the role of Synaptotagmin isoforms and their binding to SNAREs and the investigation of the possible role of mammalian exocyst complex components. The methods developed in this work for quantitative analysis of TIRFM imaging data can be successfully used for these purposes. Additional experiments using approaches of molecular biology and ultrastructural morphology will be necessary for the refinement of the model obtained from live imaging.

Another line of research can employ live TIRFM imaging using fluorescently tagged versions of putative key players in the docking machinery (like Munc18, Syntaxin, Synaptotagmin etc.), bearing specific mutations that affect their interactions. Live fluorescent imaging techniques with high spatial resolution and single molecule sensitivity (like TIRFM) can be used to study the dynamics of these proteins and their complexes, the putative ‘docking platforms’, simultaneously with real-time monitoring of vesicle docking. Spatiotemporal correlation of vesicle docking events and ‘docking platform’ dynamics could provide further insight into the molecular mechanisms of vesicle docking/priming in living cells.

Summary

Secretory vesicles dock at the plasma membrane and proceed through several steps in preparation for Ca^{2+}-triggered fusion. The molecular events between the first morphological contact with the membrane and primed state are poorly understood. In this work, total internal reflection microscopy (TIRFM) was used for real-time imaging of single fluorescently labeled large dense core vesicles (LDCVs) beneath the plasma membrane of intact adrenal chromaffin cells. TIRFM imaging was combined with the single particle tracking, correlation and residency time analysis, and assisted by stochastic modeling, to better characterize molecular events in vesicle docking. Cells from *munc18-1* null mutant mice were chosen as a model system since this t-SNARE Syntaxin-1a interacting protein is known to be essential for vesicle docking and fusion.

Footprint density of NPY-Venus labeled LDCVs, measured with TIRFM, was found to reflect alterations in morphological docking, confirming EM ultrastructural differences in *munc18-1* null (M18 KO) vs. wildtype (WT) and null+Munc18-1 (Rescue) cells. Analysis of the 'jittering' movement of docked LDCV in axial direction by the velocity autocorrelation function revealed a distinct negative autocorrelation component at small τ ~0.5-1 s, which was 4-5 times smaller in M18 KO cells than in WT. The negative autocorrelation amplitude (NPA) was restored in Rescue cells and partially recovered by overexpressing mutated Munc18-1$^{D34N;M38V}$ with low affinity for Syntaxin-1a or Munc18-2. Phorbol ester PMA rescued docking and secretion in M18 KO cells, but the NPA remained small. Computer simulations of LDCV movement showed that the NPA is determined by restrictions applied to the free diffusion model. The small NPA can be attributed to either strongly restricted movement by encagement or tethering forces, or nearly free diffusion with weak restrictions. Since the tethering could be provided by the actin cytomatrix, thickened in the M18 KO cells, the effect of pharmacological actin depolymerization on the NPA was examined. Actin cortex removal led to restoration of morphological docking in M18 KO cells without altering the NPA or secretion, suggesting weak and non-functional tethering/docking of vesicles in M18 KO cells. The role of SNAREs in docking was probed in *SNAP-25A* null mutant cells and by neurotoxin-mediated cleavage of SNAREs: only BoNT-C1 light chain overexpression reduced the NPA. By developing and using an automated analysis of vesicle residency time at the membrane, approaching vesicles were shown to infrequently dock with only some 'visitors' being captured by at least two different tethering modes, low and high-affinity. Munc18-1 increased the population of the latter state as well as the overall vesicle delivery rate.

In conclusion, three distinct docking states were identified where docking vesicles either undock immediately or are captured by minimal docking/tethering principles and converted into a Munc18-1/Syntaxin-dependent, tightly tethered, fusion competent state.

Supplementary Tables

Table S.1. Proposed roles for Munc18/Sec1 proteins in secretion

Role as a docking factor	Interactions with SNAREs before/at the priming stage	Role in the late fusion steps	Other interactions implicated in effects on secretion
LDCVs in neurosecretory cells (Voets et al., 2001; Korteweg et al., 2005)	Structural and conformational evidences: positive regulator of secretion (Dulubova et al., 1999; Misura et al., 2000)	Fusion pore modulation (Fisher et al., 2001; Barclay et al., 2003; Ciufo et al., 2004)	SNARE-independent mechanisms via interaction with Mints (Ciufo et al., 2004; Schutz et al., 2005)
Vesicles in *C. elegance* NMJ (Weimer et al., 2003)	Yeast secretion: positive regulator (Carr et al., 1999; Scott et al., 2004)		Syntaxin trafficking to the plasma membrane (Rowe et al., 2001)
	D. melanogaster Rop: negative regulator (Schulze et al., 1994; Wu et al., 2001)		Modulation of actin cytoskeleton via Cdk5 (Shetty et al., 1995; Veeranna et al., 1997)
			Relieve of Ca2+ channels inactivation by Syntaxin (Gladycheva et al., 2004; Mitchell and Ryan, 2005)
Possible modulation pathways of Munc18-1	PKC-mediated phosphorylation at residues Ser313, Ser306 (Fujita et al., 1996)	Cdk5-mediated phosphorylation at Thr574 (Fletcher et al., 1999)	

Table S.2. Mean square displacement analysis summary for LDCV lateral (XY) movement. Data are mean ± SEM.

Phenotype	Average MSD fitting parameters				Diffusion type frequency		Total
	R_{cage}	$D_{in\ cage}$	D_{cage}	D_{free}	Cage	Free	
	nm	$(\times 10^{-3})\ \mu m^2/s$			%		ves
WT	27.5±2.2	4.38±1.0	0.16±0.04	1.76±0.40	45	48	254
M18 KO	40.7±3.2	8.73±2.96	0.17±0.05	0.42±0.14	23	67	137
KO+M18-1	46.8±3.5	15.5±5.2	0.26±0.07	1.29±0.25	30	55	128
KO+ M18-1$^{D34N;M38V}$	40.4±4.6	4.95±0.99	0.16±0.05	0.81±0.02	19	74	178
WT+LatrA	37.7±2.4	7.33±1.59	0.21±0.06	0.15±0.09	47	45	115
M18 KO+ LatrA	38.0±2.9	8.33±1.62	0.10±0.02	0.17±0.06	38	55	122
M18 KO+ PMA	35.0±2.7	4.79±1.07	0.11±0.02	1.03±0.27	39	54	169
M18 KO+ 4a-PMA	34.0±2.9	7.42±4.03	0.07±0.02	0.65±0.34	33	59	163
WT+PMA	42.0±4.0	11.3±3.2	0.22±0.05	0.80±0.15	35	55	157
TeTx	28.7±2.1	3.78±0.87	0.06±0.01	0.23±0.07	40	55	144
BoNT-C1	27.8±2.2	4.13±1.22	0.06±0.01	0.14±0.04	30	65	142
Fixed	-	-	-	0.008±0.001	0	78	113
Beads	-	-	-	0.0050±0.0004	0	72	127

Table S.3. Mean square displacement analysis summary for LDCV axial (Z) movement. Data are mean ± SEM.

Phenotype	Average MSD fitting parameters				Diffusion type frequency		Total
	R_{cage}	$D_{in\ cage}$	D_{cage}	D_{free}	Cage	Free	
	nm	($\times10^{-4}$) $\mu m^2/s$	($\times10^{-5}$) $\mu m^2/s$		%		ves
WT	8.82±0.55	4.77±0.97	0.40±0.09	26.9±7.36	64	33	254
M18 KO	10.4±0.8	9.49+1.94	2.24±0.56	8.76±1.99	32	64	137
KO+M18-1	15.1±1.7	20.1±6.3	5.20±1.52	80.0±21.7	36	58	128
KO+ M18-1$^{D34N;M38V}$	11.0±1.1	10.8±2.9	2.07±0.46	72.8±14.5	44	48	178
WT+LatrA	8.81±0.62	9.09±2.99	1.01±0.21	26.2±8.21	54	44	115
M18 KO+ LatrA	10.1±0.7	7.88±2.21	1.92±0.53	13.0±6.4	50	35	122
M18 KO+ PMA	5.65±0.34	2.20±0.46	0.60±0.13	44.0±11.6	53	44	169
M18 KO+ 4a-PMA	8.72±0.80	5.97±1.36	1.35±0.35	20.2±7.7	47	48	163
WT+PMA	8.63±0.92	12.2±5.1	2.79±1.33	26.4±4.7	48	44	157
TeTx	16.2±0.7	33.1±8.7	2.05±0.40	48.1±15.4	81	18	144
BoNT-C1	13.5±0.7	11.6±2.8	1.39±0.40	16.4±4.4	67	32	142
Fixed	4.71±0.44	2.26±0.54	0.15±0.03	0.62±0.17	24	76	113
Beads	5.15±0.26	0.52±0.07	0.19±0.03	0.92±0.12	20	80	127

Table S.4. Kinetic parameters of the first-order stochastic tethers used in the random walk simulations of particle diffusion

Assigned color	k_{on}, s^{-1}	k_{off}, s^{-1}	Steady-state activation	τ_{active}, s	$\tau_{inactive}$, s	k_{on}/k_{off}
Purple	5	100	0.04762	0.01	0.2	0.05
Green	50	400	0.1111	0.0025	0.02	0.125
Yellow	5	20	0.2	0.05	0.2	0.25
Red	50	100	0.3333	0.01	0.02	0.5
Blue	5	10	0.3333	0.1	0.2	0.5
Black	0.5	1	0.3333	1	2	0.5

Supplementary Figures

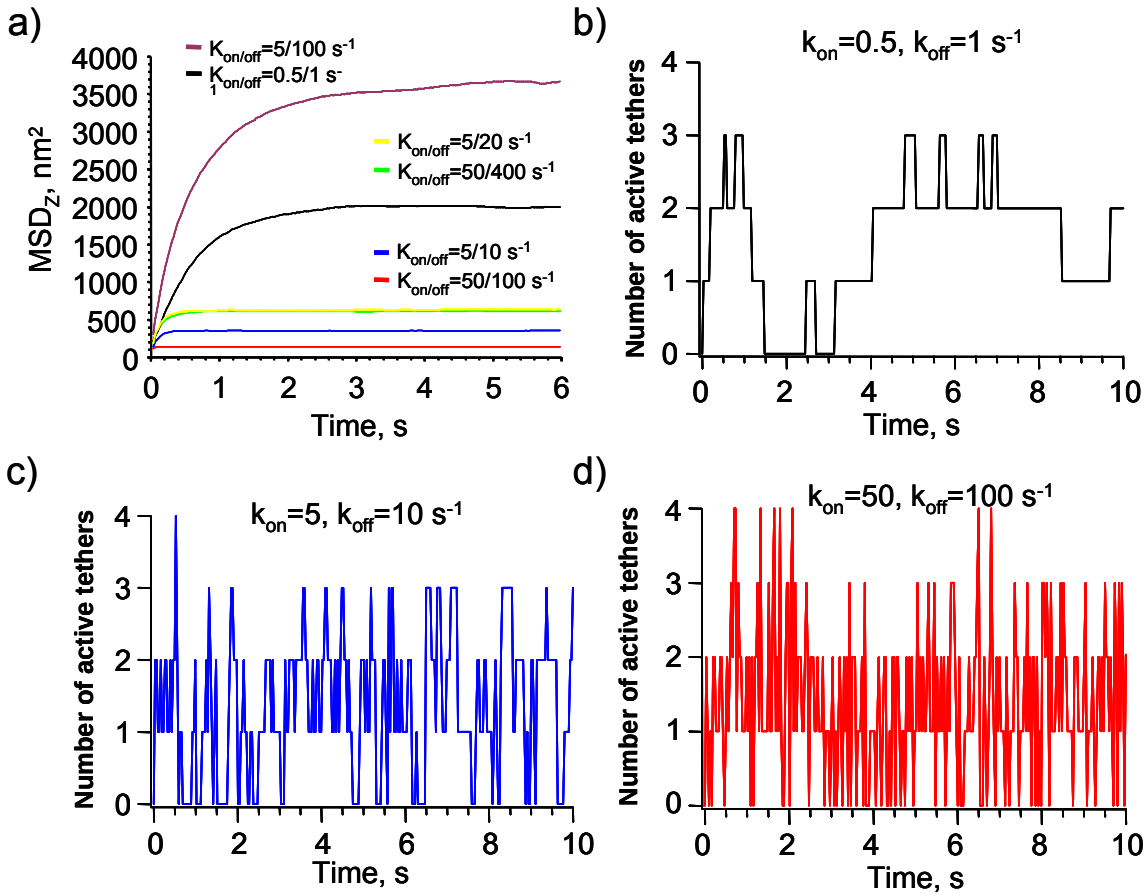

Fig. S.1. Simulation of the effective diffusion space restriction with stochastic tethers. (**a**) Mean square displacement from simulated Z-trajectories of particle movement in the space with stochastic tethers (N_{total}=4, ς=0.25) of different kinetics (color assignment is in accordance with the Suppl. Table S.3). (**b-d**) Samples of the four-tether ensemble activity during 10 s simulation time (33 ms sampling rate). Tethers fluctuations between the active and inactive states as well as the average lifetimes and state occupancy (Suppl. Table S.3) are governed by tether's kinetics: k_{on}=0.5, k_{off}=1 s^{-1} (b), k_{on}=5, k_{off}=10 s^{-1} (c), k_{on}=50, k_{off}=100 s^{-1} (d).

Appendix A

Dialog windows designed for controlling the new TIRFM setup under DaVis 6.2

A.1. Nikon TE2000 microscope control window

The dialog window (Fig. A.1) allows interactive control of the microscope functions.

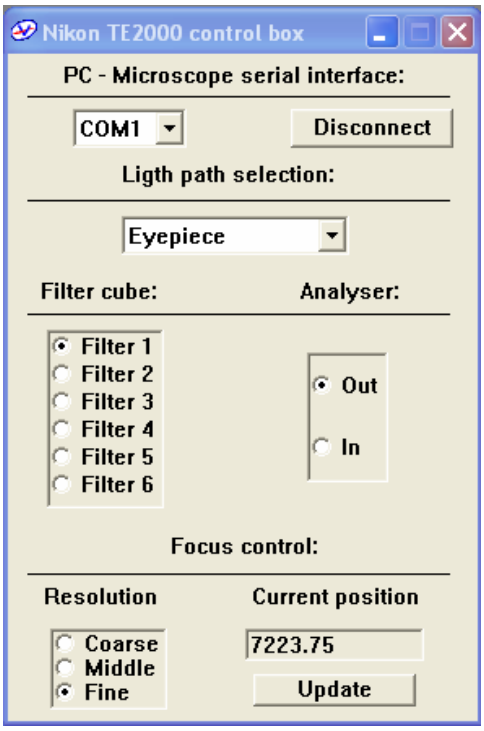

Fig. A.1. Dialog window controlling functions of the motorized inverted microscope Nikon TE2000.

• The control commands and feedback information from the microscope are sent/received through the standard RS232 serial port (COM port) which can be changed with the drop-down list.

• The button Connect/Disconnect establishes software connection between PC and microscope communication unit via selected serial port. Upon connection, the controls described below are set to default values. After DaVis 6.2 is started, the microscope is by default disconnected. The dialog window can be called from the 'iXon' menu.

• The drop-down list 'Light path selection' controls the light path selector of the microscope switching it to the desired ports: 100% observation port (eyepiece); 20/80% observation/right-side port; 100% bottom port; 20/80% observation/front port; 100% left-side port.

• The desired position of the filter cube can be chosen by the radio-button selection group, as well as the position of the polarizer in the detection pathway (analyzer) for DIC imaging.

• The resolution of the focus positioning with the focus control knob at the microscope can be changed with the radio-button group ‘Resolution’ to 100 (coarse), 50 or 25 (fine) μm per knob rotation. Position of the focus in absolute units (≈μm) can be read out from the microscope using the ‘Update’ button. Remote positioning of the focus using the PC dialog window is disabled due to the safety considerations.
• Successful completion of all the actions is feedback-controlled. Duration of the operations is variable and depends on the microscope.
• The dialog window and its related functions are programmed in the CL-file ‘nikonte2000_control.cl’.

A.2. Perfusion control window

The perfusion dialog window (Fig. A.2) controls the perfusion system built on the Warner Instruments six channel valve controller VC-6 and fast perfusion pipette stepper SF-77B.

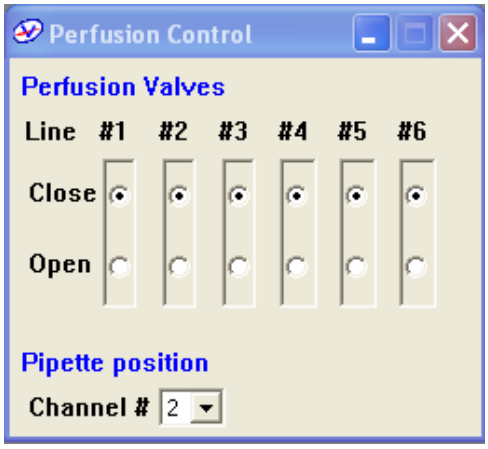

Fig. A.2. Dialog window controlling functions of the Warner Instruments perfusion system.

• The valves of the six channel perfusion system can be independently controlled in real time by the radio-button groups. The TTL control signals for the valves numbered from 1 to 6 are generated at the BNC output connectors A4, A5, A6, A7, B3, B4 of the connector box, respectively.
• The pipette position can be set with the drop-down list of positions numbered from 0 to 3. The SF-77B stepper is controlled via its digital input lines. The digital signal is ‘compiled’ out of the TTL signals from A1 (bit 0) and A2 (bit 1) BNC output connectors.
• The perfusion dialog window and its related functions are programmed in the CL-files ‘perfusion_control.cl’, ‘perfusion_warner_instr.cl’.

A.3. Illumination control window

The illumination dialog window (Fig. A.3) controls the light sources of the system: the AOTF driver for the selection of the required laser lines and their intensities, and the Polychrome IV epi-illumination device (monochromator).

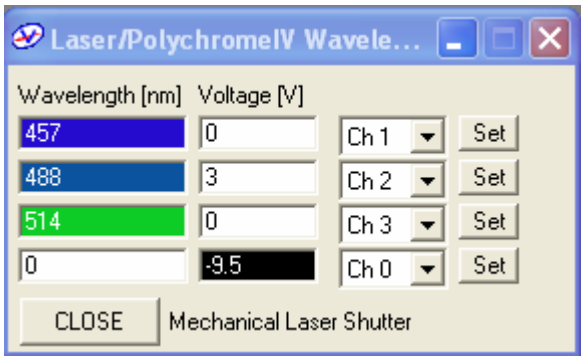

Fig. A.3. Dialog window controlling excitation light sources of the TIRFM setup.

• The pre-calibrated channels of the AOTF (457, 488, 514 nm) can be controlled with analog signals ranging from 0 (minimum) to 10V (maximum intensity). The control voltage required at any of the AOTF channels can be entered into the corresponding fields and set by pressing the 'Set' button or <Enter>. The voltage signals are generated by the I/O card installed at the PC and applied to the BNC output connectors DA1, DA2 and DA3 (for 457, 488 and 514 nm respectively).

• The Polychrome IV device (monochromator) can be controlled by directly typing desired wavelength in nm into the edit box. A new setting is accepted by pressing 'Set' button or <Enter>. Accepted values range from 340 to 680 nm, out-of-range values will correspond to the dark output of the monochromator. By default, the wavelength is set to the dark output ('0 nm'). Physically, the monochromator is controlled with analog voltage ranging from -10.0 to 10V through the analog control line connected to the BNC output DA0. The wavelength-to-voltage conversion is performed according to the look-up calibration table supplied by the manufacturer (Till Photonics GmbH).

• In addition to the AOTF, the laser excitation light (all wavelengths simultaneously) can be mechanically shuttered. The mechanical shutter is controlled by the button 'Close/Open' button, which drives TTL signals at the BNC connector A3.

• The illumination dialog window and its related functions are programmed in the CL-files 'dac_lw_control.cl', 'polychrome_iv.cl'.

A.4. Acquisition control window

The acquisition dialog window (Fig. A.4) controls the single image and live acquisition using the CCD camera. It allows setting the acquisition parameters of the camera, excitation light sources, and executing pre-programmed acquisition protocols.

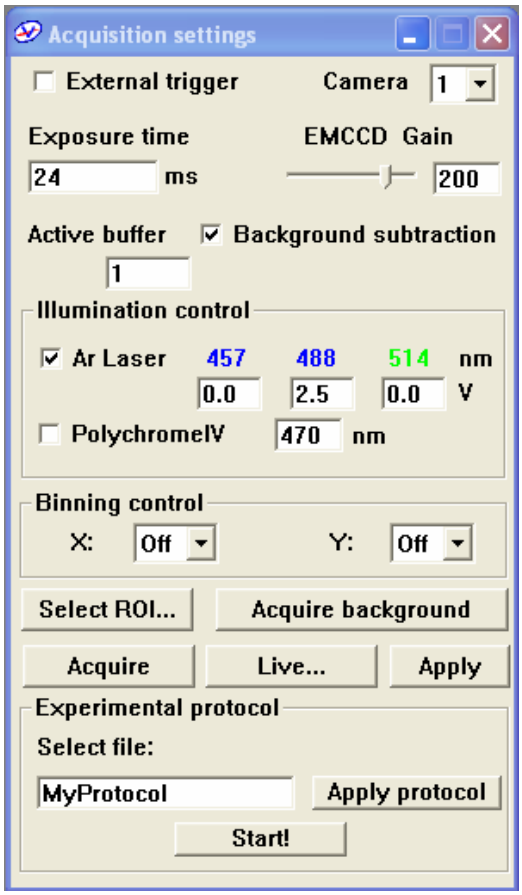

Fig. A.4. Dialog window controlling the acquisition parameters of the system.

• The dialog and its related functions can be extended to several CCD cameras (drop-down list). Currently, only one Andor i-Xon EM-CCD camera is installed under number 1. All the following settings will apply for the specified camera.

• Acquisition of single images (or images during live acquisition) can be triggered by external TTL signals. If the check-box 'External trigger' is set, the CCD camera will be triggered by the external signal. In the current configuration, the trigger signal is automatically generated by the PC at the BNC output A0 and used for camera triggering if the check-box is set. When the check-box is cleared, the acquisition timing is determined by the camera or programmed by the acquisition protocol.

• Exposure time in milliseconds can be set in the edit box 'Exposure time'. This controls camera exposure, while illumination is switched on and off before and after image readout. This and all the following entered settings are accepted by pressing 'Apply' button, or <Enter>, or automatically upon first acquisition.

• The electron multiplying gain factor (integer number between 1 and 255) of the EM-CCD can be set with the slider or directly in the edit box.
• The option 'Background subtraction' allows the automatic subtraction of a constant image representing average dark noise. Such a background image can be taken by pressing 'Acquire background' button and is calculated as the average over 10 snapshots. These snapshots are acquired at the current settings. Changing of any camera parameters will require a new background image to be taken first before the automatic background subtraction can be activated.
• 'Active buffer' determines the image buffer number (1-999) where the acquired image will be stored upon 'Acquire' action. This number is automatically increased after every next single acquisition, since otherwise the buffer will be overwritten.
• The 'Illumination control' box allows setting parameters of excitation light sources during single or live image acquisition. Check boxes activate AOTF (laser light modulator) and/or monochromator during acquisition, with parameters described above in section 3 of this Appendix.
• The 'Binning control' box allows controlling the camera binning. Binning is independent for X and Y, and available binning factors are to the power of two.
• The button 'Select ROI…' leads to the selection of a rectangular active region of interest on the CCD chip to be read out during acquisition. Alternatively, the whole CCD frame can be selected. Binning can be further applied to the selected ROI.
• The 'Acquire' button applies all the set parameters and initiates a single image acquisition, with the resulting image stored in the active buffer.
• The 'Live…' button applies all the settings and starts continuous image grabbing. Acquired images are NOT stored in this mode.
• 'Apply' button accepts all the settings for future acquisitions.
• The 'Experimental protocol' box allows loading the *.seq files with the command sequences for programmed image acquisition and periphery control. The syntax of sequence files is described in Appendix B. The file name of *.seq file, located in the \Davis62\Experiment folder, can be entered into the edit box. The button 'Apply protocol' leads to loading and translation of the command sequence from the specified file. The button 'Start!' will execute the loaded acquisition program. The resulting image series will be stored on the hard drive at the location, specified after program completion. Along with the image stack, the protocol file with the employed acquisition parameters, such as timing information for an acquired image, and the used command sequence, will be stored.
• The acquisition dialog window and its related functions are programmed in the CL-file 'setacq_parameters.cl'.

Appendix B

Programming image acquisition sequences on the new TIRFM setup

B.1. General syntax of the command sequence files (*.seq)

The set of commands which can be used in *.seq files was designed for programming complicated imaging protocols involving the timed control over different peripheral devices. Sequence files (*.seq) are the text files, that can be composed with any text editor, and should possess the following structure (Fig. B.1).

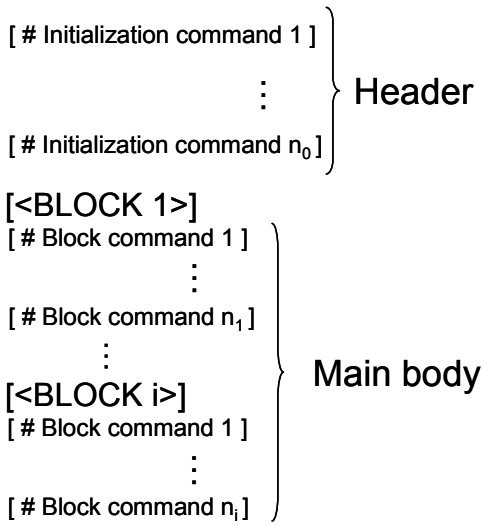

Fig. B.1. Structure schematic of the acquisition sequence controlling program.

The header of the program can contain commands that exert control over the whole program or commands to be executed before and after image acquisition. The main body of the program consists of a sequence of blocks to be executed. Commands or settings from the header retain their validity until the first appearance in a block during execution.

The blocks directly control image acquisition and can contain commands on acquisition timing, excitation light sources, and peripheral devices. However, the acquisition parameters of the CCD camera, set with the 'Acquisition control' window (Appendix A), will apply through the whole program and can not be temporarily modified within the blocks.

All commands have the common syntax (B.1).

$$\#\ \langle\text{command keyword}\rangle = \langle\text{string operand}\rangle \qquad \text{(B.1)}$$

The hash character '#' should be followed by one of the appropriate command keywords. The string operand follows after the equality sign '=' and contains the information necessary for command execution. The commands can be placed in arbitrary order in both the program header and blocks. In case of repeated commands, the latest

one will be executed. The syntax is not case-sensitive and spaces are optional except for the body of string operands. Unknown command keywords are ignored.

B.2. Available commands for programming acquisition sequences

The commands that can be used in the program header and/or blocks are listed below in the Table B.1. Their applicability, the format of operands and their actions are also described in the table. Unless otherwise specified, the commands can be used both in header and blocks.

Table B.1.

Command keyword	Operand	Description
Name (header only)	[Any string]	A symbolic name for command sequence. Example: 'My Sequence'.
BlockSequence (header only)	[[k;]..[|[l,][m]|n;]..] k, l, m – block numbers; n – number of repetitions for the loop body |l;m;|	Sequence of the blocks execution. Block's numbers should be listed in required order with ';' separator. These blocks will be consecutively executed. Loops of blocks are possible by listing a sequence of blocks (loop body) between symbols '||'. Number of loop repetitions should follow the second '|' symbol. Example: '1;|1,2,3|2;3;' has one loop and will correspond to the block sequence "1-1-2-3-1-2-3-3" when executed.
StoreStack (header only)	'TRUE' or 'FALSE'	If TRUE, the image stack will be automatically stored on the hard drive after acquisition at prompted location. If FALSE, the image stack will reside in RAM.
StoreFormat (header only)	'*.tif', '*.bmp', '*.jpg', '*.imx', '*.img', '*.b16'	Choosing the image file format for storing the acquired image stack.
Frames (blocks only)	<# of frames>	Number of image frames to acquire in the block.
Interval (blocks only)	<time in ms>	Time interval between consecutive image frames. Does NOT include the exposure time.
WaitAfter (blocks only)	<time in ms>	Time to wait before continuing after the block is over.
StartOUT_TTL (blocks only)	'A0'-'A7', 'B0'- 'B7', 'C0'-'C7'	Sets the output TTL trigger to 'high' when the block execution starts and to 'low' when it ends. Operand specifies the name of the output BNC connector for this signal.

Table B.1. (continued)

SyncOUT_TTL (blocks only)	'A0'- 'A7', 'B0'- 'B7', 'C0'-'C7'	Sets the output TTL trigger to 'high' during every image acquisition within the block. Operand specifies the name of the output BNC connector to use for this signal.
StartIN_Trigger (blocks only)	'1', '2', '3' or '4'	If command is used, the program will start the block execution upon the 'high' state of the input TTL trigger signal. Background image is taken before waiting for the trigger. Operand value specifies the bit of input port C (BNC connector IN1, IN2...) where the trigger signal is awaited.
LiveUpdate	'TRUE' or 'FALSE'	If TRUE, the acquired images will be immediately displayed. When FALSE, the performance is optimized for speed.
TakeBackground	'TRUE' or 'FALSE'	If TRUE, the new background image will be taken immediately before the acquisition starts within the block.
LaserActive (header only)	'TRUE' or 'FALSE'	Determines, whether laser illumination will be used through the whole acquisition program.
PolychromeActive (header only)	'TRUE' or 'FALSE'	Determines, whether illumination with Polychrome IV device (monochromator) will be used through the whole acquisition program.
LaserLines	<V_{457}/V_{488}/V_{514}>	Sets the voltages controlling the AOTF channels for respective laser lines: 457, 488, 514 nm. Example: '0.0/2.5/0.0' – 2.5V will be applied to the channel controlling 488 nm line.
Polychrome	<wavelength, nm>	Sets the desired wavelength of Polychrome IV: 340-680 nm or other values for the dark output.
LaserShutter (blocks only)	'TRUE' or 'FALSE'	If TRUE, the laser light will turn off between CCD exposures, otherwise illumination will be continuous during the block.
PolychromeShutter (blocks only)	'TRUE' or 'FALSE'	If TRUE, the monochromator light will turn off between CCD exposures, otherwise illumination will be continuous during the block.
LaserMechShutter	'OPEN' or 'CLOSE'	Controls the mechanical laser shutter (all laser lines).
Valves	<? ? ? ? ? ?> ?='0' or '1'	Controls the six perfusion valves. State of the valve is binary: '1'=open, '0'= close. Example: '0 0 1 0 0 0' – only valve #3 is open.

Table B.1. (continued)

Pipette	<pipette position>	Sets the perfusion pipette to desired position (from 0 to 3).
NikonFilterCube	<# of filter cube>	Sets the desired fluorescence filter cube at Nikon TE2000 microscope.
NikonLightPath	'EYE', 'RIGHT', 'BOTTOM', 'FRONT', 'LEFT'	Switches the detection light path of the Nikon TE2000 microscope to the desired port.
NikonAnalyser	'IN' or 'OUT'	Controls the DIC analyzer position of Nikon TE2000 microscope.

B.3. An example of a *.seq acquisition program

```
#Name = Experiment1
#NikonFilterCube = 1
#NikonLighPath = LEFT
#NikonAnalyser = OUT
#TakeBackground = TRUE
#LiveUpdate = TRUE
#Valves = 0 0 0 0 0 0
#Pipette = 2
#LaserActive = TRUE
#LaserLines = 0.0/0.0/0.0
#PolychromeActive = TRUE
#Polychrome = 0
#BlockSequence = 1;|1,2|2;3
#StoreStack = TRUE
#StoreFormat = *.tif
#LaserMechShutter = OPEN

BLOCK 1
#StartOUT_TTL = B1
#Valves = 0 1 0 0 0 0
#Pipette = 2
#LaserLines = 0.0/3.0/0.0
#LaserShutter = TRUE
#Interval = 200
#Frames = 100
#WaitAfter= 0

BLOCK 2
#SyncOUT_TTL =B1
#Valves = 1 0 0 0 0 0
#Pipette = 1
#LaserLines = 0.0/3.0/0.0
#LaserShutter = TRUE
#Interval = 0
#Frames = 200
#WaitAfter=0

BLOCK 3
#NikonFilterCube = 2
#TakeBackground = TRUE
#StartIN_Trigger = 1
#LiveUpdate = FALSE
```

```
#Polychrome = 430
#PolychromeShutter = FALSE
#Valves = 0 1 0 0 0 0
#Pipette = 2
#LaserLines = 0.0/0.0/0.0
#Interval = 10
#Frames = 100
```

B.4. Format of the output image stack and protocol file

When a sequence *.seq file is used for programmed image stack acquisition, the resulting image stack can be automatically stored on the PC's hard drive if the 'StoreStack' command was used in the header of the program with 'TRUE' operand value. The location and filename will be prompted to be specified after the acquisition is complete or user-interrupted. The image stack will be stored as a set of individual image files in the newly created folder at the specified location. The name of the folder is formed as the specified name with the added suffix '_img'. The image filenames will have the specified name with the numbered four-digit suffix starting with 0: '_0000', '_0001' and so on. Filename extensions will correspond to the image file type determined by the 'StoreFormat' command. The text protocol file will be stored at the same specified location as the image stack folder and have the specified name and *.sti extension.

For example, if the specified location to store the acquired data of 100 images in TIFF format is 'C:\Data\', and the specified name is 'Experiment1', the stored data will have the following structure (Fig. B.2).

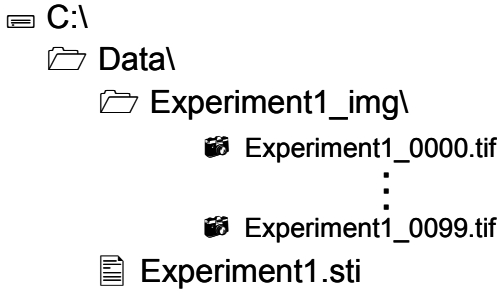

Fig. B.2. Structure of the data stored by the acquisition sequence program.

The *.sti protocol file is a simple text file where the employed camera settings, the image stack time stamps, and the used sequence program are documented. The header of the file contains 8 lines. The first line has information on the sequence program name (set with the 'Name' command) and date and time of the sequence program execution. After an empty line, there are 6 lines stored with the following camera parameters: 1) CCD camera number; 2) exposure time; 3) EMCCD gain factor; 4) pixel coordinates of the rectangular ROI on the CCD chip, used for image readout; 5) binning factors for X and Y; 6) background subtraction mode. The next line is empty, followed by the info-string 'Time marks of acquired images:'. If the acquisition program was interrupted by the user, this line will have corresponding notification. The number of following lines is

determined by the number of stored images. Every line will have a number of an image in the stack (starting from 0), and date and time stamps of an image in "DD.MM.YY hh:mm:ss.ms" text format. At the end of the *.sti file, the copy of the *.seq program used is included for complete documentation.

A truncated example of such a protocol file (experiment1.sti) is included below.

```
----- File Starts
Protocol program 'Experiment1' executed at: Fri Nov 26, 2004 20:53:01

Camera number: 1
Exposure time used: 100 ms
Camera gain: 70
ROI on the CCD chip: (0,0) to (127,127)
Binning along X and Y: 1 by 1
Background subtraction: enabled

Time marks of acquired images:
0: 26.11.04 20:53:02.390
1: 26.11.04 20:53:03.515
2: 26.11.04 20:53:04.640
3: 26.11.04 20:53:05.765
4: 26.11.04 20:53:06.875
// 440 time stamps were cut
446: 26.11.04 21:01:22.750
447: 26.11.04 21:01:23.875
448: 26.11.04 21:01:25.000
449: 26.11.04 21:01:26.109
450: 26.11.04 21:01:27.234

Protocol program used:

#Name=Experiment1
#LiveUpdate=TRUE
----- Further sequence program listing truncated
```

Acknowledgements

I would like to thank my supervisor, Dr. Jürgen Klingauf, for his great patience, constructive criticism, helpfulness and support in critical situations, which all made this work possible. I would also like to thank the head of the department Prof. Dr. Erwin Neher and the members of my PhD thesis committee Prof. Dr. Tobias Moser and Prof. Dr. Zippelius for their support and critical suggestions during development of the project.

Many-many thanks to all the former and current members of our MOST group, who made my period of life in the lab inimitable and unforgettable. I thank Drs. Dinah Loerke for her continuous calming optimism, and Edward Lemke for his supercritical realism, enthusiasm and endless source of entertainment. Special thanks for their volunteered critical proofreading of this manuscript. Dr. Pieter Vanden Berghe was always helpful and ready to discuss scientific and other important problems, always reaching the state of mutual understanding. I thank Drs. Maria Krikounova and Veronica Müller for being a source of moral support and a spirit of contradiction, and the new colleagues, Drs. Natalya Glyvuk and Yaroslav Tsytsyura for their kindness. I thank Martin Wienisch since together we could sustain and manage difficulties of the last period, also for being inexhaustible source of charm, music, and staying still a hopeless romantic. I am grateful to my partner in fly-project Dr. Amitabha Majumdar, and master student Anna Botvinnik for having great time in the lab and outside. I thank a lab-rotation student Tsaiwen Chen who was that kind of student that makes the teachers grow. I also thank Michael Pilot for expert technical assistance by the first call.

I am thankful to Dr. Ralf Nehring for teaching and supervising molecular cloning despite having tons of other problems, Dirk Reuter for urgent production of viral particles, and Frank Köhne who could rapidly build electronic gadgets for the new TIRFM setup. Many thanks to Dr. Samuel Young, Jr., who taught and supervised my cloning and production of adenoviruses, and besides that, for creating unique working atmosphere in the lab. I thank Dr. Ruud Toonen, Prof. Dr. Matthijs Verhage and Dr. Jakob Sorensen for fruitful stimulating discussions and coordination of our collaboration project. Many thanks to the members of Dr. Sorensen's group, especially Dr. Attila Gulyás-Kovács for teaching me chromaffin tricks and moral support, Dr. Jean-Sebastian Schonn for discussions and fun and Ira Milosevic for the NPY-Venus construct. I also thank Dr. Darina Khimich and Dr. Tobias Moser with whom we started inner-hair cell TIRFM project.

I thank all the members of GRK 723, and the head, Prof. Dr. Detlev Schild, for organizing the program of seminars and meetings, being of significant educational value, and support of this work with the fellowship from Deutsche Forschungsgemeinschaft. Many thanks to the coordination team of the Neurosciences Program for perfect organization of the study process and other activities, providing great opportunities for the international students. Participation in the Program made staying in Göttingen and all my work here in principle possible.

And, I am endlessly grateful for everything to my parents Galina and Olexander Kochubey, who always supported my intention to study and interest in science, and to my wife Natalya Korogod, providing the most important and essential psychological support which kept me going.

References

Allersma MW, Wang L, Axelrod D, Holz RW (2004) Visualization of regulated exocytosis with a granule-membrane probe using total internal reflection microscopy. Mol Biol Cell 15:4658-4668.

Aravanis AM, Pyle JL, Tsien RW (2003) Single synaptic vesicles fusing transiently and successively without loss of identity. Nature 423:643-647.

Ashery U, Betz A, Xu T, Brose N, Rettig J (1999) An efficient method for infection of adrenal chromaffin cells using the Semliki Forest virus gene expression system. Eur J Cell Biol 78:525-532.

Ashery U, Varoqueaux F, Voets T, Betz A, Thakur P, Koch H, Neher E, Brose N, Rettig J (2000) Munc13-1 acts as a priming factor for large dense-core vesicles in bovine chromaffin cells. Embo J 19:3586-3596.

Axelrod D, Thompson NL, Burghardt TP (1983) Total internal inflection fluorescent microscopy. J Microsc 129 Pt 1:19-28.

Bader MF, Holz RW, Kumakura K, Vitale N (2002) Exocytosis: the chromaffin cell as a model system. Ann N Y Acad Sci 971:178-183.

Barclay JW, Craig TJ, Fisher RJ, Ciufo LF, Evans GJ, Morgan A, Burgoyne RD (2003) Phosphorylation of Munc18 by protein kinase C regulates the kinetics of exocytosis. J Biol Chem 278:10538-10545.

Bastiaensen E, De Block J, De Potter WP (1988) Neuropeptide Y is localized together with enkephalins in adrenergic granules of bovine adrenal medulla. Neuroscience 25:679-686.

Bennett MK, Calakos N, Scheller RH (1992) Syntaxin: a synaptic protein implicated in docking of synaptic vesicles at presynaptic active zones. Science 257:255-259.

Betz WJ, Angleson JK (1998) The synaptic vesicle cycle. Annu Rev Physiol 60:347-363.

Beutner D, Voets T, Neher E, Moser T (2001) Calcium dependence of exocytosis and endocytosis at the cochlear inner hair cell afferent synapse. Neuron 29:681-690.

Bhaskar K, Shareef MM, Sharma VM, Shetty AP, Ramamohan Y, Pant HC, Raju TR, Shetty KT (2004) Co-purification and localization of Munc18-1 (p67) and Cdk5 with neuronal cytoskeletal proteins. Neurochem Int 44:35-44.

Biederer T, Sudhof TC (2000) Mints as adaptors. Direct binding to neurexins and recruitment of munc18. J Biol Chem 275:39803-39806.

Biederer T, Sudhof TC (2001) CASK and protein 4.1 support F-actin nucleation on neurexins. J Biol Chem 276:47869-47876.

Blumberg S, Gajraj A, Pennington MW, Meiners JC (2005) Three-dimensional characterization of tethered microspheres by total internal reflection fluorescence microscopy. Biophys J 89:1272-1281.

Borisovska M, Zhao Y, Tsytsyura Y, Glyvuk N, Takamori S, Matti U, Rettig J, Sudhof T, Bruns D (2005) v-SNAREs control exocytosis of vesicles from priming to fusion. Embo J 24:2114-2126.

Borst JG, Helmchen F, Sakmann B (1995) Pre- and postsynaptic whole-cell recordings in the medial nucleus of the trapezoid body of the rat. J Physiol 489 (Pt 3):825-840.

Brandt BL, Hagiwara S, Kidokoro Y, Miyazaki S (1976) Action potentials in the rat chromaffin cell and effects of acetylcholine. J Physiol 263:417-439.

Broadie K, Prokop A, Bellen HJ, O'Kane CJ, Schulze KL, Sweeney ST (1995) Syntaxin and synaptobrevin function downstream of vesicle docking in Drosophila. Neuron 15:663-673.

Burghardt TP, Thompson NL (1984) Effect of planar dielectric interfaces on fluorescence emission and detection. Evanescent excitation with high-aperture collection. Biophys J 46:729-737.

Burgoyne RD, Fisher RJ, Graham ME, Haynes LP, Morgan A (2001) Control of membrane fusion dynamics during regulated exocytosis. Biochem Soc Trans 29:467-472.

Carr CM, Grote E, Munson M, Hughson FM, Novick PJ (1999) Sec1p binds to SNARE complexes and concentrates at sites of secretion. J Cell Biol 146:333-344.

Catterall WA (1999) Interactions of presynaptic Ca2+ channels and snare proteins in neurotransmitter release. Ann N Y Acad Sci 868:144-159.

Ceccarelli B, Hurlbut WP, Mauro A (1972) Depletion of vesicles from frog neuromuscular junctions by prolonged tetanic stimulation. J Cell Biol 54:30-38.

Chan SA, Polo-Parada L, Smith C (2005) Action potential stimulation reveals an increased role for P/Q-calcium channel-dependent exocytosis in mouse adrenal tissue slices. Arch Biochem Biophys 435:65-73.

Chen X, Tang J, Sudhof TC, Rizo J (2005) Are neuronal SNARE proteins Ca2+ sensors? J Mol Biol 347:145-158.

Chen YA, Scales SJ, Scheller RH (2001) Sequential SNARE assembly underlies priming and triggering of exocytosis. Neuron 30:161-170.

Chieregatti E, Witkin JW, Baldini G (2002) SNAP-25 and synaptotagmin 1 function in Ca2+-dependent reversible docking of granules to the plasma membrane. Traffic 3:496-511.

Chow RH, von Ruden L, Neher E (1992) Delay in vesicle fusion revealed by electrochemical monitoring of single secretory events in adrenal chromaffin cells. Nature 356:60-63.

Ciufo LF, Barclay JW, Burgoyne RD, Morgan A (2004) Munc18-1 Regulates Early and Late Stages of Exocytosis via Syntaxin-independent Protein Interactions. Mol Biol Cell.

Clay JR, DeFelice LJ (1983) Relationship between membrane excitability and single channel open-close kinetics. Biophys J 42:151-157.

Colquhoun D, Hawkes AG (1995) The principles of the stochastic interpretation of ion-channel mechanisms. In: Single-channel recording, 2nd Edition (Neher E, Sakmann B, eds), pp 397-482. New York: Plenum Press.

Colquhoun D, Sigworth FJ (1995) Fitting and statistical analysis of single-channel records. In: Single-channel recording, 2nd Edition (Neher E, Sakmann B, eds), pp 483-588. New York: Plenum Press.

Deak F, Schoch S, Liu X, Sudhof TC, Kavalali ET (2004) Synaptobrevin is essential for fast synaptic-vesicle endocytosis. Nat Cell Biol 6:1102-1108.

Del Castillo J, Katz B (1954) Quantal components of the end-plate potential. J Physiol 124:560-573.

Dulubova I, Sugita S, Hill S, Hosaka M, Fernandez I, Sudhof TC, Rizo J (1999) A conformational switch in syntaxin during exocytosis: role of munc18. Embo J 18:4372-4382.

Duncan RR, Greaves J, Wiegand UK, Matskevich I, Bodammer G, Apps DK, Shipston MJ, Chow RH (2003) Functional and spatial segregation of secretory vesicle pools according to vesicle age. Nature 422:176-180.

El Meskini R, Jin L, Marx R, Bruzzaniti A, Lee J, Emeson R, Mains R (2001) A signal sequence is sufficient for green fluorescent protein to be routed to regulated secretory granules. Endocrinology 142:864-873.

Eliasson L, Renstrom E, Ding WG, Proks P, Rorsman P (1997) Rapid ATP-dependent priming of secretory granules precedes Ca(2+)-induced exocytosis in mouse pancreatic B-cells. J Physiol 503 (Pt 2):399-412.

Fasshauer D, Sutton RB, Brunger AT, Jahn R (1998) Conserved structural features of the synaptic fusion complex: SNARE proteins reclassified as Q- and R-SNAREs. Proc Natl Acad Sci U S A 95:15781-15786.

Fernandez-Chacon R, Konigstorfer A, Gerber SH, Garcia J, Matos MF, Stevens CF, Brose N, Rizo J, Rosenmund C, Sudhof TC (2001) Synaptotagmin I functions as a calcium regulator of release probability. Nature 410:41-49.

Fisher RJ, Pevsner J, Burgoyne RD (2001) Control of fusion pore dynamics during exocytosis by Munc18. Science 291:875-878.

Fix M, Melia TJ, Jaiswal JK, Rappoport JZ, You D, Sollner TH, Rothman JE, Simon SM (2004) Imaging single membrane fusion events mediated by SNARE proteins. Proc Natl Acad Sci U S A 101:7311-7316.

Fletcher AI, Shuang R, Giovannucci DR, Zhang L, Bittner MA, Stuenkel EL (1999) Regulation of exocytosis by cyclin-dependent kinase 5 via phosphorylation of Munc18. J Biol Chem 274:4027-4035.

Foran P, Lawrence GW, Shone CC, Foster KA, Dolly JO (1996) Botulinum neurotoxin C1 cleaves both syntaxin and SNAP-25 in intact and permeabilized chromaffin cells: correlation with its blockade of catecholamine release. Biochemistry 35:2630-2636.

Fujita Y, Sasaki T, Fukui K, Kotani H, Kimura T, Hata Y, Sudhof TC, Scheller RH, Takai Y (1996) Phosphorylation of Munc-18/n-Sec1/rbSec1 by protein kinase C: its implication in regulating the interaction of Munc-18/n-Sec1/rbSec1 with syntaxin. J Biol Chem 271:7265-7268.

Fukuda M, Moreira JE, Liu V, Sugimori M, Mikoshiba K, Llinas RR (2000) Role of the conserved WHXL motif in the C terminus of synaptotagmin in synaptic vesicle docking. Proc Natl Acad Sci U S A 97:14715-14719.

Gallwitz D, Jahn R (2003) The riddle of the Sec1/Munc-18 proteins - new twists added to their interactions with SNAREs. Trends Biochem Sci 28:113-116.

Gandhi SP, Stevens CF (2003) Three modes of synaptic vesicular recycling revealed by single-vesicle imaging. Nature 423:607-613.

Garcia EP, Gatti E, Butler M, Burton J, De Camilli P (1994) A rat brain Sec1 homologue related to Rop and UNC18 interacts with syntaxin. Proc Natl Acad Sci U S A 91:2003-2007.

Gengyo-Ando K, Kamiya Y, Yamakawa A, Kodaira K, Nishiwaki K, Miwa J, Hori I, Hosono R (1993) The C. elegans unc-18 gene encodes a protein expressed in motor neurons. Neuron 11:703-711.

Geppert M, Goda Y, Hammer RE, Li C, Rosahl TW, Stevens CF, Sudhof TC (1994) Synaptotagmin I: a major Ca2+ sensor for transmitter release at a central synapse. Cell 79:717-727.

Gillis KD, Mossner R, Neher E (1996) Protein kinase C enhances exocytosis from chromaffin cells by increasing the size of the readily releasable pool of secretory granules. Neuron 16:1209-1220.

Gladycheva SE, Ho CS, Lee YY, Stuenkel EL (2004) Regulation of syntaxin1A-munc18 complex for SNARE pairing in HEK293 cells. J Physiol 558:857-871.

Goda Y, Stevens CF (1994) Two components of transmitter release at a central synapse. Proc Natl Acad Sci U S A 91:12942-12946.

Gorgas K, Bock P (1976) Morphology and histochemistry of the adrenal medulla. I. Various types of primary catecholamine-storing cells in the mouse adrenal medulla. Histochemistry 50:17-31.

Grabner CP, Price SD, Lysakowski A, Fox AP (2005) Mouse chromaffin cells have two populations of dense core vesicles. J Neurophysiol 94:2093-2104.

Gulyás-Kovács A (2005) Munc18 function in large dense-core vesicle exocytosis. PhD Thesis. In: Department of Membrane Biophysics, Max-Planck Institute for biophysical chemistry, pp 87 p. Goettingen: Georg-August University, SUB Online.

Hafez I, Kisler K, Berberian K, Dernick G, Valero V, Yong MG, Craighead HG, Lindau M (2005) Electrochemical imaging of fusion pore openings by electrochemical detector arrays. Proc Natl Acad Sci U S A.

Halachmi N, Lev Z (1996) The Sec1 family: a novel family of proteins involved in synaptic transmission and general secretion. J Neurochem 66:889-897.

Han X, Wang CT, Bai J, Chapman ER, Jackson MB (2004) Transmembrane segments of syntaxin line the fusion pore of Ca2+-triggered exocytosis. Science 304:289-292.

Harlow M, Ress D, Koster A, Marshall RM, Schwarz M, McMahan UJ (1998) Dissection of active zones at the neuromuscular junction by EM tomography. J Physiol Paris 92:75-78.

Harrison SD, Broadie K, van de Goor J, Rubin GM (1994) Mutations in the Drosophila Rop gene suggest a function in general secretion and synaptic transmission. Neuron 13:555-566.

Hata Y, Sudhof TC (1995) A novel ubiquitous form of Munc-18 interacts with multiple syntaxins. Use of the yeast two-hybrid system to study interactions between proteins involved in membrane traffic. J Biol Chem 270:13022-13028.

Hata Y, Slaughter CA, Sudhof TC (1993) Synaptic vesicle fusion complex contains unc-18 homologue bound to syntaxin. Nature 366:347-351.

Hecht E (2002) Optics, 4th Edition. Reading, Mass.: Addison-Wesley.

Heuser JE, Reese TS (1973) Evidence for recycling of synaptic vesicle membrane during transmitter release at the frog neuromuscular junction. J Cell Biol 57:315-344.

Heuser JE, Reese TS, Dennis MJ, Jan Y, Jan L, Evans L (1979) Synaptic vesicle exocytosis captured by quick freezing and correlated with quantal transmitter release. J Cell Biol 81:275-300.

Hexum TD, Majane EA, Russett LR, Yang HY (1987) Neuropeptide Y release from the adrenal medulla after cholinergic receptor stimulation. J Pharmacol Exp Ther 243:927-930.

Hiesinger PR, Fayyazuddin A, Mehta SQ, Rosenmund T, Schulze KL, Zhai RG, Verstreken P, Cao Y, Zhou Y, Kunz J, Bellen HJ (2005) The v-ATPase V0 subunit a1 is required for a late step in synaptic vesicle exocytosis in Drosophila. Cell 121:607-620.

Hill K, Li Y, Bennett M, McKay M, Zhu X, Shern J, Torre E, Lah JJ, Levey AI, Kahn RA (2003) Munc18 interacting proteins: ADP-ribosylation factor-dependent coat proteins that regulate the traffic of beta-Alzheimer's precursor protein. J Biol Chem 278:36032-36040.

Hsu SC, Hazuka CD, Foletti DL, Scheller RH (1999) Targeting vesicles to specific sites on the plasma membrane: the role of the sec6/8 complex. Trends Cell Biol 9:150-153.

Hunt JM, Bommert K, Charlton MP, Kistner A, Habermann E, Augustine GJ, Betz H (1994) A post-docking role for synaptobrevin in synaptic vesicle fusion. Neuron 12:1269-1279.

Jahn R (2004) Principles of exocytosis and membrane fusion. Ann N Y Acad Sci 1014:170-178.

Jahn R, Lang T, Sudhof TC (2003) Membrane fusion. Cell 112:519-533.

Jockusch WJ, Praefcke GJ, McMahon HT, Lagnado L (2005) Clathrin-dependent and clathrin-independent retrieval of synaptic vesicles in retinal bipolar cells. Neuron 46:869-878.

Johns LM, Levitan ES, Shelden EA, Holz RW, Axelrod D (2001) Restriction of secretory granule motion near the plasma membrane of chromaffin cells. J Cell Biol 153:177-190.

Katz B, Miledi R (1965) The Effect Of Calcium On Acetylcholine Release From Motor Nerve Terminals. Proc R Soc Lond B Biol Sci 161:496-503.

Kawasaki F, Mattiuz AM, Ordway RW (1998) Synaptic physiology and ultrastructure in comatose mutants define an in vivo role for NSF in neurotransmitter release. J Neurosci 18:10241-10249.

Klingauf J, Neher E (1997) Modeling buffered Ca2+ diffusion near the membrane: implications for secretion in neuroendocrine cells. Biophys J 72:674-690.

Klingauf J, Kavalali ET, Tsien RW (1998) Kinetics and regulation of fast endocytosis at hippocampal synapses. Nature 394:581-585.

Kobayashi S (1977) Adrenal medulla: chromaffin cells as paraneurons. Arch Histol Jpn 40 Suppl:61-79.

Kobayashi S, Coupland RE (1993) Morphological aspects of chromaffin tissue: the differential fixation of adrenaline and noradrenaline. J Anat 183 (Pt 2):223-235.

Koenig JH, Ikeda K (1989) Disappearance and reformation of synaptic vesicle membrane upon transmitter release observed under reversible blockage of membrane retrieval. J Neurosci 9:3844-3860.

Koenig JH, Ikeda K (1996) Synaptic vesicles have two distinct recycling pathways. J Cell Biol 135:797-808.

Korteweg N, Maia AS, Thompson B, Roubos EW, Burbach JP, Verhage M (2005) The role of Munc18-1 in docking and exocytosis of peptide hormone vesicles in the anterior pituitary. Biol Cell 97:445-455.

Koval LM, Yavorskaya EN, Lukyanetz EA (2001) Electron microscopic evidence for multiple types of secretory vesicles in bovine chromaffin cells. Gen Comp Endocrinol 121:261-277.

Kuromi H, Kidokoro Y (1998) Two distinct pools of synaptic vesicles in single presynaptic boutons in a temperature-sensitive Drosophila mutant, shibire. Neuron 20:917-925.

Lang T, Bruns D, Wenzel D, Riedel D, Holroyd P, Thiele C, Jahn R (2001) SNAREs are concentrated in cholesterol-dependent clusters that define docking and fusion sites for exocytosis. Embo J 20:2202-2213.

Lang T, Wacker I, Steyer J, Kaether C, Wunderlich I, Soldati T, Gerdes HH, Almers W (1997) Ca2+-triggered peptide secretion in single cells imaged with green fluorescent protein and evanescent-wave microscopy. Neuron 18:857-863.

Lauterborn W, Kurz T (2003) Coherent optics: fundamentals and applications, 2nd Edition. Berlin; New York: Springer.

Lenzi D, Crum J, Ellisman MH, Roberts WM (2002) Depolarization redistributes synaptic membrane and creates a gradient of vesicles on the synaptic body at a ribbon synapse. Neuron 36:649-659.

Li D, Xiong J, Qu A, Xu T (2004) Three-dimensional tracking of single secretory granules in live PC12 cells. Biophys J 87:1991-2001.

Li L, Chin LS (2003) The molecular machinery of synaptic vesicle exocytosis. Cell Mol Life Sci 60:942-960.

Li Q, Lau A, Morris TJ, Guo L, Fordyce CB, Stanley EF (2004) A syntaxin 1, Galpha(o), and N-type calcium channel complex at a presynaptic nerve terminal: analysis by quantitative immunocolocalization. J Neurosci 24:4070-4081.

Liu T, Tucker WC, Bhalla A, Chapman ER, Weisshaar JC (2005) SNARE-Driven, 25-Millisecond Vesicle Fusion In Vitro. Biophys J 89:2458-2472.

Loerke D, Stuhmer W, Oheim M (2002) Quantifying axial secretory-granule motion with variable-angle evanescent-field excitation. J Neurosci Methods 119:65-73.

Loerke D, Preitz B, Stuhmer W, Oheim M (2000) Super-resolution measurements with evanescent-wave fluorescence excitation using variable beam incidence. J Biomed Opt 5:23-30.

Loerke D, Wienisch M, Kochubey O, Klingauf J (2005) Differential control of clathrin subunit dynamics measured with EW-FRAP microscopy. Traffic 6:918-929.

Lou X, Scheuss V, Schneggenburger R (2005) Allosteric modulation of the presynaptic Ca2+ sensor for vesicle fusion. Nature 435:497-501.

Manneville JB, Etienne-Manneville S, Skehel P, Carter T, Ogden D, Ferenczi M (2003) Interaction of the actin cytoskeleton with microtubules regulates secretory organelle movement near the plasma membrane in human endothelial cells. J Cell Sci 116:3927-3938.

Mattheyses A, Axelrod D (2002) Measurement of fluorophore excitation and emission properties near bare and metal coated surfaces. Biophys J (Annual Meeting Abstracts) 82:499.

Maximov A, Sudhof TC (2005) Autonomous function of synaptotagmin 1 in triggering synchronous release independent of asynchronous release. Neuron 48:547-554.

Merrifield CJ, Perrais D, Zenisek D (2005) Coupling between Clathrin-Coated-Pit Invagination, Cortactin Recruitment, and Membrane Scission Observed in Live Cells. Cell 121:593-606.

Merrifield CJ, Feldman ME, Wan L, Almers W (2002) Imaging actin and dynamin recruitment during invagination of single clathrin-coated pits. Nat Cell Biol 4:691-698.

Michael DJ, Geng X, Cawley NX, Loh YP, Rhodes CJ, Drain P, Chow RH (2004) Fluorescent Cargo Proteins in Pancreatic {beta}-Cells: Design Determines Secretion Kinetics at Exocytosis. Biophys J 87:L03-L05.

Misura KM, Scheller RH, Weis WI (2000) Three-dimensional structure of the neuronal-Sec1-syntaxin 1a complex. Nature 404:355-362.

Mitchell SJ, Ryan TA (2005) Munc18-dependent regulation of synaptic vesicle exocytosis by syntaxin-1A in hippocampal neurons. Neuropharmacology 48:372-380.

Moser T, Beutner D (2000) Kinetics of exocytosis and endocytosis at the cochlear inner hair cell afferent synapse of the mouse. Proc Natl Acad Sci U S A 97:883-888.

Murthy VN, Stevens CF (1999) Reversal of synaptic vesicle docking at central synapses. Nat Neurosci 2:503-507.

Nagai T, Ibata K, Park ES, Kubota M, Mikoshiba K, Miyawaki A (2002) A variant of yellow fluorescent protein with fast and efficient maturation for cell-biological applications. Nat Biotechnol 20:87-90.

Nagy G, Matti U, Nehring RB, Binz T, Rettig J, Neher E, Sorensen JB (2002) Protein kinase C-dependent phosphorylation of synaptosome-associated protein of 25 kDa at Ser187 potentiates vesicle recruitment. J Neurosci 22:9278-9286.

Nagy G, Reim K, Matti U, Brose N, Binz T, Rettig J, Neher E, Sorensen JB (2004) Regulation of releasable vesicle pool sizes by protein kinase A-dependent phosphorylation of SNAP-25. Neuron 41:417-429.

Naren AP, Nelson DJ, Xie W, Jovov B, Pevsner J, Bennett MK, Benos DJ, Quick MW, Kirk KL (1997) Regulation of CFTR chloride channels by syntaxin and Munc18 isoforms. Nature 390:302-305.

Neher E (1998) Vesicle pools and Ca2+ microdomains: new tools for understanding their roles in neurotransmitter release. Neuron 20:389-399.

Neher E, Marty A (1982) Discrete changes of cell membrane capacitance observed under conditions of enhanced secretion in bovine adrenal chromaffin cells. Proc Natl Acad Sci U S A 79:6712-6716.

Neves G, Lagnado L (1999) The kinetics of exocytosis and endocytosis in the synaptic terminal of goldfish retinal bipolar cells. J Physiol 515 (Pt 1):181-202.

Novick P, Schekman R (1979) Secretion and cell-surface growth are blocked in a temperature-sensitive mutant of Saccharomyces cerevisiae. Proc Natl Acad Sci U S A 76:1858-1862.

Novick P, Guo W (2002) Ras family therapy: Rab, Rho and Ral talk to the exocyst. Trends Cell Biol 12:247-249.

O'Connor V, Heuss C, De Bello WM, Dresbach T, Charlton MP, Hunt JH, Pellegrini LL, Hodel A, Burger MM, Betz H, Augustine GJ, Schafer T (1997) Disruption of syntaxin-mediated protein interactions blocks neurotransmitter secretion. Proc Natl Acad Sci U S A 94:12186-12191.

Ogawa H, Hayashi N, Hori I, Kobayashi T, Hosono R (1996) Expression, purification and characterization of recombinant C. Elegans UNC-18. Neurochem Int 29:553-563.

Oheim M (2001) Imaging transmitter release. II. A practical guide to evanescent-wave imaging. Lasers Med Sci 16:159-170.

Oheim M, Stuhmer W (2000) Tracking chromaffin granules on their way through the actin cortex. Eur Biophys J 29:67-89.

Oheim M, Loerke D, Chow RH, Stuhmer W (1999) Evanescent-wave microscopy: a new tool to gain insight into the control of transmitter release. Philos Trans R Soc Lond B Biol Sci 354:307-318.

Olivo-Marin J (2002) Extraction of spots in biological images using multiscale products. PATTERN RECOGNITION 35:1989-1996.

Paillart C, Li J, Matthews G, Sterling P (2003) Endocytosis and vesicle recycling at a ribbon synapse. J Neurosci 23:4092-4099.

Perez-Branguli F, Muhaisen A, Blasi J (2002) Munc 18a binding to syntaxin 1A and 1B isoforms defines its localization at the plasma membrane and blocks SNARE assembly in a three-hybrid system assay. Mol Cell Neurosci 20:169-180.

Perrais D, Kleppe I, Taraska J, Almers W (2004) Recapture after exocytosis causes differential retention of protein in granules of bovine chromaffin cells. J Physiol.

Petrenko AG, Perin MS, Davletov BA, Ushkaryov YA, Geppert M, Sudhof TC (1991) Binding of synaptotagmin to the alpha-latrotoxin receptor implicates both in synaptic vesicle exocytosis. Nature 353:65-68.

Pevsner J, Hsu SC, Scheller RH (1994) n-Sec1: a neural-specific syntaxin-binding protein. Proc Natl Acad Sci U S A 91:1445-1449.

Pyle JL, Kavalali ET, Piedras-Renteria ES, Tsien RW (2000) Rapid reuse of readily releasable pool vesicles at hippocampal synapses. Neuron 28:221-231.

Qian H, Sheetz MP, Elson EL (1991) Single particle tracking. Analysis of diffusion and flow in two-dimensional systems. Biophys J 60:910-921.

Reist NE, Buchanan J, Li J, DiAntonio A, Buxton EM, Schwarz TL (1998) Morphologically docked synaptic vesicles are reduced in synaptotagmin mutants of Drosophila. J Neurosci 18:7662-7673.

Rettig J, Neher E (2002) Emerging roles of presynaptic proteins in Ca++-triggered exocytosis. Science 298:781-785.

Rhee JS, Betz A, Pyott S, Reim K, Varoqueaux F, Augustin I, Hesse D, Sudhof TC, Takahashi M, Rosenmund C, Brose N (2002) Beta phorbol ester- and diacylglycerol-induced augmentation of transmitter release is mediated by Munc13s and not by PKCs. Cell 108:121-133.

Richards DA, Guatimosim C, Betz WJ (2000) Two endocytic recycling routes selectively fill two vesicle pools in frog motor nerve terminals. Neuron 27:551-559.

Richards DA, Bai J, Chapman ER (2005) Two modes of exocytosis at hippocampal synapses revealed by rate of FM1-43 efflux from individual vesicles. J Cell Biol 168:929-939.

Richmond JE, Weimer RM, Jorgensen EM (2001) An open form of syntaxin bypasses the requirement for UNC-13 in vesicle priming. Nature 412:338-341.

Rickman C, Archer DA, Meunier FA, Craxton M, Fukuda M, Burgoyne RD, Davletov B (2004) Synaptotagmin interaction with the syntaxin/SNAP-25 dimer is mediated by an evolutionarily conserved motif and is sensitive to inositol hexakisphosphate. J Biol Chem 279:12574-12579.

Riento K, Kauppi M, Keranen S, Olkkonen VM (2000) Munc18-2, a functional partner of syntaxin 3, controls apical membrane trafficking in epithelial cells. J Biol Chem 275:13476-13483.

Rizo J, Sudhof TC (1998) C2-domains, structure and function of a universal Ca2+-binding domain. J Biol Chem 273:15879-15882.

Rizzoli SO, Betz WJ (2004) The structural organization of the readily releasable pool of synaptic vesicles. Science 303:2037-2039.

Rohrbach A (2000) Observing secretory granules with a multiangle evanescent wave microscope. Biophys J 78:2641-2654.

Rosenmund C, Sigler A, Augustin I, Reim K, Brose N, Rhee JS (2002) Differential control of vesicle priming and short-term plasticity by Munc13 isoforms. Neuron 33:411-424.

Rowe J, Calegari F, Taverna E, Longhi R, Rosa P (2001) Syntaxin 1A is delivered to the apical and basolateral domains of epithelial cells: the role of munc-18 proteins. J Cell Sci 114:3323-3332.

Royle SJ, Lagnado L (2003) Endocytosis at the synaptic terminal. J Physiol 553:345-355.

Ryan TA (2001) Presynaptic imaging techniques. Curr Opin Neurobiol 11:544-549.

Sabatini BL, Regehr WG (1998) Optical measurement of presynaptic calcium currents. Biophys J 74:1549-1563.

Sakaba T, Neher E (2001) Quantitative relationship between transmitter release and calcium current at the calyx of held synapse. J Neurosci 21:462-476.

Sakaba T, Stein A, Jahn R, Neher E (2005) Distinct kinetic changes in neurotransmitter release after SNARE protein cleavage. Science 309:491-494.

Sara Y, Mozhayeva MG, Liu X, Kavalali ET (2002) Fast vesicle recycling supports neurotransmission during sustained stimulation at hippocampal synapses. J Neurosci 22:1608-1617.

Sassa T, Harada S, Ogawa H, Rand JB, Maruyama IN, Hosono R (1999) Regulation of the UNC-18-Caenorhabditis elegans syntaxin complex by UNC-13. J Neurosci 19:4772-4777.

Satzler K, Sohl LF, Bollmann JH, Borst JG, Frotscher M, Sakmann B, Lubke JH (2002) Three-dimensional reconstruction of a calyx of Held and its postsynaptic principal neuron in the medial nucleus of the trapezoid body. J Neurosci 22:10567-10579.

Saxton MJ (1993) Lateral diffusion in an archipelago. Single-particle diffusion. Biophys J 64:1766-1780.

Saxton MJ, Jacobson K (1997) Single-particle tracking: applications to membrane dynamics. Annu Rev Biophys Biomol Struct 26:373-399.

Schiavo G, Stenbeck G, Rothman JE, Sollner TH (1997) Binding of the synaptic vesicle v-SNARE, synaptotagmin, to the plasma membrane t-SNARE, SNAP-25, can explain docked vesicles at neurotoxin-treated synapses. Proc Natl Acad Sci U S A 94:997-1001.

Schikorski T, Stevens CF (2001) Morphological correlates of functionally defined synaptic vesicle populations. Nat Neurosci 4:391-395.

Schneggenburger R, Neher E (2005) Presynaptic calcium and control of vesicle fusion. Curr Opin Neurobiol 15:266-274.

Schneggenburger R, Sakaba T, Neher E (2002) Vesicle pools and short-term synaptic depression: lessons from a large synapse. Trends Neurosci 25:206-212.

Schoch S, Deak F, Konigstorfer A, Mozhayeva M, Sara Y, Sudhof TC, Kavalali ET (2001) SNARE function analyzed in synaptobrevin/VAMP knockout mice. Science 294:1117-1122.

Schulze KL, Littleton JT, Salzberg A, Halachmi N, Stern M, Lev Z, Bellen HJ (1994) rop, a Drosophila homolog of yeast Sec1 and vertebrate n-Sec1/Munc-18 proteins, is a negative regulator of neurotransmitter release in vivo. Neuron 13:1099-1108.

Schutz D, Zilly F, Lang T, Jahn R, Bruns D (2005) A dual function for Munc-18 in exocytosis of PC12 cells. Eur J Neurosci 21:2419-2432.

Scott BL, Van Komen JS, Irshad H, Liu S, Wilson KA, McNew JA (2004) Sec1p directly stimulates SNARE-mediated membrane fusion in vitro. J Cell Biol 167:75-85.

Shetty KT, Kaech S, Link WT, Jaffe H, Flores CM, Wray S, Pant HC, Beushausen S (1995) Molecular characterization of a neuronal-specific protein that stimulates the activity of Cdk5. J Neurochem 64:1988-1995.

Sigworth FJ, Sine SM (1987) Data transformations for improved display and fitting of single-channel dwell time histograms. Biophys J 52:1047-1054.

Smith C, Moser T, Xu T, Neher E (1998) Cytosolic Ca2+ acts by two separate pathways to modulate the supply of release-competent vesicles in chromaffin cells. Neuron 20:1243-1253.

Smith D (2003) Cdk5 in neuroskeletal dynamics. Neurosignals 12:239-251.

Sollner T, Bennett MK, Whiteheart SW, Scheller RH, Rothman JE (1993) A protein assembly-disassembly pathway in vitro that may correspond to sequential steps of synaptic vesicle docking, activation, and fusion. Cell 75:409-418.

Sollner T, Whiteheart SW, Brunner M, Erdjument-Bromage H, Geromanos S, Tempst P, Rothman JE (1993) SNAP receptors implicated in vesicle targeting and fusion. Nature 362:318-324.

Sorensen JB (2004) Formation, stabilisation and fusion of the readily releasable pool of secretory vesicles. Pflugers Arch 448:347-362.

Sorensen JB, Fernandez-Chacon R, Sudhof TC, Neher E (2003) Examining synaptotagmin 1 function in dense core vesicle exocytosis under direct control of Ca2+. J Gen Physiol 122:265-276.

Sorensen JB, Nagy G, Varoqueaux F, Nehring RB, Brose N, Wilson MC, Neher E (2003) Differential control of the releasable vesicle pools by SNAP-25 splice variants and SNAP-23. Cell 114:75-86.

Stevens CF, Sullivan JM (1998) Regulation of the readily releasable vesicle pool by protein kinase C. Neuron 21:885-893.

Steyer JA, Almers W (1999) Tracking single secretory granules in live chromaffin cells by evanescent-field fluorescence microscopy. Biophys J 76:2262-2271.

Steyer JA, Horstmann H, Almers W (1997) Transport, docking and exocytosis of single secretory granules in live chromaffin cells. Nature 388:474-478.

Sudhof TC (2004) The synaptic vesicle cycle. Annu Rev Neurosci 27:509-547.

Südhof TC, Scheller RH (2001) Mechanism and Regulation of Neurotransmitter Release. In: Synapses (Cowan WM, Südhof TC, Stevens CF, eds), pp 177-216. Baltimore: Johns Hopkins University Press.

Sugita S, Janz R, Sudhof TC (1999) Synaptogyrins regulate Ca2+-dependent exocytosis in PC12 cells. J Biol Chem 274:18893-18901.

Sun JY, Wu XS, Wu LG (2002) Single and multiple vesicle fusion induce different rates of endocytosis at a central synapse. Nature 417:555-559.

Sund SE, Swanson JA, Axelrod D (1999) Cell membrane orientation visualized by polarized total internal reflection fluorescence. Biophys J 77:2266-2283.

Sutton RB, Fasshauer D, Jahn R, Brunger AT (1998) Crystal structure of a SNARE complex involved in synaptic exocytosis at 2.4 A resolution. Nature 395:347-353.

Taraska JW, Almers W (2004) Bilayers merge even when exocytosis is transient. Proc Natl Acad Sci U S A 101:8780-8785.

Toomre D, Manstein DJ (2001) Lighting up the cell surface with evanescent wave microscopy. Trends Cell Biol 11:298-303.

Toonen RF, Verhage M (2003) Vesicle trafficking: pleasure and pain from SM genes. Trends Cell Biol 13:177-186.

Trifaro J, Rose SD, Lejen T, Elzagallaai A (2000) Two pathways control chromaffin cell cortical F-actin dynamics during exocytosis. Biochimie 82:339-352.

Trifaro JM, Lejen T, Rose SD, Pene TD, Barkar ND, Seward EP (2002) Pathways that control cortical F-actin dynamics during secretion. Neurochem Res 27:1371-1385.

Tsuboi T, Rutter GA (2003) Multiple forms of "kiss-and-run" exocytosis revealed by evanescent wave microscopy. Curr Biol 13:563-567.

Tsuboi T, Ravier MA, Xie H, Ewart MA, Gould GW, Baldwin SA, Rutter GA (2005) Mammalian exocyst complex is required for the docking step of insulin vesicle exocytosis. J Biol Chem.

Tucker WC, Weber T, Chapman ER (2004) Reconstitution of Ca2+-regulated membrane fusion by synaptotagmin and SNAREs. Science 304:435-438.

Unsicker K, Huber K, Schutz G, Kalcheim C (2005) The chromaffin cell and its development. Neurochem Res 30:921-925.

Veeranna, Grant P, Pant HC (1997) Expression of p67 (Munc-18), Cdk5, P-NFH and syntaxin during development of the rat cerebellum. Dev Neurosci 19:172-183.

Verhage M, de Vries KJ, Roshol H, Burbach JP, Gispen WH, Sudhof TC (1997) DOC2 proteins in rat brain: complementary distribution and proposed function as vesicular adapter proteins in early stages of secretion. Neuron 18:453-461.

Verhage M, Maia AS, Plomp JJ, Brussaard AB, Heeroma JH, Vermeer H, Toonen RF, Hammer RE, van den Berg TK, Missler M, Geuze HJ, Sudhof TC (2000) Synaptic assembly of the brain in the absence of neurotransmitter secretion. Science 287:864-869.

Vitale ML, Seward EP, Trifaro JM (1995) Chromaffin cell cortical actin network dynamics control the size of the release-ready vesicle pool and the initial rate of exocytosis. Neuron 14:353-363.

Voets T, Neher E, Moser T (1999) Mechanisms underlying phasic and sustained secretion in chromaffin cells from mouse adrenal slices. Neuron 23:607-615.

Voets T, Moser T, Lund PE, Chow RH, Geppert M, Sudhof TC, Neher E (2001) Intracellular calcium dependence of large dense-core vesicle exocytosis in the absence of synaptotagmin I. Proc Natl Acad Sci U S A 98:11680-11685.

Voets T, Toonen RF, Brian EC, de Wit H, Moser T, Rettig J, Sudhof TC, Neher E, Verhage M (2001) Munc18-1 promotes large dense-core vesicle docking. Neuron 31:581-591.

Washbourne P, Thompson PM, Carta M, Costa ET, Mathews JR, Lopez-Bendito G, Molnar Z, Becher MW, Valenzuela CF, Partridge LD, Wilson MC (2002) Genetic ablation of the t-SNARE SNAP-25 distinguishes mechanisms of neuroexocytosis. Nat Neurosci 5:19-26.

Washbourne P, Thompson PM, Carta M, Costa ET, Mathews JR, Lopez-Bendito G, Molnar Z, Becher MW, Valenzuela CF, Partridge LD, Wilson MC (2002) Genetic ablation of the t-SNARE SNAP-25 distinguishes mechanisms of neuroexocytosis. Nat Neurosci 5:19-26.

Weber T, Zemelman BV, McNew JA, Westermann B, Gmachl M, Parlati F, Sollner TH, Rothman JE (1998) SNAREpins: minimal machinery for membrane fusion. Cell 92:759-772.

Weimer RM, Richmond JE, Davis WS, Hadwiger G, Nonet ML, Jorgensen EM (2003) Defects in synaptic vesicle docking in unc-18 mutants. Nat Neurosci 6:1023-1030.

Wu MN, Schulze KL, Lloyd TE, Bellen HJ (2001) The ROP-syntaxin interaction inhibits neurotransmitter release. Eur J Cell Biol 80:196-199.

Xu T, Binz T, Niemann H, Neher E (1998) Multiple kinetic components of exocytosis distinguished by neurotoxin sensitivity. Nat Neurosci 1:192-200.

Xu T, Ashery U, Burgoyne RD, Neher E (1999) Early requirement for alpha-SNAP and NSF in the secretory cascade in chromaffin cells. Embo J 18:3293-3304.

Yokoyama CT, Myers SJ, Fu J, Mockus SM, Scheuer T, Catterall WA (2005) Mechanism of SNARE protein binding and regulation of Cav2 channels by phosphorylation of the synaptic protein interaction site. Mol Cell Neurosci 28:1-17.

Young SM, Jr. (2005) Proteolysis of SNARE proteins alters facilitation and depression in a specific way. Proc Natl Acad Sci U S A 102:2614-2619.

Zenisek D, Steyer JA, Almers W (2000) Transport, capture and exocytosis of single synaptic vesicles at active zones. Nature 406:849-854.

Zenisek D, Steyer JA, Feldman ME, Almers W (2002) A membrane marker leaves synaptic vesicles in milliseconds after exocytosis in retinal bipolar cells. Neuron 35:1085-1097.

Zhang L, Marcu MG, Nau-Staudt K, Trifaro JM (1996) Recombinant scinderin enhances exocytosis, an effect blocked by two scinderin-derived actin-binding peptides and PIP2. Neuron 17:287-296.

Zucker RS, Regehr WG (2002) Short-term synaptic plasticity. Annu Rev Physiol 64:355-405.

Curriculum Vitae

Personal data:
Full name: Olexiy Olexandrovich Kochubey
Born: 12.11.1979 in Dniepropetrovsk, Ukraine
Parents: Galina Sergiivna and Olexander Olexiyovich Kochubey
Citizenship: Ukraine
Martial status: married, no children. Wife, Korogod Natalya Sergiivna

September 1986 – July 1996	Elementary and secondary school N132, Dniepropetrovsk, Ukraine
September 1996 – July 2001	Studying at the Physical Faculty, Department of Experimental Physics, Dniepropetrovsk National University, Ukraine. B.Sc. degree in July 2000.
July 2001	Thesis defence for M.Sc. degree in "Biomedical and technical apparatus and systems"
October 2001 – August 2002	Master's course in the International MSc/PhD Study Program "Neurosciences", Georg-August-University, Göttingen, Germany
August 2002	Master's examination in "Neurosciences" Program, admission to the PhD part of the Program
Since October 2002	PhD project within the "Neurosciences" Program, in the group of Microscopy of Synaptic Transmission (AG Dr. Klingauf), Department of Membrane Biophysics (Prof. Dr. Neher), Max-Planck Institut for biophysical Chemistry, Göttingen, Germany. Thesis advisor – Dr. Jürgen Klingauf

Scholarships:

September 1999 - June 2001	Scholarship of the Parliament of Ukraine
February 2003 - September 2005	Fellowship of Deutsche Forschungsgemeinschaft (GRK 723, Prof. Dr. Schild, Göttingen)

Publication list

Loerke D., Wienisch M., Kochubey O., Klingauf J., 2005. Differential control of clathrin subunit dynamics measured with EW-FRAP microscopy. *Traffic* 6(10): 918-29.

Majumdar* A., Kochubey* O., Krishnan KS, Klingauf J. Imaging clathrin dynamics in *d. Melanogaster* hemocytes reveals a role for actin in vesicle fission. (*Submitted*, 2005)

Toonen* R.F., Kochubey* O., de Wit* H., Gulyas-Kovacs* A., Konijnenburg B., Sørensen J.B., Klingauf J., Verhage M. Dissecting vesicle docking and tethering principles in secretory cells (*Prep. for re-submission*, 2005)

* - authors contributed equally

Major congress contributions

Kochubey O., Khimich D., Moser T., Klingauf J. Observation of exo/endocytic activity in cochlear inner hair cells using TIRF microscopy. Program No. 900.8. *2003 Abstract Viewer/Itinerary Planner.* Washington, DC: Society for Neuroscience, 2003. Online.

Kochubey O., Toonen R.F., Verhage M., Klingauf J. Munc-18-1 promotes granule docking in chromaffin cells as revealed by evanescent wave microscopy. Program No. P33-10, *Abstract*, *Eur. J. Physiol 447 (Supplement 1)*, 2004.

Kochubey O.O.,. Toonen R.F, Verhage M., Klingauf J. Munc-18-1 is a positive regulator of granule docking in chromaffin cells as visualized by evanescent wave microscopy. Program No. 279.6. *2004 Abstract Viewer/Itinerary Planner.* Washington, DC: Society for Neuroscience, 2004. Online.